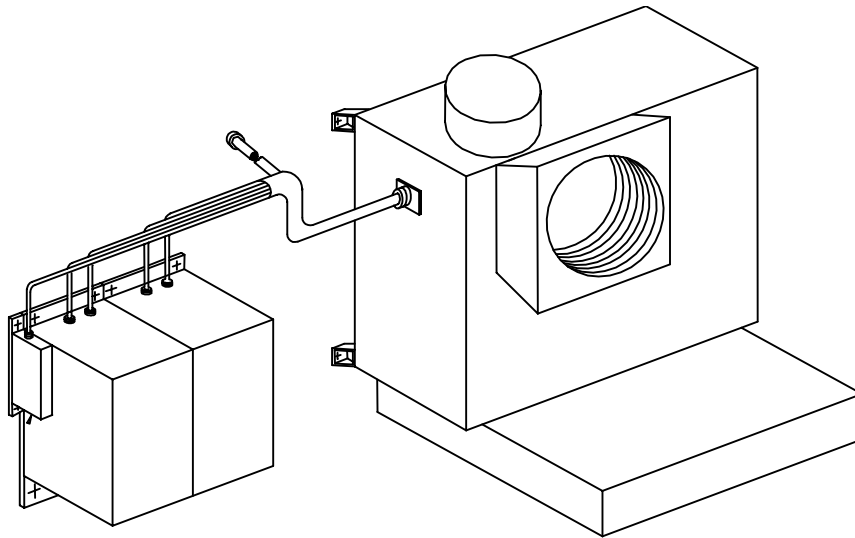


**Unclassified**



## **Advanced Baseline Sounder**

### **Design Study**

### **(Draft Version)**

L. Candell, M. MacDonald, G. Carlisle, M. Coakley, H. Finkle, M. Kelly, D. Ryan-Howard, D. Weidler,  
D. Weitz

MIT Lincoln Laboratory  
244 Wood St. Lexington, MA 02420-9185  
November, 1998

***For Official Use Only***

This work was sponsored by the National Oceanic and Atmospheric Administration under U.S. Air Force Contract F19628-95-C-0002.

Opinions, interpretations, conclusions, and recommendations are those of the authors and are not necessarily endorsed by the United States Air Force.

**Unclassified**

## **STUDY CHARTER**

NOAA NESDIS has asked MIT Lincoln Laboratory to conduct a study of the requirements, design, and implementation plan for a GOES Advanced Baseline Sounder (ABS) to meet the needs of the National Weather Service and other NOAA customers. The output of this study will provide 1) a baseline set of requirements, 2) key design tradeoffs for an instrument meeting these requirements and 3) an evaluation of cost, schedule and technical risk for a candidate design. The results of this study will be transferable to industry to serve as a guide to their response to an upcoming NESDIS Request for Information (RFI) for the ABS.



## EXECUTIVE SUMMARY

Since 1973, the Geosynchronous Operational Environmental Satellite (GOES) system has provided continuous coverage of the continental United States and adjacent ocean areas for the purposes of weather monitoring and prediction. It has become an indispensable component of the network of meteorological instruments operated by the National Weather Service, particularly in its ability to provide continuous information in otherwise data-sparse regions which are subject to severe weather, e.g. the oceans.

Two primary meteorological instruments are carried aboard GOES. The first is an earth imager which operates in several spectral bands from the visible to the long-wave IR. It provides information about surface temperature, cloud cover, cloud height and motion, and numerous other meteorological products which are highly valuable for characterizing the state of the atmosphere at any given time. The second instrument is an atmospheric sounder which operates over a broad range of the infrared spectrum within which numerous molecular absorption bands for carbon dioxide and water vapor exist. These absorption bands, in conjunction with window channels and visible imagery, provide a means for determining the vertical profile of atmospheric temperature and water vapor – profiles which are extracted from the measured spectral radiance through a set of retrieval algorithms. The resulting three-dimensional data set finds application in the initialization of numerical weather prediction models, and in meteorological products derived from the channels analogous to those derived from imager data.

The meteorological requirements of a future GOES sounder have been issued in draft form<sup>1</sup>. Systems engineering constraints are not addressed in this document, but are implied by the meteorological requirements.

This report documents a study carried out at the request of the National Oceanographic and Atmospheric Administration (NOAA) to formulate a point-design for an advanced baseline sounding instrument, from which high-resolution soundings of the atmosphere may be obtained from future GOES platforms. Tradeoffs between competing system options were conducted, and are documented in detail within this report to serve as a guide for potential contractors. The trade studies highlight the choices required in selecting different options for the architecture such an instrument should assume. The ABS point design is intended to be as detailed as the six-month study period permitted, with sufficient detail to verify its flight-worthiness. Estimates of the accuracy of the retrieved profiles are made as well, to determine the utility of the data which the instrument would provide to the meteorological community.

The recommendation of this study is that a high-resolution sounder based on a Fourier-transform Michelson spectrometer is a sufficiently proven design that it may be flown on future GOES platforms without unnecessary risk. The optical and electronic design of the instrument make it capable of producing data which meets the requirements of the NWS draft in terms of operability, spatial and spectral resolution, and sensitivity. Predicted temperature and humidity profiles validate this capability. A concise summary of the point design arrived at in this work is shown in Figure 1 and Table 1 on the following pages. The point design is described in detail in Section 3.

---

<sup>1</sup> NWS draft document "Observational Requirements for the Evolution of Future NOAA Operational Geostationary Satellites," 12 December, 1996

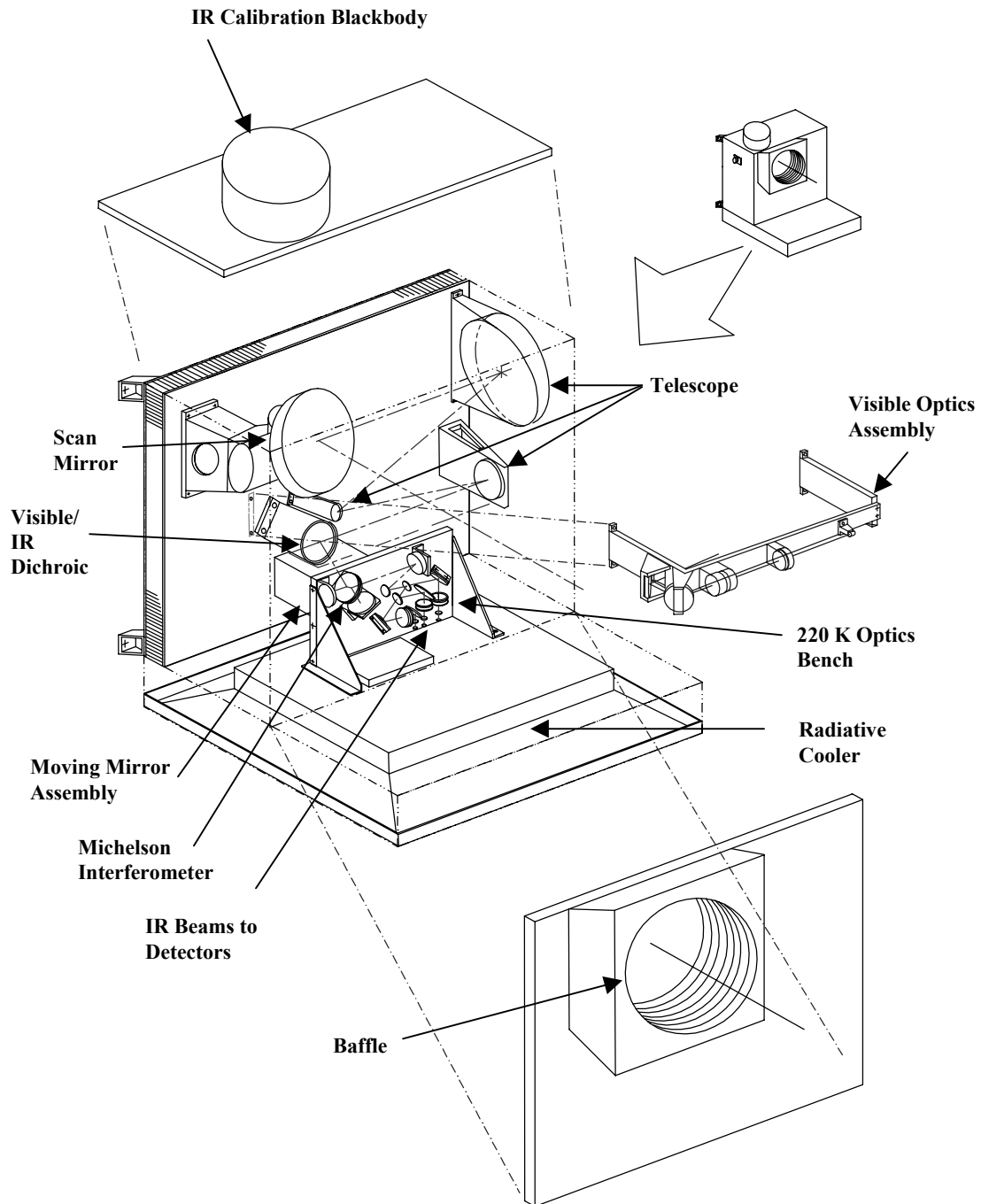


Figure 1. The Advanced Baseline Sounder overall layout is illustrated.

**TABLE 1**

**ABS Instrument Summary**

<b>Feature</b>	<b>Description</b>
Optical aperture	15.2 cm (6 in)
Scan method	2-axis, step & dwell, 4.4 mrad (160 km SSP) steps, E-W & N-S
Dwell time	3.1 s
Coverage rate	3000 km (N-S) x 5000 km (E-W) in 30 min Additional 5 minutes required for calibration
Spatial resolution	278 $\mu$ rad full-angle (10 km, SSP)
Spectral resolution	2.5 $\text{cm}^{-1}$ , 2150 – 2720 $\text{cm}^{-1}$ (shortwave)band 1.25 $\text{cm}^{-1}$ , 1210 – 1740 $\text{cm}^{-1}$ (midwave)band 0.625 $\text{cm}^{-1}$ , 662 – 1150 $\text{cm}^{-1}$ (longwave)band
Input telescope	Three-mirror, re-imaging, afocal telescope
Interferometer	Michelson interferometer, 1.1" diameter, ZnSe beamsplitter, porch-swing moving mirror in one arm, dynamically-aligned mirror (error < 0.8 $\mu$ rad) in second arm
Interferometer mirror sweep	$\pm 0.4$ cm, RMS velocity fluctuation < $\pm 1\%$
Aft-optics	Catadioptric, field-imaging, f/1.4 optics
Visible channel	Silicon 320 x 320 CCD, 12 $\mu$ m pixels, 300 K operating temperature, 14 $\mu$ rad pixel FOV (0.5 km, SSP), SNR = 600 for 10 ms integration
Star sensing	SNR $\geq 6$ for B0-class star
Data output	14-bit quantization
Data rate	~2.5 Mbit/s
Detector focal planes (all bands, unless otherwise noted)	PV HgCdTe 16 x 16 arrays, 60 $\mu$ m pixels, 75 K operating temperature, 278 $\mu$ rad pixel FOV (10 km, SSP), 172 $\mu$ s integration time (6 KHz frame rate), single 1.5 Mpix/s output, $2.8 \times 10^8$ e <sup>-</sup> charge storage. $\lambda_{\text{cutoff}} = 4.7$ $\mu$ m, SW band $\lambda_{\text{cutoff}} = 8.0$ $\mu$ m, MW band $\lambda_{\text{cutoff}} = 15.1$ $\mu$ m, LW band
Passive cooler construction	Three-stage design, no sun shield, $\varepsilon = 0.90$ EOL, 75 K patch (control point for IR detectors) 125 K radiator 220 K housing (control point for cold optics)
Passive cooler thermal budget (non-parasitic)	30 mW dissipation for each of three IR FPA's @ 75 K, 10 mW conduction to patch through wires, 15 W optics dissipation @ 220 K
Passive cooler stage area	Patch: 1310 $\text{cm}^2$ , Radiator: 280 $\text{cm}^2$ , Housing: 1320 $\text{cm}^2$ Overall size of square cooler $\approx 25'' \times 25''$
Calibration intervals	Space view: TBD, Blackbody view: TBD
Internal calibration blackbody	T = 320 K assumed in modeling
Predicted channel NE $\Delta$ N	0.02 mW/( $\text{m}^2$ sr $\text{cm}^{-1}$ ), SW band 0.09 mW/( $\text{m}^2$ sr $\text{cm}^{-1}$ ), MW band 0.31 mW/( $\text{m}^2$ sr $\text{cm}^{-1}$ ), LW band
Predicted retrieval accuracy	surface-300 mb: $\leq \pm 1.0$ K, $\leq \pm 10\%$ rel. humidity 300-100 mb: $\leq \pm 1.0$ K, $\leq \pm 20\%$ rel. humidity above 100 mb: $\leq \pm 1.0$ K
Instrument power consumption	~ 70 W
Instrument mass	~ 77 Kg
Instrument dimensions	See Figure 2

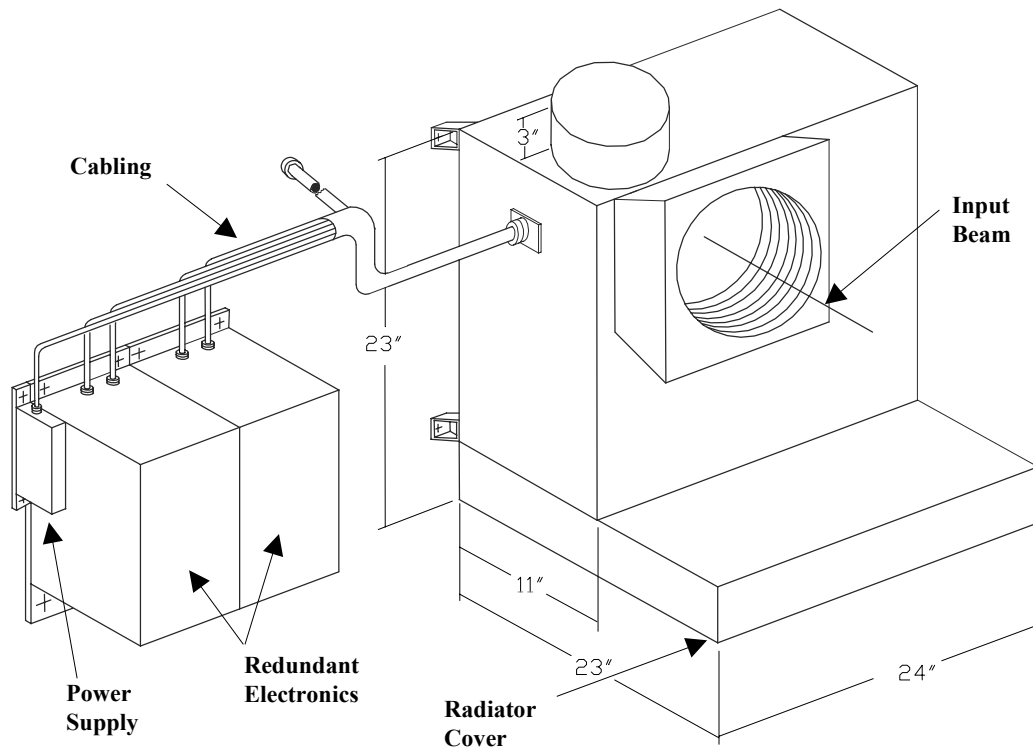


Figure 2. The Advanced Baseline Sounder outline dimensions are illustrated.

The operation of the ABS instrument is now briefly summarized, referring to Figure 1: Radiance from the earth scene is collected by a 6-inch diameter aperture, which is baffled to reduce the influx of sunlight into the instrument. The scene radiance is directed to the telescope by a scan mirror with two angular degrees of freedom. This mirror steps the 160 x 160 km instrument field-of-view over the earth scene, and rotates to allow the instrument to view either the internal blackbody or cold space for radiometric calibration. The telescope collects the scene radiance and passes it to a dichroic which splits the infrared portion of the spectrum off to the Michelson interferometer. The visible portion passes through the dichroic and lenses to a 320 x 320 visible CCD array which provides visible imagery for cloud-cover detection, and star-sensing capability for image registration. The scan mirror, telescope, and visible optics are mounted to an ambient-temperature optical bench.

The Michelson interferometer divides the IR radiance between two arms terminated in mirrors. The optical path-difference (OPD) between these arms is modulated by displacing one mirror to produce a time-varying interference pattern when the reflected beams are recombined at the beamsplitter. The second mirror uses actuators to dynamically maintain its surface parallel to that of the moving mirror. Although it is not shown in Figure 1, a near-IR diode laser produces a beam sharing a common path with the scene radiance which provides sampling metrology for the detector electronics. The output of the Michelson interferometer is relayed through dichroics and the aft optics to three photovoltaic detector focal planes optimized for the shortwave-, midwave-, and longwave-infrared regions. The aft optics configuration images the earth scene onto the detector arrays. The Michelson interferometer beamsplitter and refractive aft optics are mounted to a second optical bench which is cooled to 220 K by the outermost

stage of a passive radiative cooler. Kinematic mounts align this bench to the ambient-temperature optics while providing thermal isolation.

Each detector focal plane is implemented as a 16 x 16 pixel array of photovoltaic HgCdTe which is connected to a silicon readout which multiplexes the pixels through a serial output. The detector focal planes are mounted to the 75 K innermost stage of the passive radiative cooler. An intermediate stage reduces parasitic coupling of heat between the 220 K and 75 K stages. A mounting arrangement between the cooler stages minimizes thermal conductance and allows the longwave channel to maintain its alignment warm-to-cold. Differential expansion between the 220 K and 75 K optics mounts affects the shortwave and midwave channels, but these remain within their required sensitivity.

The detected signal is in the form of an interferogram, which contains the spectral information for each pixel encoded in the time domain. This signal is amplified and sampled at OPD intervals determined by the metrology system. It is then digitized, and is routed to a digital signal processor which implements a decimating FIR filter on the oversampled data. The resulting data stream is compatible with the existing GOES down-link bandwidth. Control circuits for instrument components such as the scan mirror, moving mirror, dynamic alignment mirror, and thermal control loops are implemented within the ABS instrument.

Apart from its power and downlink requirements, the instrument operates independently of the satellite bus, and imposes only two bus requirements: that the side of the bus on which the radiative cooler is mounted presents a clear hemispherical view to space, and that a yaw flip be executed at each equinox to prevent solar irradiation of the radiative cooler. These are not considered by the GOES community to be unreasonable constraints.





## **ACKNOWLEDGMENTS**

The authors gratefully acknowledge Dan Mooney for consultation on technical issues, and John Kerekes for guidance in regard to the retrieval estimates. We are also grateful to Karen Hovsepian and Suzanne Pettingell for their assistance in preparing the manuscript.



# TABLE OF CONTENTS

	<b>Page</b>
Study Charter	iii
Executive Summary	v
Acknowledgments	xi
List of Illustrations	xv
List of Tables	xix
 1. INTRODUCTION	 1
1.1 Desired Improvements Over Existing Sounder	1
1.2 Study Definition	1
1.3 Outline of the Report	2
 2. ABS REQUIREMENTS	 3
2.1 Overview	3
2.2 Instrument Requirements	3
 3. ABS POINT DESIGN	 7
3.1 Overview	7
3.2 Optical System Point Design	7
3.3 Detector Point-Design	10
3.4 Mechanical Design	11
3.5 Electronics System Point-Design	17
3.6 Estimation of ABS Developmental Cost	27
3.7 Technology Risk Areas and Long-Life Issues	28
 4. TRADE STUDIES MADE PRECEDING THE POINT DESIGN	 31
4.1 Overview	31
4.2 Diffraction Grating vs. FTS Spectrometer	31
4.3 Optics Trade	36
4.4 Detector Focal Plane Array Options	44
4.5 LW-Band Detector Cutoff Wavelength Selection	51
4.6 IR Detector Readout Options	59
4.7 Passive Radiative Cooling vs. Refrigeration of Focal Planes	70
4.8 Visible Channel Design	78
4.9 Data-Processing Electronics Trades	82
 APPENDIX A. LIST OF ACRONYMS	 89
 APPENDIX B. GRATING AND FTS SPECTROMETERS	 91

## **TABLE OF CONTENTS (Continued)**

	<b>Page</b>
APPENDIX C. INTERFEROMETER PERFORMANCE MODEL	97
APPENDIX D. ABS POINT DESIGN OPTICAL PRESCRIPTION	103

## LIST OF ILLUSTRATIONS

Figure No.		Page
1	The Advanced Baseline Sounder overall layout is illustrated.	iv
2	The Advanced Baseline Sounder outline dimensions are illustrated.	vi
3-1	Schematic of the optical system for the ABS Point Design.	8
3-2	Spot diagrams for the infrared channels.	9
3-3	Spot diagrams for the visible channel.	10
3-4	The ABS sensor layout is shown.	12
3-5	The optical design approach is shown, illustrating the location of the optics on the 300 K and 220 K optical benches.	13
3-6	The ABS radiative cooler is shown, along with the kinematic mounting concept used to maintain the LWIR channel in alignment. A flexure is shown at right.	15
3-7	The mounting concept used to align the 220 K optics bench and radiative cooler to the 300 K optics is shown.	16
3-8	ABS electronics system architecture.	18
3-9	Instrument controller and FPA timing/readout.	18
3-10	Reference Interferometer (conceptual diagram).	19
3-11	Metrology and sampling electronics.	20
3-12	IR signal processing chain.	21
3-13	Visible channel signal processing.	22
3-14	Scan mirror servo controller.	22
3-15	FTS mirror servo controller.	23
3-16	Dynamic alignment mirror servo controller.	23
3-17	Reduction in modulation efficiency due to mirror tilt.	24
3-18	Visible CCD thermal controller.	25
3-19	FPA radiant cooler thermal controller.	25

## LIST OF ILLUSTRATIONS (Continued)

Figure No.		Page
3-20	Instrument power supply.	26
4-1	The operation of a Michelson interferometer is illustrated.	33
4-2	An echelle grating is illustrated	34
4-3	The imaging modes available for an FTS (left) and echelle grating (right) are illustrated.	35
4-4	Modulation vs. half angle in Interferometer.	38
4-5	ABS Interferometer component diameters.	39
4-6	ABS Interferometer transmission.	39
4-7	System f-number.	40
4-8	Comparison of non-reimaging and reimaging input telescopes.	41
4-9	6-inch and 8-inch collecting aperture telescopes.	41
4-10	Schematic of field imaging optics.	42
4-11	Schematic of pupil imaging system for (a) single detector and (b) array.	43
4-12	Pupil imaging system with microlens array at intermediate image.	43
4-13	Comparison of catadioptric and refractive aft optics.	44
4-14	Theoretical limit to $D^*BLIP$ and thermal-noise limited $D^*$ for PC MCT detectors, $T=65, 75, 85$ K.	48
4-15	Theoretical limit to $D^*BLIP$ and thermal-noise limited $D^*$ for unbiased PV HgCdTe detectors, $T=65, 75, 85$ K.	49
4-16	Theoretical limit to performance of 6x6 PC and PV array compared to a 16 x 16 PV array (all at $T=65$ K) as a function of wavenumber.	50
4-17	LW minimum NedN in each band as a function of detector temperature.	50
4-18	The peak pressure of a large number of weighting functions is plotted vs. wavelength.	52

## LIST OF ILLUSTRATIONS (Continued)

Figure No.		Page
4-19	The simulated RMS temperature error is plotted vs. pressure for a 16 x 16 array operated at 75 K for peak wavelengths of 13.0, 13.3, 13.7, 14.0, 14.3, 14.7, 15.0, and 16.0 $\mu\text{m}$ .	53
4-20	Mean RMS temperature error as a function of wavelength in the 1000 - 300 mb zone for detectors tuned to various peak wavelengths (listed in Figure 4-19), with detector temperatures of 65 K, 70 K, 75 K, 80 K, and 85 K.	55
4-21	Mean RMS temperature error as a function of wavelength in the 300 - 100 mb zone for detectors tuned to various peak wavelengths (listed in Figure 4-19), with detector temperatures of 65 K, 70 K, 75 K, 80 K, and 85 K.	55
4-22	Mean RMS temperature error as a function of wavelength in the 100 - 5 mb zone for detectors tuned to various peak wavelengths (listed in Figure 4-19), with detector temperatures of 65 K, 70 K, 75 K, 80 K, and 85 K.	56
4-23	Mean RMS temperature error as a function of wavelength in the 100 - 5 mb zone for detectors tuned to various peak wavelengths (listed in previous Figure 4-19), with detector temperatures of 65 K, 70 K, 75 K, 80 K and 85 K. Values from current detector technology are shown based on published $R_0A$ and temperature data from LMIRIS.	57
4-24	Results of retrieval showing mean RMS relative humidity error as a function of height.	58
4-25	Mean RMS relative humidity error in the 1000 - 300 mb region plotted versus wavenumber.	58
4-26	Mean RMS relative humidity error from 300 - 130 mb region plotted as a function of peak wavelength.	59
4-27	The RTIA with a source follower input and output filter.	60
4-28	The CTIA with a source follower input.	61
4-29	The ratio of amplifier noise current to detector noise current as a function of the detector bias, for detector temperatures between 65 and 80 K.	62
4-30	The readout capacitor storage capacity as function of area and breakdown electric field and vendor capacities.	65



## LIST OF ILLUSTRATIONS (Continued)

Figure No.		Page
4-31	The minimum readout rates required viewing an earth scene with a $2.8 \times 10^8$ electron integration capacity.	66
4-32	Aperture diameter (solid curve) required to meet our NedN goal as a function of array size for a $T=80$ K array, the pixel rate (dashed curve) is plotted on the right vertical axis.	68
4-33	Aperture diameter (solid curve) required to meet our NedN goal as a function of array size, assuming a 75 K array temperature, the pixel rate (dashed curve) is plotted on the right vertical axis.	68
4-34	NedN (solid curve) as a function of aperture diameter for a 75 K $16 \times 16$ array, the pixel rate (dashed curve) is plotted on the right vertical axis.	68
4-35	NedN (solid curve) as a function of array size for a fixed 15 cm aperture, with the array cooled to 75 K, the pixel rate (dashed curve) is plotted on the right vertical axis.	69
4-36	The process by which the cooler size was determined is illustrated here.	72
4-37	The mechanical layout of the radiative cooler is illustrated.	73
4-38	A plot of the side length of a square three-stage cooler is shown for a 70 K (uncontrolled) patch temperature as a function of the radiator temperature.	74
4-39	The assumed configuration for an actively-cooled design is shown, with one PTC de-energized.	77
4-40	Current GOES star sensing methodology versus ABS star sensing methodology.	81
4-41	ABS signal processing architecture.	84
4-42	Modeled performance for different number of quantization bits.	87
4-43	Integration period and mirror velocity as functions of FPA size.	88
C-1	Flow chart detailing the steps considered in calculating the NedN of a Fourier transform interferometric sounder.	97
C-2	PV detector current-voltage characteristics.	100
D-1	Perspective view of the ABS system.	107

## LIST OF TABLES

Table No.		Page
1	ABS Instrument Summary	v
2-1	NWS Sounding Requirements	3
3-1	Summary of IR Detector Focal Planes	10
3-2	Summary of Visible Detector Focal Plane	11
3-3	ABS Weight Estimate	17
3-4	Subsystem Power Allocation	26
3-5	Summary of ABS Development	27
3-6	Breakdown of ABS Cost of Subsystem	28
4-1	General Differences between Grating Spectrometers and Fourier-Transform Michelson Spectrometers	32
4-2	Assumed Parameters	37
4-3	Instrument and Satellite Parameters	45
4-4	Background Inputs for the LW Channel	46
4-5	Background Inputs for the MW Channel	46
4-6	Background Inputs for the SW Channel	47
4-7	Detector Model Input and Output Parameters	47
4-8	The Ideal Sampling Rate, Detector Stare Time, Capacitor Integration Time, and Fixed Pixel Rate for Several Array Sizes Between 6 x 6 and 32 x 32.	63
4-9	The Minimal Zero Bias Readout Rate to Prevent Saturation at $2.8 \times 10^8$ Electrons	66
4-10	Minimum Readout Rates for the LW Band Fully Reverse Biased at Different Detector Temperatures	66
4-11	Minimum Pixel Rates for the LW Band Fully Reverse Biased for Several Array Sizes and Temperatures	66

## **LIST OF TABLES (Continued)**

<b>Table No.</b>		<b>Page</b>
4-12	Trade Study Resulting Instrument, Satellite, and Signal Processing Parameters	70
4-13	A Few General Differences Between Passively-Cooled and Actively-Cooled Systems are Highlighted	71
4-14	A Summary of the Passive Cooler Design Cases Considered in the Trade Study	75
4-15	The Performance of the TRW PTC 7203 is Summarized	77
4-16	Actively-Cooled Designs Considered in the Trade Study	78
4-17	ABS Nominal Operation	83
4-18	Alternative ABS Sounding Modes	86

# 1. INTRODUCTION

Historically, the data obtained from the GOES sounder has been considered less valuable by meteorologists than the imager data. Comparisons of predictions made using data available from radiosondes with that using both radiosondes and the GOES sounder has identified only a small benefit from the satellite data. Several hypotheses have been advanced to explain this small benefit, but the two factors generally cited have been insufficient accuracy of the retrieved profiles, and insufficient vertical resolution<sup>2</sup>. The National Oceanographic and Atmospheric Administration (NOAA) has expended a considerable degree of effort to develop means of overcoming these limitations. The retrieval accuracy problem has been worked both from the point of view of reducing instrument noise by utilizing advanced infrared detector technology, and by improving retrieval algorithms which are required to invert the measured spectral radiance to a calculated profile. The vertical resolution problem has inspired work to develop instruments with thousands of spectral channels using either a grating (e.g. AIRS<sup>3</sup>) or Michelson interferometer (e.g. ITS<sup>4</sup> and GHIS<sup>5</sup>) configuration.

## 1.1 DESIRED IMPROVEMENTS OVER EXISTING SOUNDER

The GOES I-O sounder is a radiometer which employs a rotating filter wheel in the optical path to divide the scene radiance into 17 spectral channels. The spectral resolution of the sounding instrument influences the width of the weighting functions used in the retrieval algorithms, and the vertical resolution of the profiles which these algorithms produce. The availability of a far higher number of spectral channels in an FTS instrument compared to the filter-wheel approach permits the vertical resolution of the soundings to be substantially improved.

Improvements in infrared detector array technology realized in the past several years likewise permit an advanced instrument to obtain profiles with increased accuracy. The recent development of long-cutoff-wavelength HgCdTe photovoltaic detector arrays enables the development of imaging arrays which permit long integration times while staring at the scene. This is in contrast to the 4-element detectors employed in the GOES I-O instrument. The operating temperature of the detectors can be lowered to 75 K from the 94 K in GOES I-O by eliminating the astro-mast and performing a yaw flip of the bus at each equinox. This increases the sensitivity of the detectors with a corresponding improvement in instrument sensitivity.

## 1.2 STUDY DEFINITION

### 1.2.1 Objectives and Scope

The purpose of this study was to produce a realistic point design of a high-resolution sounding instrument suitable for flight on a future GOES satellite. The design was not intended to be sufficiently detailed that activities such as solid modeling, analysis of vibrational modes, detailed thermal predictions, etc. could be carried out. It was instead intended to be sufficiently detailed to allow critical evaluation of

---

<sup>2</sup> W. L. Smith, "Atmospheric soundings from satellites – false expectation or the key to improved weather prediction," *Q. J. R. Meteorol. Soc.*, Vol. 117, pp. 267-297, (1990).

<sup>3</sup> H. H. Aumann, C. Miller, "Atmospheric infrared sounder (AIRS) on the earth observing system," [http://www-air.jpl.nasa.gov/papers/sci\\_eng\\_papers/paper\\_001/george.html](http://www-air.jpl.nasa.gov/papers/sci_eng_papers/paper_001/george.html)

<sup>4</sup> D. L. Mooney, et. al., "POES High-resolution sounder study final report," Project Report NOAA-1, MIT Lincoln Lab, 25 January, 1993.

<sup>5</sup> W. E. Bicknell, et. al., "GOES High-resolution interferometer study," Project Report NOAA-12, MIT Lincoln Lab, 5 June, 1995.

the design specifics by readers of this report. This process of design and evaluation should then form the basis of a comprehensive development effort, to be carried out by industry, producing an instrument which is fully capable of incorporation into the GOES platform.

### **1.2.2 Team Members**

The following people were members of the study team, and are responsible for the content of this report:

Larry Candell	Leader
Guy Carlisle	
Monica Coakley	
Harry Finkle	
Mike Kelly	
Mike MacDonald	Report editor
Danette Ryan-Howard	
Darryl Weidler	
Dave Weitz	

### **1.2.3 History of Activities**

The ABS study was kicked off at a meeting among the MIT/LL team members on April 22, 1998. Subsequent meetings were held approximately every two weeks. Briefings to NOAA on the progress of the study were conducted at the GOES quarterly reviews on June 18, 1998 at MIT/LL and on September 23, 1998 at NOAA. The report was assembled during October 1998 and was submitted in draft form to NOAA on November 19, 1998.

## **1.3 OUTLINE OF THE REPORT**

This report is divided into three main sections. Section 2 details the requirements imposed on the ABS instrument by the user community. Section 3 is a description of the point design which was arrived at as a result of the various trade studies. Section 4 details the trade studies themselves, which were carried out as the instrument design converged to its final configuration. The ordering of the sections is chosen so that the reader can proceed from the Executive Summary through Sections 3 and 4 with increasing levels of detail being encountered. Most of the design detail is kept in Section 4, in the interest of keeping the report modular so that each element of the design can be evaluated individually. The reader must bear in mind that the various elements of the ABS design are intertwined in such a way that a change in one part of the design tends to propagate through the remaining parts. Each trade study is prefaced by a short bulleted list which highlights the key points considered within the trade.

## 2. ABS REQUIREMENTS

### 2.1 OVERVIEW

The ABS performance requirements derive primarily from NWS guidelines. As detailed in the NWS draft document<sup>1</sup>, the NWS and NESDIS community selected critical imager and sounder performance requirements from a larger set of desired operational features. These critical requirements then framed the main goals for MIT Lincoln Laboratory's ABS point-design study. In addition, the ABS study sought to maintain compatibility with salient requirements for the present sounder instrument, as delineated in the GOES NO/PQ performance specification<sup>6</sup>.

According to the NWS requirements draft, geostationary soundings must provide continuous and reliable high-resolution data that will usefully complement other existing data sources. In particular, geostationary observations should cover: (1) coastal and open oceans, as well as other areas not observed with existing data; (2) near gradients between other data sources; and (3) between temporal gaps in polar satellite coverage. High-resolution geostationary measurements of temperature, water vapor, and wind should help to resolve steep spatial and vertical gradients in the temperature and vapor fields, and thus augment radiosonde coverage.

Table 2-1 summarizes the NWS requirements for sounding accuracy and resolution.

**TABLE 2-1**

**NWS Sounding Requirements**

Altitude Range	Observational Accuracy (RMS Error)		Vertical Resolution
	Temperature	Humidity	
Surface – 300 Mb	± 1.0 K	± 10%	1 – 2 km layers
300 – 100 Mb	± 1.0 K	± 20%	2 – 3 km layers
100 Mb and above	± 1.0 K	-----	3 – 6 km layers

### 2.2 INSTRUMENT REQUIREMENTS

All requirements listed below, unless otherwise noted, represent 1 standard deviation accuracy. Sources for each individual item are as indicated. It is important to note that these numbers are subject to change based on revision of NWS/NESDIS requirements. Moreover, this list is not intended to be exhaustive, but merely outlines some of the key requirements that influenced the ABS study.

---

<sup>6</sup> "Performance Specification for GOES-NO/PQ Imager and Sounder Instruments," NASA Goddard Space Flight Ctr., 28 March, 1996

(1) COVERAGE AREA and RATE – *NWS draft requirement, NESDIS, and MIT Lincoln Lab*

3000 km x 5000 km in 30 minutes (plus 5 minutes for IR calibrations) and, when needed, one 1000 km x 1000 km enhancement.

Mesoscale uses: 1000 km x 1000 km every 6 minutes, for either the same or different areas. (Note that this represents a coverage rate three times slower than the 30 minute, 3000 km x 5000 km mode.)

(2) SPATIAL RESOLUTION -- *NWS draft requirement*

Ground spot diameter  $\leq 10$  km (at SSP); 10 km spacing.

80% of energy incident on detector pixel must originate from circle of this diameter.

(3) SPECTRAL RANGE and RESOLUTION -- *“Industry practice” (to meet vertical resolution requirements using an inversion-based technique)*

Longwave:	650-1150 $\text{cm}^{-1}$ ,	0.625 $\text{cm}^{-1}$ resolution
Midwave:	1210-1740 $\text{cm}^{-1}$ ,	1.25 $\text{cm}^{-1}$ resolution
Shortwave:	2150-2720 $\text{cm}^{-1}$ ,	2.5 $\text{cm}^{-1}$ resolution

Contemporaneous Visible Imagery -- *NWS draft requirement*

- Specify cloud cover within 10%
- Simultaneous and collocated with IR data FOV
- Sub-IR pixel resolution recommended

(4) RADIOMETRIC RESOLUTION (NOISE PERFORMANCE)

NEdN: 0.5 $\text{mW}/(\text{m}^2 \cdot \text{cm}^{-1} \cdot \text{sr})$	Longwave
0.1 $\text{mW}/(\text{m}^2 \cdot \text{cm}^{-1} \cdot \text{sr})$	Midwave
0.05 $\text{mW}/(\text{m}^2 \cdot \text{cm}^{-1} \cdot \text{sr})$	Shortwave

Origin: meets *NWS draft requirement* for temperature error bound,  $\pm 1$  K rms for 60 km x 60 km averaged cell size. (Note that this exceeds GHIS instrument performance goals.)

(5) SOUNDING-CELL RESOLUTION -- *NWS draft requirement*

At least one temperature and water vapor sounding in every adjacent 60 km x 60 km area (as clouds permit).

(6) SENSITIVITY and DYNAMIC RANGE -- *NWS draft requirement*

Should span from brightness temperature of NEdT to the blackbody calibration target or the highest scene temperature (whichever is larger).

(7) LIFETIME -- *NESDIS*

7 years mission  
9 years design

(8) MASS (“GROWTH CAPABILITY”) -- *NWS draft requirement*

Excess capacity > 25% of payload mass capacity [i.e., instrument mass < 0.75 · (maximum payload mass)]

(9) BAND-TO-BAND REGISTRATION -- *NWS draft requirement*

Centroids of each spectral region matched to within 10%.

Maximum 10 seconds dwell for each FOV (to avoid clouds encroaching into more than 10% of FOV).

(10) PIXEL-TO-PIXEL REGISTRATION -- *NWS draft requirement*

Adjacent position errors < 1 km (at SSP).

(11) IMAGE-TO-IMAGE REGISTRATION -- *NWS draft requirement*

Single pixel jitter < 2.5 km (at SSP).

(12) IR CALIBRATION -- *NASA/GSFC performance requirement for GOES-NO/PQ*

Absolute	1 K
Non-linearity	< 1.7%
Relative calibration	
Line-to-line (same detector)	0.1 K
Detector-to-detector	0.1 K
Channel-to-channel	0.1 K
Calibration-to-calibration	0.1 K
Crosstalk (electrical/optical)	< 0.1%

(13) NAVIGATION/EARTH LOCATION -- *NWS draft requirement*

Knowledge < 2.5 km at SSP (for all scan modes)

Contiguous samples at 5000 km from SSP on earth (in viewing direction)

Allowable degradation at local midnight and during maneuvers compatible with imager requirements.

(14) STRAY LIGHT -- *no requirement available*

(15) MTF -- *no requirement available*

(16) INDUCED VIBRATIONS (from FTS & Scan mirrors) -- TBD

(17) EMI (frequencies, levels, locations) -- TBD

(18) THERMAL LOADING (of satellite bus) – TBD





### **3. ABS POINT DESIGN**

#### **3.1 OVERVIEW**

In this section the ABS point design is presented, representing the culmination of a series of system trade studies conducted as the design evolved. These trade studies are documented in Section 4. This point design embodies an instrument which is capable of meeting the requirements of the previous section without entailing unnecessary size, cost or risk. In likelihood it does not, however, represent the only such instrument. The trade studies were conducted in an iterative manner, and do not preclude other approaches to designing a high-quality instrument. We believe, however, that this instrument design does provide a valuable blueprint for future work to be conducted in implementing a high-resolution atmospheric sounder on future GOES platforms. Moreover, we believe that this point design represents a near-optimal architecture.

The general flow of this section may be summarized as follows: The overall optical design is presented in Section 3.2 which images the earth scene to three IR and one visible focal plane. This includes the input telescope, interferometer, and the aft optics. A concise summary of the IR focal planes is then given in Section 3.3. A detailed mechanical design is then presented in Section 3.4 which is focused on details such as mounting and alignment of the optical elements, the measures taken to cool different elements, and the overall construction and mass of the ABS instrument. The electronics required for instrument control, metrology and sampling, and signal processing are detailed individually in Section 3.5 along with an instrument power consumption budget. Estimates for the instrument costs are presented in Section 3.6. Finally, a brief summary of the technology risk areas we believe may be associated with this point design, and some comments on long-lifetime issues, are presented in Section 3.7.

#### **3.2 OPTICAL SYSTEM POINT DESIGN**

The point design has a 6-inch aperture, reimaging input telescope and requires a scan mirror that is approximately 6.5 x 11.3 inches. The input telescope is followed by a dichroic beamsplitter that transmits visible radiation and reflects infrared radiation. The interferometer and the infrared aft optics are cooled to 220 K to reduce the emissivity of the refractive components. The Michelson interferometer has a 1.1-inch working aperture. The moving mirror in the interferometer has a full sweep of 0.8 cm. Field imaging, catadioptric aft optics, which operate at  $f/1.42$ , were selected. The infrared optics have 10-km resolution and an instantaneous ground field-of-view of 160 x 160 km. The three 16 x 16 pixel detector arrays, which have 60- $\mu\text{m}$  pixels, are cooled to 75 K. The footprint for the point design optical system is small, only 20 x 18 inches prior to adding the housings. A visible optical train, which is compatible with the input telescope design, has been included. The visible optics have 0.5-km resolution and cover the 160 x 160 km ground field-of-view. A schematic of the optical system for the point design is shown in Figure 3-1. The prescription is included as Appendix D.

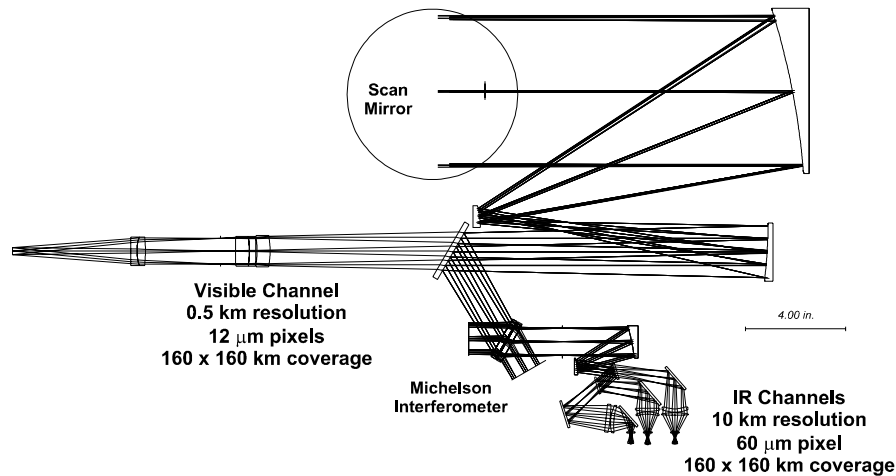


Figure 3-1. Schematic of the optical system for the ABS Point Design.

### 3.2.1 Input Telescope Optics

The input telescope has a 6-inch collecting aperture and produces a 1.1-inch diameter collimated beam. The 1.1-inch diameter was selected for the interferometer aperture in Section 4.3.2. The afocal telescope comprises three powered mirrors with a common axis of symmetry. An off-axis section of each mirror is used. The image of the aperture stop was placed near the scan mirror in the point design. The exact location of the entrance pupil was not constrained during the design process and can be adjusted. Although it may be desirable to have an accessible internal image in the input telescope, it was not maintained as a design constraint.

### 3.2.2 Interferometer

The interferometer accepts the 1.1-inch collimated beam produced by the input telescope. The moving mirror on the interferometer has a full physical sweep of 0.8 cm. The field-of-view within the interferometer is  $\pm 0.98$  degrees to the corners of the field. A zinc selenide (ZnSe) beamsplitter / compensator pair was chosen based on Section 4.3.3. The metrology optics associated with the interferometer are not shown in the optical schematics.

### 3.2.3 Aft Optics

As discussed in Section 4.3.5, field imaging aft optics were selected since the detectors have a uniform response across the pixel area and the field imaging system does not require a microlens array. The infrared detector arrays are cooled to 75 K. The detector arrays for the shortwave, midwave and longwave channels lie in a common plane, which can be located against the cooler patch. Common reflective optics for the three channels were considered. There was, however, insufficient space for the dichroic beamsplitters if the common reflective optics were the only powered elements in the  $f/1.42$  aft optical train. With a slower common optical system (e.g.  $f/2$ ), supplemental optics would be required in each channel to achieve the final  $f$ -number, i.e. a catadioptric design form. The beamsplitters in the converging  $f/2$  beam would need to be wedged to minimize aberrations. Either refractive or catadioptric aft optics can be used. The system should have an intermediate image so that an image of the aperture stop can be formed in front of the detector. An efficient cold stop is located at the image of the aperture stop. Telecentric optics are used to form a well-corrected intermediate image. Relay optics (2:1) are then

used to form the final image. The catadioptric design form was selected for the point design since it is more compact, is slightly easier to athermalize, and has common reflective elements forming an accessible intermediate image in each channel. There are minimal clearances in some areas of the aft optics. Clearance issues would be resolved during the integration of the mechanical and optical designs.

### 3.2.4 Visible Optics

A visible channel with 0.5-km resolution was included in the baseline system. A five-element, refractive optical system was developed to form an image of the ground on the visible array. The visible system has a 160 x 160 km field-of-view and was designed for a wavelength range from 500 to 700 nm. The visible optics operate at  $f/5.66$ . The selected detector array has 12- $\mu\text{m}$  pixels.

### 3.2.5 Performance

**Infrared Performance.** Figure 3-2 displays the spot diagrams for the infrared channels. The on-axis field point, a point at the edge of the field, and a point at the corner of the field are shown. All three channels have diffraction-limited performance on axis. The longwave channel has diffraction-limited performance at all field points. Although the shortwave and midwave channels do not have diffraction-limited performance at all field points, performance is acceptable since the geometrical spot size is smaller than the pixel size.

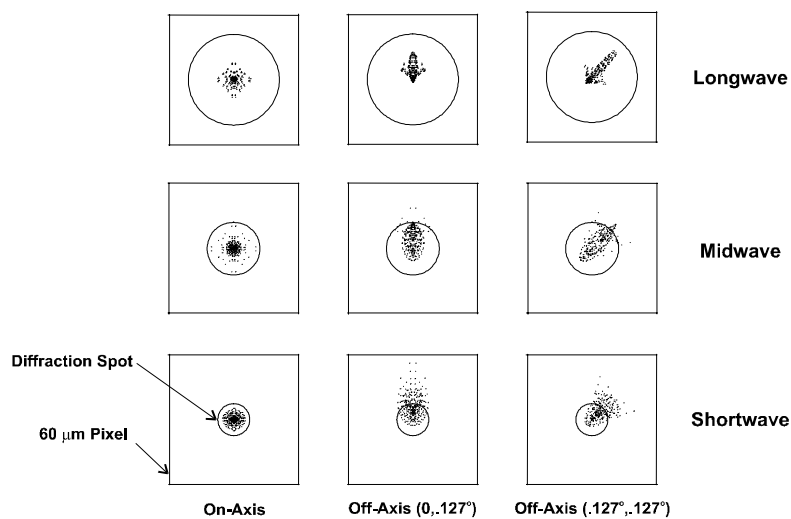


Figure 3-2. Spot diagrams for the infrared channels.

**Visible Performance** Three spot diagrams for the visible channel are shown in Figure 3-3. The image of a single point on the ground is compatible with the 12- $\mu\text{m}$  detector element. There is some image degradation at the corners of the 160 x 160 km field. The performance at the edge of the field would benefit from further optimization of the design.

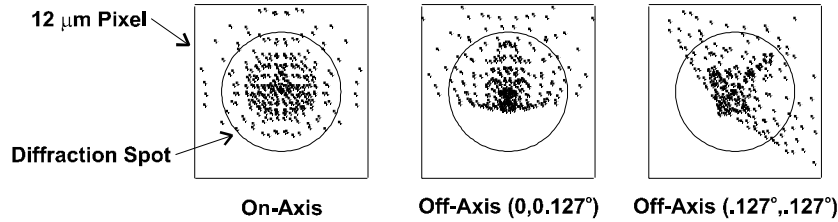


Figure 3-3. Spot diagrams for the visible channel.

### 3.3 DETECTOR POINT-DESIGN

This section briefly summarizes the detector configurations chosen for the ABS point design. An extensive series of trade studies conducted in Sections 4.4, 4.5, and 4.6 led to the selection of three photovoltaic HgCdTe arrays, assumed to be mated via bump-bonding or fanout boards to silicon ROIC's. The selection of photovoltaic detectors was governed by the considerations of Section 4.4. The longwave channel cutoff wavelength (defined as 1.1 times the peak wavelength) was chosen as a result of the simulated temperature and water-vapor retrievals in Section 4.5. The pixel charge-storage and other readout issues are addressed in Section 4.6. The reader is directed to these trade studies for further details. The IR detector focal plane arrays are summarized in Table 3-1

TABLE 3-1

Summary of IR Detector Focal Planes

Property	LW Band	MW Band	SW Band
Cutoff wavelength at 75 K ( $\mu\text{m}$ )	15.1	8.0	4.7
Pixel size ( $\mu\text{m}$ )	60	60	60
Array size (pixels)	16 x 16	16 x 16	16 x 16
Frame rate (Hz)	6000	6000	6000
Charge storage ( $e^-$ )	$2.8 \times 10^8$	$< 2.8 \times 10^8$	$< 2.8 \times 10^8$
$R_0A$ ( $\Omega\text{-cm}^2$ )	3.2	$2.6 \times 10^5$	$4.2 \times 10^{12}$ (est.)
$D^*$ ( $\text{cm } \sqrt{\text{Hz/W}}$ )	$2.14 \times 10^{11}$	$5.87 \times 10^{11}$	$2.13 \times 10^{12}$
NEdT (K), with 250 K blackbody and $f$ -cone-matched optical design operating at peak responsivity wavelength	0.26 at $690 \text{ cm}^{-1}$	0.19 at $1275 \text{ cm}^{-1}$	0.71 at $2150 \text{ cm}^{-1}$
NEdN ( $\text{W}/(\text{cm}^2 \text{ sr cm}^{-1})$ )	0.02 at $690 \text{ cm}^{-1}$	0.09 at $1275 \text{ cm}^{-1}$	0.31 at $2150 \text{ cm}^{-1}$
Estimated operability	99.9%	99.9%	99.9%
Power dissipation	$\sim 30 \text{ mW}^*$	$\sim 30 \text{ mW}^{**}$	$\sim 30 \text{ mW}^{**}$

\* Assumes single output.

\*\* Actual power dissipation is likely to be 15 – 20 mW. Further reduction may be possible via powering-down the focal plane when no “valid data” is being taken (e.g. away from zero path-difference).

The visible channel detector specification follows from Section 4.8, where the determination was made that a single visible channel was capable of performing both cloud-cover imaging for retrievals, and star-sensing for image navigation and registration functions. The visible channel is configured either as a 320 x 320-pixel CCD, or as a larger-format CCD (e.g. 1024 x 1024) with only a 320 x 320 portion located next to the frame-transfer buffer utilized. The reader is directed to this trade study for further details. The visible detector focal plane array is summarized in Table 3-2.

**TABLE 3-2****Summary of Visible Detector Focal Plane**

Property	Visible Band
Pixel size ( $\mu\text{m}$ )	12
Array size (pixels)	320 x 320 (minimum)
Frame transfer shift time for 320 pixels	1 ms
Frame rate	< 1 Hz
Quantum efficiency	0.30 or better
Read noise ( $\text{e}^-/\text{pixel}$ )	18
Dark current at 300 K ( $\text{e}^-/(\text{pixel s})$ )	180

**3.4 MECHANICAL DESIGN****3.4.1 General**

The optical design formed the starting point for the mechanical design. The visible optics may be utilized at the instrument ambient temperature (approximately 300 K). The Infrared (IR) refractive optics following the visible-IR dichroic must be cooled to approximately 220 K to reduce the background flux into the detectors. The IR detectors are cooled to 75 K to reduce the dark current. It is assumed that a yaw-flip maneuver is executed by the satellite at the spring and autumn equinoxes, so that no sun-shield is required around the passive radiator stages, which face alternately north and south. The decision to use passive detector cooling rather than active refrigeration was done to keep the overall package as simple as possible and to keep the electrical power as low as practical.

Figure 3-4 illustrates the layout of the ABS sensor system. It includes the thermal cover enclosing the optics of the sensor and the passive radiator which cools the 220 K optics and 75 K detectors. The ABS sensor would be mounted to the satellite bus structure. It would probably be thermally decoupled as much as possible from the satellite to maintain its thermal control and alignment. Its system-level impacts on the satellite bus comprise its required location (including provisions for seasonal yaw-flip maneuvers), power consumption, mass, and data communication requirements. In addition, a cover is required over the passive radiator which covers the radiating surfaces during the immediate post-launch period while the sensor is outgassing. This cover would then be deployed so that the IR portions of the instrument would be functional – the delay before cover deployment is necessary to avoid contamination of cold surfaces by adsorbed trace gases. The cover is not shown in Figure 3-4. A second cover is required to protect the optics aperture. It is our understanding that the bus contractor will provide this cover, and so it is also excluded from Figure 3-4 and from the instrument mass estimate.

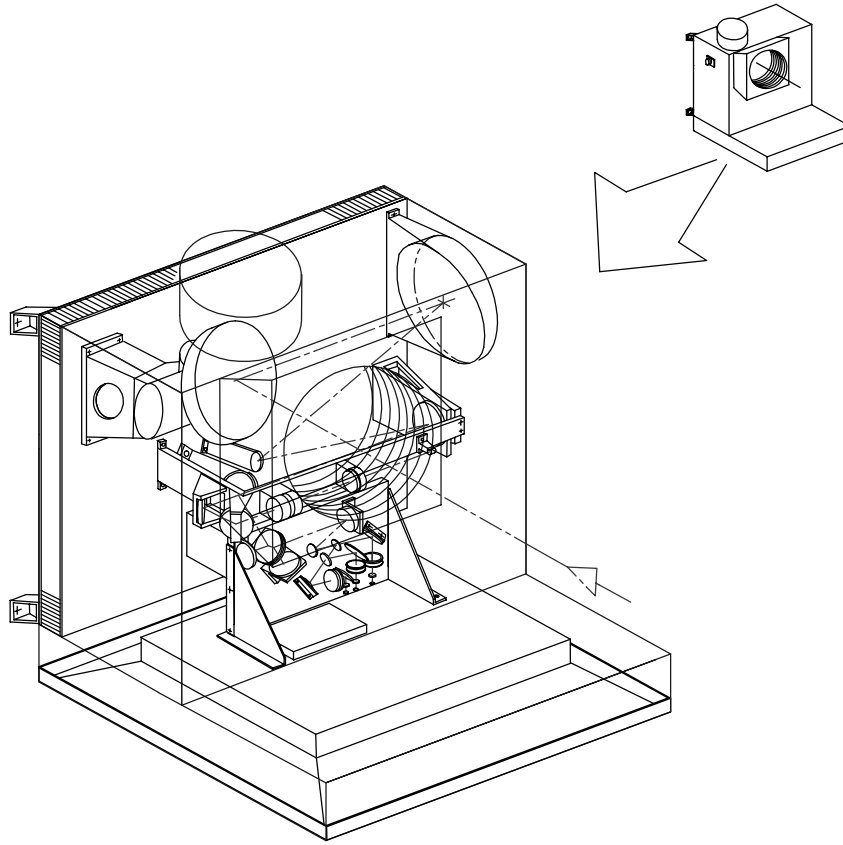


*Figure 3-4. The ABS sensor layout is shown.*

### **3.4.2 Instrument Design Approach**

Figure 3-5 depicts the design approach for the overall optical configuration. An ambient-temperature optical bench supports the scan mirror, telescope, and IR-Visible dichroic as well as the visible detectors. A second optical bench is present which is cooled to 220 K by the outermost stage of the radiative cooler, and which is kinematically supported from the main optical bench at the level of the optical beam. The Michelson interferometer and aft optics (excluding the detectors) are mounted to this bench. The IR detectors are mounted to the coldest (patch) stage of the passive radiator system, which is designed to operate the detectors at a controlled temperature of 75 K. An intermediate stage in the passive cooler isolates the 220 K and 75 K stages.

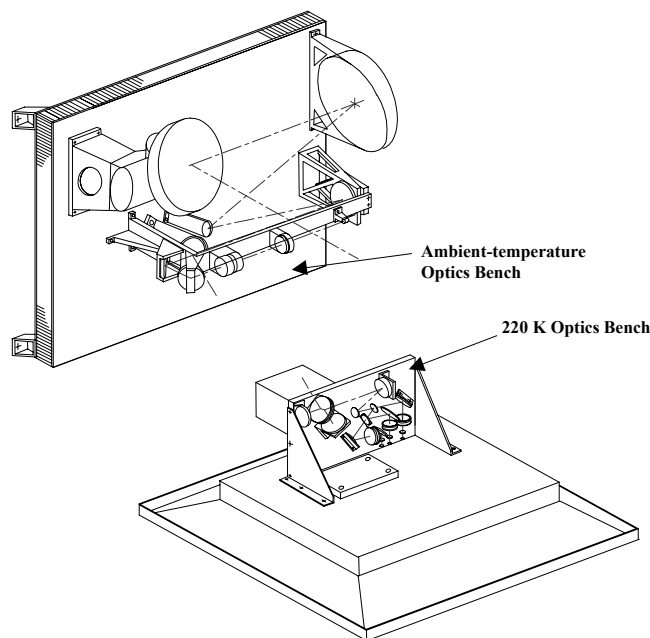


*Figure 3-5. The optical design approach is shown, illustrating the location of the optics on the 300 K and 220 K optical benches. A cover (not shown) would be located over the 220 K optics.*

The stages of the passive radiator are sized using the procedure described in Section 4.7. Facing surfaces are gold-plated to minimize radiative heat transfer. The conduction of heat between stages is determined by the mounts, which are described in detail in the next section. Although sun-shielding is not used as described earlier, it is necessary to incorporate a small shield on the earth-facing side of the radiator to shield the radiating surfaces from reflected and emitted radiance from the earth.

It is desirable to align the optics at room temperature. This requires that alignment be maintained upon cooling to the operating temperature. Alignment of the interferometer to the telescope is maintained by keeping the center of the input face of the beamsplitter fixed relative to the input beam from the visible-IR dichroic. The kinematic supports for the IR optical bench which implement this function are described in Section 3.4.4. The IR optics, mounts, and bench would be constructed from aluminum to make an athermal design in which parts would grow or shrink together with temperature, maintaining their relative alignment. Since three detector focal planes are used, requiring beams originating at the 220 K aft optics and terminating at the 75 K detector optics, differential thermal expansion effects preclude the detectors from simultaneously maintaining alignment upon cooling unless they are mounted to separate 75 K radiators kinematically aligned individually to their respective input beams. The complexity of such an arrangement motivated the decision to mount the detectors to one radiator for alignment and mechanical simplicity. The 75 K stage is kinematically supported from the remaining stages such that the alignment of the long-wave IR detector is maintained relative to the long-wave output beam. The alignment of the two remaining detectors is allowed to shift in proportion to differential thermal expansion effects between the 75 K stage and 220 K bench. This choice was made to maintain the maximum signal for the long-wave detector (which has the lowest signal margin) while still maintaining an adequate signal level for the short and mid wave detectors.



### 3.4.3 Instrument Details

The main support structure for the instrument is the ambient-temperature optical bench. This is assumed to be a honeycomb structure with 0.125" thick aluminum facesheets and an aluminum core 2" thick. A bench 25" x 19" supported at the four-corners with a uniformly distributed weight of 100 pounds would have a first-mode natural frequency of approximately 170 Hz. For the study, a honeycomb plate similar to "breadboard benches" in many catalogues was considered a good choice because of the flexibility of the arrangement of components as the design matures. Depending upon the final configuration it may be preferable to consider machining the optical bench from a solid aluminum plate.

The optical bench is assumed to be covered with a light-tight aluminum housing 0.06" thick, stiffened as required to keep the frequency high enough to not affect the operation of the instrument.

The powered reflecting optics and the optical supports are likewise made of aluminum to provide an athermal design, and to provide for reasonable thermal conductivity and relatively low cost. The mirrors and optical supports were assumed to be solid aluminum with the exception of the scan mirror which directs the incoming beam. The scan mirror must stop and slew frequently, which induces vibrations in the instrument and satellite. To minimize these effects on the satellite, and to minimize the weight of the drive and support system, the scan mirror was assumed to be of 50% lightweighted aluminum. The scan mirror also must view an IR calibration blackbody 90 degrees from the incoming beam, and be able to move the detector field-of-view off the limb of the earth to view cold space for calibration. Therefore, the field-of-regard of the instrument was assumed to be +/- 10 degrees providing for 1.5 degrees beyond the edge of the earth.

An input baffle was included which is approximately 7" long to allow for the mass of this structure to be included in the weight estimate. However, there are times when the sun looks directly up the baffle at the scan mirror. The effect of direct solar impingement on the scan mirror has not been studied in detail at this time, and the length of the baffle will require some study.

The 220 K IR components and mounts are similar to those described above except that the IR-optical bench is assumed to be a 0.5" thick solid aluminum plate, because of its relatively small size, rather than a honeycomb panel.

The 220 K radiator is assumed to be mounted to the IR optical bench with aluminum brackets to provide a rigid support and good thermal conductivity. The 15 W thermal load on this bench, in conjunction with a 0.125" thick 220 K radiator structure having a radial heat path approximately 11" from the mounts to the edge, will produce a temperature gradient between the heat sources and the perimeter of the radiator of approximately 11 K. Under this condition, the space-facing radiating surface of the 220 K radiator stage must really run at ~209 K to cool the optics to 220 K. The impact is that the cooler structure grows approximately 1" larger on each side, which is considered to be an acceptable effect.

The intermediate stage and the patch stage have much lower heat loads to be radiated. With the entire heat load sunk to the center of each stage, assuming a .125" thick stage, temperature gradients of much less than 1 K are expected. Conversely if the stage is only 0.032" thick the temperature drop will be approximately 1 K. The weight associated with these panels must be chosen to maintain a relatively high natural frequency. The weight estimate assumed panels of 0.125" thick aluminum. The patch stage would have a natural frequency of almost 100 Hz using this construction supported at 4 equally spaced points.

### 3.4.4 Kinematic Supports and Thermal Isolators

The supports for the radiators and the 220 K optical bench must be strong enough to support the launch loads, stiff enough to minimize undesirable motion of the instrument components, and sufficient thermal isolators to keep excessive amounts of heat from flowing into the respective stage. As mentioned above it is also desirable to use them as kinematic supports to maintain alignment from warm to cold operation. Figure 3-6 depicts the thermal and mechanical concept used. A fiberglass strip as shown in Figure 3-6 is stiff along its length and width, but flexible through its thickness. They can therefore be used in pairs on opposite sides of a supported item to maintain a stiff support in two directions while remaining flexible in the third. Another pair oriented 90 degrees to the first can support the third direction rigidly. This design effectively resists loads in the three orthogonal directions and the three orthogonal moments. The intersection of lines connecting the pairs of flexures will remain stationary as temperatures change – coefficient of thermal expansion (CTE) effects causing the flexures to deflect in the direction of the thickness of the strip but maintaining a single point stationary. This technique is used between the three stages of the radiative cooler to maintain the alignment of the long-wave IR detector and the long-wave output beam. The fiberglass strips are 1.84" long by .75" wide and 0.033" thick, which provides a thermal resistance of almost 10,000 K/W. There are 8 thermal paths in parallel so that the resulting total would be 1,200 K/W. The heat conducted would be  $\sim 0.8$  mW/K. A temperature difference of 45 K between the two support sides would amount to a heat input of  $\sim 40$  mW which was accounted for in the thermal analyses.

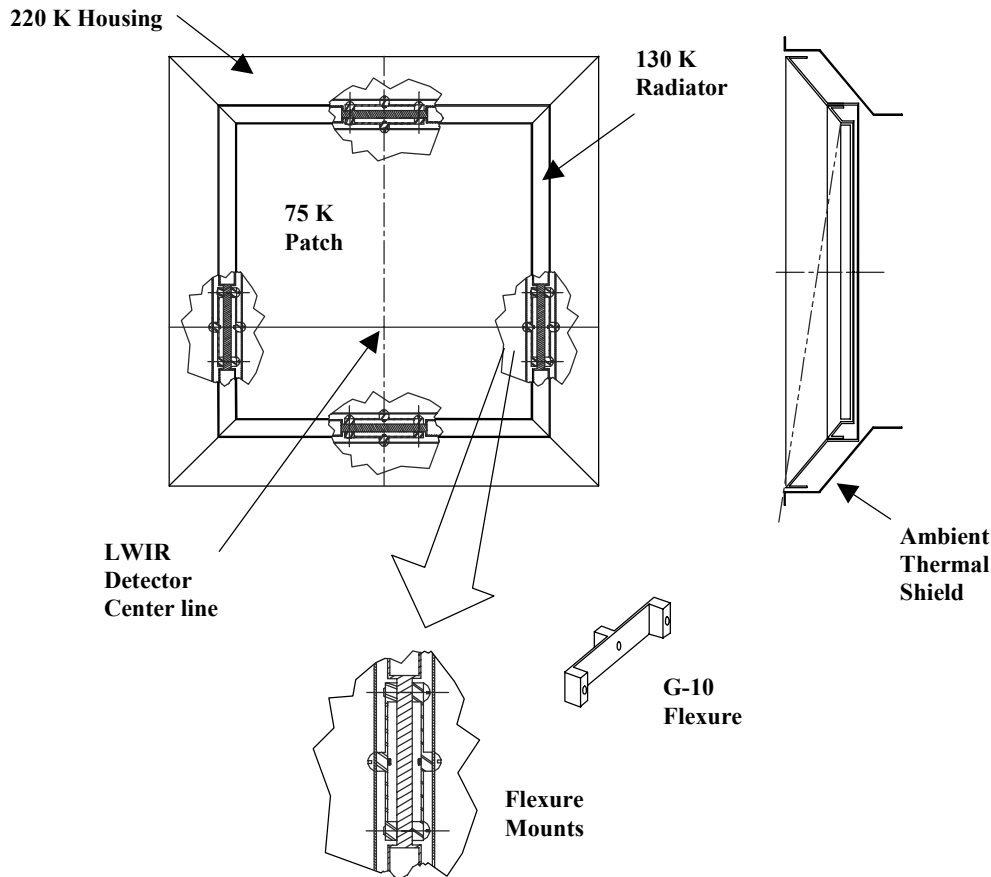


Figure 3-6. The ABS radiative cooler is shown, along with the kinematic mounting concept used to maintain the LWIR channel in alignment. A flexure is detailed below.

The same technique was used to maintain alignment between the incoming IR beam and the IR beamsplitter used in the interferometer except that the flexures were placed perpendicular to a line from the fixed point to the location of the flexure. The flexures were also used in the vertical position in this case rather than horizontal as shown on the radiator concept. The concept for this support structure is shown in Figure 3-7.

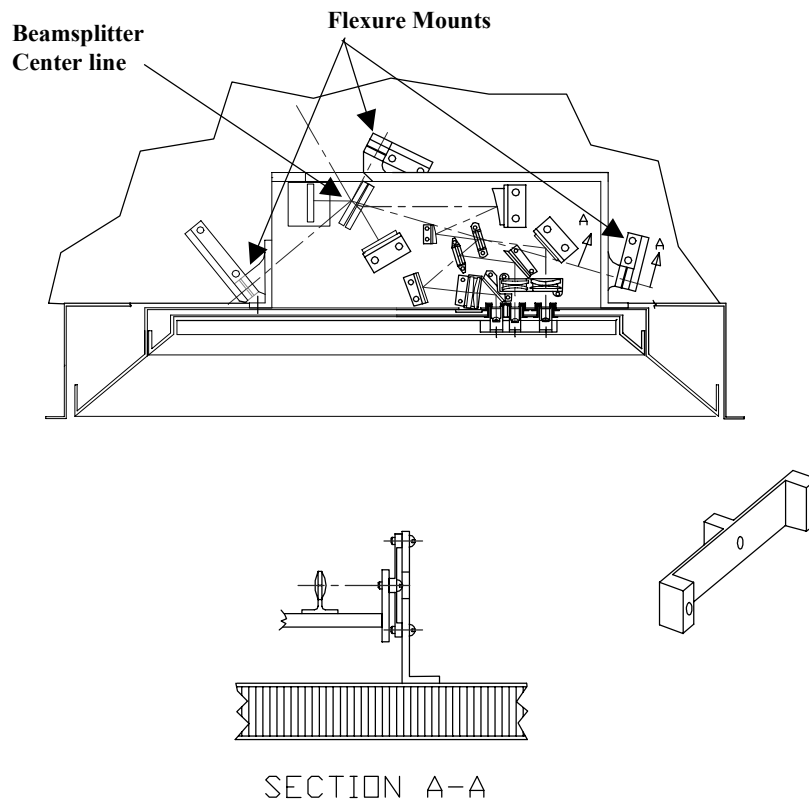


Figure 3-7. The mounting concept used to align the 220 K optics bench and radiative cooler to the 300 K optics is shown.

### 3.4.5 Weight Estimate

A weight estimate for the ABS instrument is shown in Table 3-3. It includes the sensor assembly and the two (redundant) electronic assemblies. The door covering the instrument's input aperture is likewise not included because it is our understanding that this item will be furnished by the satellite bus contractor.

**TABLE 3-3****ABS Weight Estimate**

<b>Item</b>	<b>Weight (lb)</b>	<b>Mass (Kg)</b>
Input aperture cover	-	-
Radiator cover	5.5	2.5
Optical bench (Al honeycomb)	13.8	6.3
IR cold bench	5.7	2.6
Passive thermal radiators	20.3	9.2
Moving-mirror assembly	5.0	2.3
Optics & supports	8.6	3.9
Scan mirror (Al 50% lightweighted)	3.2	1.5
Scan motor assembly & support	13.7	6.2
Blackbody calibration source	1.40	0.6
Housing (Al 0.06" thick)	14.0	6.4
Baffle	5.4	2.4
<b>Sensor estimate</b>	<b>96.6</b>	<b>43.9</b>
Power Supplies	13.2	6.0
Electronics	30.8	14.0
20% Contingency	28.1	12.8
<b>ABS Total weight</b>	<b>169</b>	<b>77</b>

**3.5 ELECTRONICS SYSTEM POINT-DESIGN**

This section presents the proposed point-design for the ABS instrument's electronics system. Figure 3-8 schematically depicts the overall architecture. Each element shown is detailed in a separate subsection below. As discussed in Section 4.9, the general sensor data flow follows a path from very high, unprocessed rates to a final output rate of about ~2.5 Mbps. In addition, the electronics coordinate automatic instrument operation, execution of ground-commandable functions, and collection of housekeeping telemetry data.

All component parts that could be used to build the point-design are presently (9/98) available in space-qualified versions. Servo controllers are shown as implemented digitally, based primarily on successful working prototypes used for MIT Lincoln Laboratory's GHIS brassboard test program. The processor for these GHIS servo systems was a Texas Instruments TMS320c25 DSP chip, which Space Electronics Inc. currently markets in a radiation-hardened, S-class package. Other ABS controllers are shown as analog systems, although TMS320c25 chips could also implement the functions digitally.

The strategy adopted here is neither overly stressing nor particularly risky. Using existing technology, the ABS point-design could nearly fit its output data within the present GOES NO/P/Q bandwidth allocation for the sounder communication link (720 kbps). The ABS instrument proposed here therefore could conceivably fly on the GOES NO/P/Q satellite without any major bus modifications. Moreover, with reasonable design foresight and a comprehensive ground-test program, implementing the electronics as a robust space-qualified configuration would likely prove quite feasible.

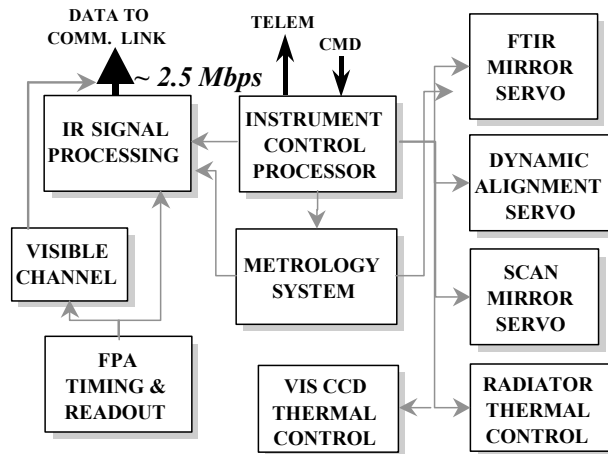


Figure 3-8. ABS electronics system architecture.

### 3.5.1 Instrument Control Processor and FPA Timing/Readout Circuitry

The instrument control processor centrally manages and coordinates all ABS operation. As shown in Figure 3-9, it consists of an 8 (or 16) bit microcontroller and appropriate memory for program code and storage registers. Ground command interpretation, spacecraft/sensor interaction, instrument monitoring, and overall sensor operation are managed within this subsystem.

Drive signals for IR and visible focal plane arrays originate in a digital logic circuit, implemented as a PROM sequencer or within an ASIC gate array. Analog circuitry then converts these digital clocks into appropriate voltage levels for FPA readout, for instance 3 or 4-phase clocks for the visible CCD. Adequate power supply current is budgeted for these analog drive lines.

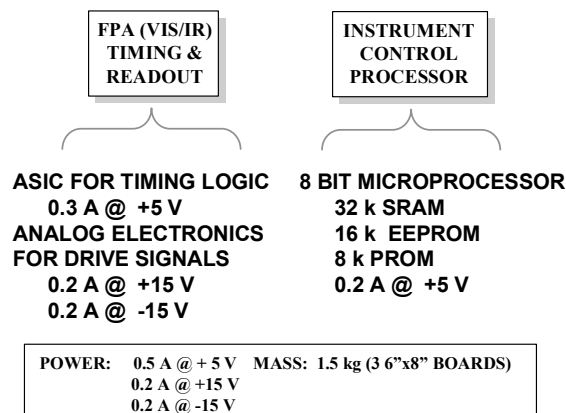


Figure 3-9. Instrument controller and FPA timing/readout.

### 3.5.2 Metrology System

The metrology system acts as principal timer for the FTS moving mirror servo controller, and also generates sampling triggers for the IR channel A/Ds. It uses a reference interferometer that tracks the moving mirror with interference fringes from a monochromatic light source. Based on Lincoln Laboratory experience with GHIS brassboard testing, the ABS point-design proposes using a laser diode

with a 0.8-1.5  $\mu\text{m}$  wavelength. As mentioned in Section 4-9, the lifetime and reliability of this reference source represents an important design concern, as does its in-flight wavelength calibration.<sup>7</sup>

Given this high S/N metrology source, it becomes practical to implement an absolute fringe counting design as follows. The reference interferometer generates linearly polarized light that becomes circularly polarized in one interferometer arm (see Figure 3-10). Separating and then detecting orthogonal polarizations at the interferometer output produces an in-phase signal (I) and a quadrature (90° out of phase) signal (Q).

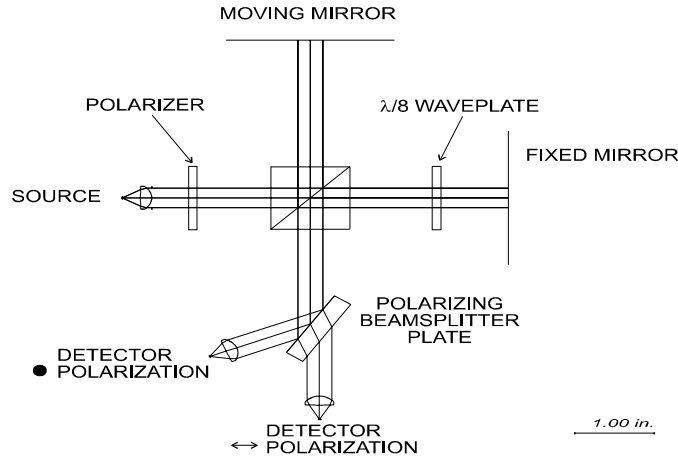


Figure 3-10. Reference Interferometer (conceptual diagram).

Production of I and Q terms is easy to understand by considering vector representations of the electromagnetic fields. Ignoring the waves' time variation, the linear polarized light wave (oriented at 45° to the x axis) is:

$$\vec{E}_l \sim e^{i \cdot \phi_l} \cdot (1, 1), \quad (3-1)$$

while the circularly polarized light wave (with y-component leading by 90°) is:

$$\vec{E}_c \sim e^{i \cdot \phi_c} \cdot (1, e^{i \cdot \pi/2}) = e^{i \cdot \phi_c} \cdot (1, i), \quad (3-2)$$

where the  $\phi$ 's are phase shifts due to different path lengths. The total field at the detectors will be  $E_t = E_l + E_c$ , with an interference term given by:

<sup>7</sup> Measurements from the GHIS project indicated that such a laser's short-term stability was better than 10 ppm; see W. E. Bicknell, et. al., "GOES High-Resolution Interferometer Sounder (GHIS) Brassboard Test Program," MIT Lincoln Laboratory, Lexington, MA, Project Report NOAA-22 (22 July 1998).

$$\begin{aligned}
& \vec{E}_1 \cdot \vec{E}_c^* + \vec{E}_1^* \cdot \vec{E}_c \\
& \sim e^{i\phi_1} \cdot (1, 1) \cdot e^{-i\phi_c} \cdot (1, -i) + e^{-i\phi_1} \cdot (1, 1) \cdot e^{i\phi_c} \cdot (1, i) \\
& = e^{i\phi} \cdot (1, -i) + e^{-i\phi} \cdot (1, i), \text{ where } \phi \equiv \phi_1 - \phi_c, \\
& = (e^{i\phi} + e^{-i\phi}, -i \cdot (e^{i\phi} - e^{-i\phi})) \\
& = 2 \cdot (\cos\phi, \sin\phi); \text{ i.e. I and Q terms.}
\end{aligned} \tag{3-3}$$

A change in moving mirror direction changes the sign of Q relative to I. Clocking an up/down counter with zero crossings of one signal, while feeding the relative sign of the other signal into the UP/DOWN line, would provide an absolute measure of the interferometer's mirror position. The zero crossings also generate clock pulses for triggering the IR signal sampling electronics. Because the crossings correspond to fixed numbers of reference wavelengths, the triggers occur in repeatable OPD positions and thus facilitate sampled interferogram data alignment (e.g. for background subtraction).

Conditioning circuitry converts the I and Q signals out of the detectors into digital logic-level signals. As shown in Figure 3-11, these feed into a quadrature decoder chip that generates trigger and mirror-direction pulses at four times the frequency of either I or Q. Using this decoder rather than feeding the signals directly into a counter thus provides four times greater spatial resolution, and also eliminates susceptibility to glitches and other noise on the I and Q lines. These decoded pulses increment and decrement an 18 bit up/down counter, which is initially reset to zero when the moving mirror is at zero path-difference (ZPD). This count value thus represents the number of reference wavelengths the mirror is from ZPD. A positive count corresponds to location away from ZPD in one direction, while a negative count is mirror position in the opposite direction.

Gating logic generates sampling triggers for the IR channel A/Ds within a specified region around ZPD. This gating is configured to stop data sampling during mirror turnarounds. ADC sampling pulses from this circuitry trigger one-shots with adjustable timing to allow matching the delay through the metrology signal path with the delay through the IR detector signal path. (Mismatched group delays between these two paths contribute to the aggregate instrument NEdN noise.)

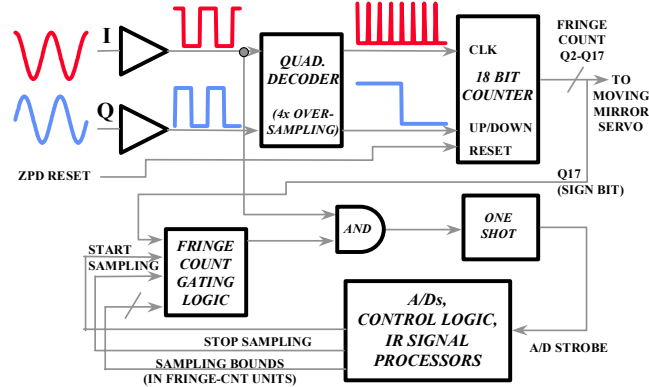


Figure 3-11. Metrology and sampling electronics.

### 3.5.3 IR Waveband Signal Processing

This subsystem comprises the critical processing elements necessary to convert raw detector output signals into a final data stream suitable for transmission to ground. As discussed in Section 4.9, the primary algorithm is a decimating finite-impulse-response (FIR) filter of the oversampled IR

interferogram. Implementation issues include: (1) the number of longwave FPA outputs, (2) modifying detector output signals to permit sampling with 12 bit A/Ds, and (3) obtaining DSP chips/cores with zero overhead to perform single-cycle multiply and accumulate operations.

The longwave IR channel could conceivably require two output analog chains to keep the FPA's readout circuitry tractable. If so, then the signal flow indicated in Figure 3-12 would have two identical paths running in parallel. The main impact of such parallelism would be a slight increase in power consumption as well as a little additional overhead to merge the two data streams. Note that only the longwave channel would need such a modification.

Some of the dynamic range of the IR detectors' response would be due solely to thermal noise rather than true signal. It may be possible to subtract estimates of these thermal noise offsets from each pixel output in the FPA prior to sampling. This scheme would permit using fewer bits for the A/D, say 12 rather than 14, thereby simplifying the task of obtaining fast radiation-hardened A/Ds. Analog Devices, however, does market a 14 bit part (AD9243, S-class version) that samples at 3 MHz and consumes 110 mW of power.

An additional concern is minimizing the processing overhead inside the DSP engine that will be performing the FIR algorithm. Architectural support for zero-wait state memory access and single-cycle MAC operations could strongly influence selection of appropriate DSP chips or cores. Often, the fast throughputs indicated on product specification sheets apply only in restrictive situations using limited buffer memory, so this implementation issue warrants further attention.

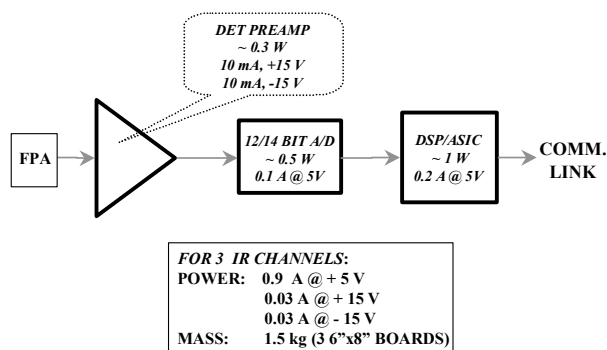


Figure 3-12. IR signal processing chain.

### 3.5.4 Visible Channel Signal Processing

This subsystem comprises a simple analog chain digitized with a 12 bit A/D. See Figure 3-13. A 320 x 320 portion of the CCD chip's output, with suitable analog processing such as correlated double sampling (if necessary), would be sampled at a rate of approximately  $320 \cdot 320 / 3.1 \approx 33$  kHz. With 12 bit samples this would produce a data stream of about 400 kbps, which would then merge with the processed IR data prior to transmission.

The visible CCD would also perform the required star sensing operation for instrument navigation and registration. The instrument controller could readily manage processing of these digitized star-sense signals. No sounding operations need coordination by the controller during the star sense mode, so it could conceivably accommodate flexible tracking/registration algorithms.



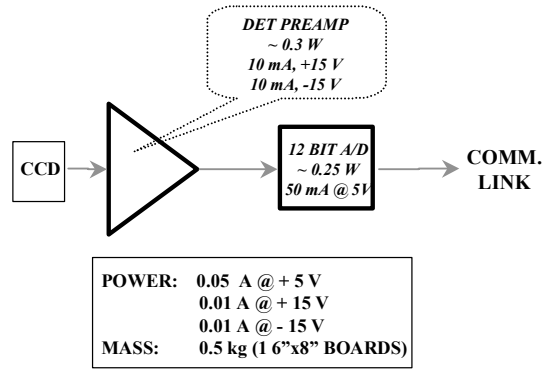


Figure 3-13. Visible channel signal processing.

### 3.5.5 Scan Mirror Servo Controller

The ABS instrument will need a mirror to scan the sensor's 160 km x 160 km ground IFOV over a 3000 km x 5000 km sounding area, as well as to point into cold space or the internal blackbody calibration target. The servo controller necessary to perform this scanning is relatively straightforward, as seen in Figure 3-14. Although shown for a digital implementation, this control loop could also be built as an analog controller using appropriate S-class operational amplifiers.

Probably the component warranting most scrutiny is the feedback sensor. Based on the ABS image-to-image registration requirement of 2.5 km for each pixel, a simple rotary shaft encoder would require  $\log_2(2 \cdot \pi \cdot 36000 / 2.5) \approx 16.5$  bits of resolution. It may be possible to reduce this encoding resolution by using a grid slightly larger than 2.5 km for scan mirror positioning. The servo system could have higher gain at the transition edges between grid squares, and thus could reposition the scan mirror to these coarser grid lines in a repeatable fashion while meeting the 2.5 km image-to-image registration requirement.

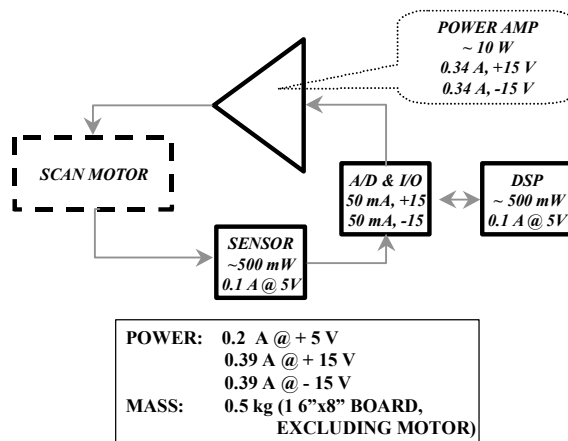


Figure 3-14. Scan mirror servo controller.

### 3.5.6 FTS Mirror Servo Controller

One arm of the ABS's interferometer will travel forward and backward with constant velocity. Figure 3-15 depicts a generalized layout of the servo controller for such a moving mirror. The metrology

system discussed above acts as feedback sensor, providing the servo controller with mirror position information based on the reference fringe count.

MIT Lincoln Laboratory's first GHIS Study Project Report<sup>5</sup> contains details on compensator algorithms and one possible implementation for the FTS servo. Experience with the GHIS brassboard, which used essentially the proposed compensator design, suggests that maintaining velocity constant to within 1% rms is a feasible design goal.<sup>8</sup> A strategy that could possibly simplify the porch-swing is mentioned in the next section.

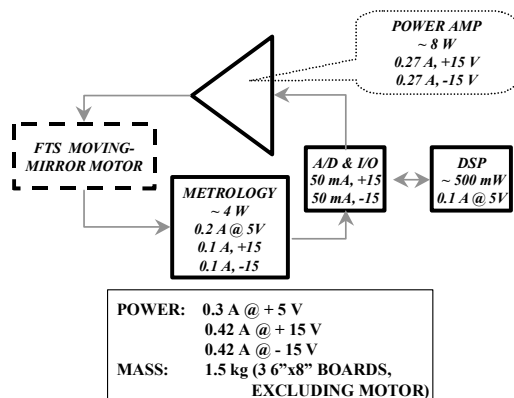


Figure 3-15. FTS mirror servo controller.

### 3.5.7 Dynamic Alignment Mirror Servo Controller

The other arm of the interferometer will need to maintain parallel alignment with the moving mirror during its entire sweep. An actively controlled mirror, as shown in Figure 3-16, could compensate for tilt disturbances induced by low-level vibrations. The closed loop bandwidth required for this controller represents a key implementation concern; it should be the lowest bandwidth compatible with a reasonable projected vibration spectrum.

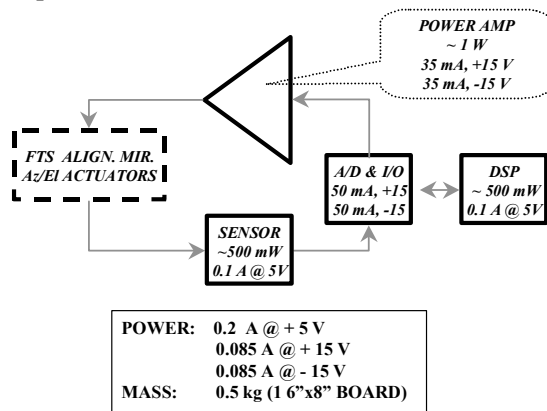


Figure 3-16. Dynamic alignment mirror servo controller.

<sup>8</sup> Bicknell, Project Rep. NOAA-22 (22 July 1998).

How sensitive is the interferometer to tilt disturbances? A straightforward analysis<sup>9</sup> indicates that mirror misalignment will produce a reduction in fringe contrast (i.e. interferometer modulation efficiency) that scales as:

$$2 \cdot \frac{J_1(4\pi\nu\varepsilon R)}{4\pi\nu\varepsilon R}, \quad (3-4)$$

where  $J_1$  = Bessel function of 1<sup>st</sup> kind  
 $\nu$  = wavenumber  
 $\varepsilon$  = mirror tilt  
 $R$  = radius of effective beam aperture.

Using point-design numbers of  $\nu = 1150 \text{ cm}^{-1}$  (highest frequency in longwave channel, which has the largest mirror travel range) and  $R = 0.55$  inches, Figure 3-17 shows the tilt sensitivity. For instance, mirror tilts of less than  $\pm 30 \text{ } \mu\text{rad}$  over a mirror sweep would reduce modulation efficiency by less than 5%.

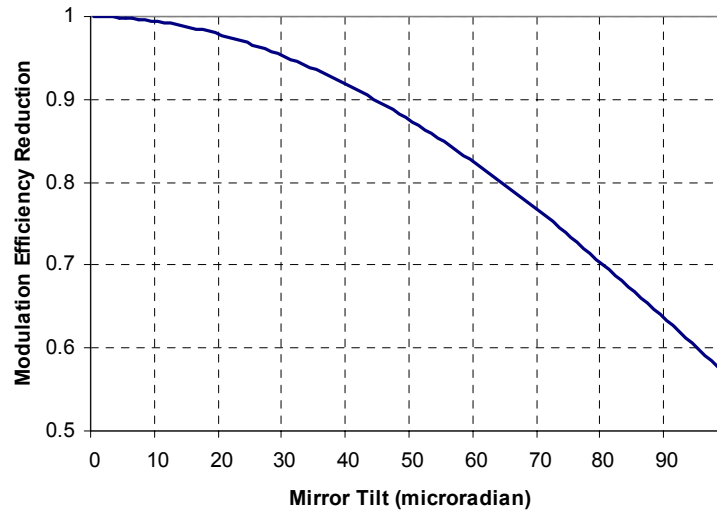


Figure 3-17. Reduction in modulation efficiency due to mirror tilt.

Another interesting option is to use this dynamic alignment system to compensate for velocity variations in the moving mirror. By using the metrology signal together with control actuators that could displace the alignment mirror longitudinally (along the optical axis), it might be possible to relax some constraints on the porch-swing velocity profile, or perhaps even drive the porch-swing with a simple sinusoid. The dynamic alignment mirror's motion would then consist of a superposition of tilt (azimuth and elevation) and linear travel, all coordinated to achieve proper alignment and velocity control. Such a scheme may not prove feasible, but it warrants further investigation if it would simplify the moving mirror's porch-swing control as well as overall interferometer operation.

<sup>9</sup> D. R. Hearn, "Fourier Transform Interferometry," MIT Lincoln Laboratory, Lexington, MA, Project Memorandum 96PM-GOES-0008 (18 August 1995).

### 3.5.8 Visible CCD Thermal Controller

The CCD detector array that would provide simultaneous visible imagery (at 0.5 km resolution) will function best if maintained at a stable temperature. This operating temperature should be low enough to minimize dark current and other thermally induced noise. Figure 3-18 depicts a conceptual design for such a temperature stabilization control loop. Needing minimal complexity and bandwidth for its compensator algorithm, the controller is shown implemented with simple S-class operational amplifiers.

A low-power thermo-electric cooler (TEC) could generate the appropriate thermal stabilization. Sufficient cooling power would result provided that there were a high-temperature (approximately 300 K) sink point available on the spacecraft bus. Using a TEC avoids having to tap into the limited cooling capacity of the radiant cooler, but that is another option if TEC operation proves undesirable.

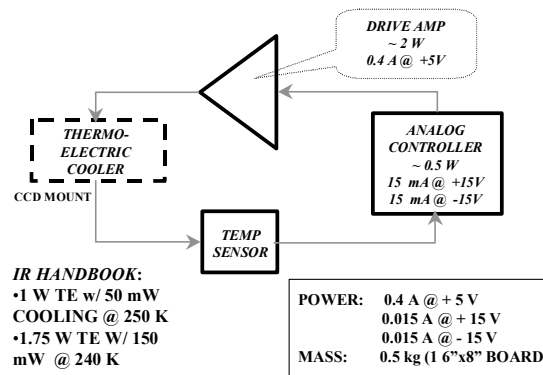


Figure 3-18. Visible CCD thermal controller.

### 3.5.9 FPA Radiant Cooler Thermal Controller

The IR detector arrays must operate at a stable, controlled temperature. Joule heating of the radiant cooler patch, to which the IR detectors are heat-sunk, will operate this stage at a temperature approximately 5 K warmer than the (uncontrolled) patch design temperature. Figure 3-19 shows a simple thermal controller to generate this heating, and thus maintain a stable set-point temperature for the IR FPAs. An analog compensator with S-class operational amplifiers should suffice, though it could be implemented digitally as well.

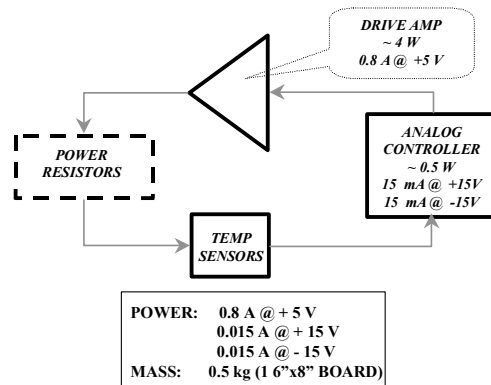


Figure 3-19. FPA radiant cooler thermal controller.

### 3.5.10 Instrument Power Supply

Figure 3-20 shows the power supply necessary to provide the ABS instrument with conditioned power at +5 volts and  $\pm 15$  volts. The conversion efficiency from satellite prime power to sensor power is assumed to be 75%. Interpoint markets S-class DC/DC converters with sufficient output power ratings. To minimize converter switching noise from coupling onto the instrument electronics, the power supply should probably have its own isolated housing.

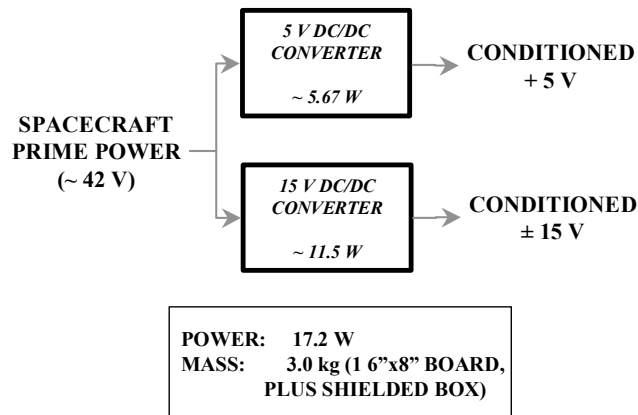


Figure 3-20. Instrument power supply.

### 3.5.11 Electronics System Power and Mass Budget

Each subsystem presented above specifies an estimated power consumption and mass. The projected mass for each electronic PC board includes a pro rata share of the mass for a mechanical enclosure to house all the boards. A separate enclosure is budgeted for the power supply system. Subsystem power allocations are delineated in Table 3-4.

**TABLE 3-4**

**Subsystem Power Allocation**

Instrument Subsystem	Power Estimate (W)
Instrument Controller	1.0
FPA Timing & Readout	7.5
IR Processing	5.4
Visible Processing	0.6
Scan Mirror	12.5
FTS Mirror (including Metrology)	13.5
Dynamic Alignment	3.6
Radiator Thermal Control	4.5
Visible CCD Thermal Control	2.4
Power Supply	17.2
<b>TOTAL</b>	<b>68</b>

The total estimated mass for one electronics box is 7 kg. This comprises 14 PC boards and an enclosure. The point-design assumes that the electronics will be dually redundant, so that there will be another identical electronics box in a power-down standby mode. The projected mass is therefore: 14 kg for 2 electronics boxes, 3 kg for a power supply, 2 kg for cabling, and 1 kg contingency. This represents 20 kg total mass for the entire electronics suite.

Moreover, note that these projections do not reflect any miniaturization efforts. The point-design assumes a low-risk strategy of using standard packaging for components (e.g. DIP, SOIC). Miniaturization could reduce the mass, but does not seem particularly necessary for this application.

### 3.6 ESTIMATION OF ABS DEVELOPMENTAL COST

In this section we estimate the cost of a development program for the ABS. The program consists of a phased development that begins with Phase B in FY2001.

Table 3-5 summarizes the ABS developmental cost by year and lists milestones. The total cost is \$207M. The total includes a 25% contingency in the hardware phases, C and D, but not in Phase B. The cost of Phase B is \$7M per contractor, which is approximately 7% of the program cost through the production of the first ABS flight unit. We assumed two contractors in a competitive Phase B for a cost of \$14M in the total cost. The total cost \$207M does not include the cost to integrate the ABS instrument into the GOES spacecraft.

Table 3-6 gives a breakdown of the ABS developmental cost by subsystem.

**TABLE 3-5**  
**Summary of ABS Development**

2001	2002	2003	2004	2005	2006	2007 GOES Q	2008	Total Cost
Phase B	Phases C & D			Multiple Phase D (Flight Units)				
ABS Flight Units (Completion dates)				1	2	3	4	
Integration of Flight Unit #1 into GOES Q				—	—	— ◇		
\$14M	18.8	24.8	36.1	35.8	35.8	29.8	11.9	<b>\$207M</b>
<b>Notes:</b> <b>Number of Units:</b> Development includes: i) One (1) Qualification Unit, and ii) Four (4) Flight Units. <b>Contingency:</b> Phases C/D include 25% contingency (Phase B has no contingency). <b>Debut of Sensors:</b> Development schedule debuts ABS on GOES Q. <b>Sensor/Spacecraft Integration:</b> Integration of ABS to GOES spacecraft begins Jan. '07, at a time 15 months prior to GOES Q launch availability date of April '08. ABS to spacecraft integration not included in total cost.								

**TABLE 3-6**  
**Breakdown of ABS Cost by Subsystem**

Item	Cost (\$M)
Itemization of subsystems	
<i>a) Scan mirror assembly</i>	1.0
<i>b) Telescope and optics</i>	2.0
<i>c) Housing and structure</i>	0.5
<i>d) Focal plane array</i>	2.0
<i>e) Electronics</i>	4.0
<i>f) Interferometer</i>	2.0
<i>g) Calibration sources</i>	0.2
<i>h) Integration and test</i>	12.0
<i>i) Power supply</i>	0.5
<i>j) Cooler</i>	0.5
<i>k) Thermal control louvers</i>	0.1
<i>l) Sun shield</i>	0.1
Total cost of major components	24.9
Add 15% uncertainty	3.7
Cost of each flight unit	28.6
Cost of four (4) flight units	114.4
Qual unit cost (1.4 x single flight unit cost)	40.0
Four flight units + Qual unit	154.4
Contingency allowance (25%)	38.6
Four flight units + Qual unit + 25% contingency	193.0
Two Phase B contracts	14.0
Total Cost	\$207 M

### 3.7 TECHNOLOGY RISK AREAS AND LONG-LIFE ISSUES

In this section we briefly comment on some aspects of the ABS point design which warrant some attention with respect to risk and/or lifetime. No in-depth work was conducted as part of this study into these topics, but the requirements of Section 2 call for a design lifetime of 9 years to support a 7-year mission duration. The system components listed below are, in our estimation, those for which further examination would be justified to meet these lifetimes.

#### **Interferometer metrology source (near-IR diode laser)**

Risk: Low/Moderate

The ABS requires a monochromatic source (preferably a laser) for timing the interferogram sampling. A long-life flight history does not exist for diode lasers.

#### **Moving-mirror mechanism**

Risk: Low/Moderate

The ABS requires a mechanical “porch-swing”-style mechanism to allow the moving mirror to translate 0.8 cm repetitively. A caging mechanism is also required to prevent motion during launch. Risk-reduction activities have been performed as part of the GHIS and ITS programs, among others, but no long-life flight history exists.

#### **LW IR Detector technology readiness**

Risk: Low/Moderate

The ~14  $\mu\text{m}$  peak wavelength required for the longwave ABS channel is near the limit of current technology for PV detectors at 75 K. Longwave PV detector technology is immature, and lacks a flight history.

#### **Scan mirror motor lifetime**

Risk: Low

GOES-8 and -9 encountered premature failures of motor windings. These windings have been redesigned in subsequent instruments. The 50% smaller ABS aperture places less demands on the scan subsystem in any case.

#### **IR Detectors lifetime**

Risk: Low

The imaging array configuration in ABS does not allow for redundancy. There is no flight history for these arrays.

#### **Visible-channel SNR**

Risk: Low

Aging / irradiation effects on scan-mirror coatings leave GOES visible SNR out of spec after ~5 years. Use of the same coatings would impact the visible channel of ABS, possibly degrading nighttime cloud-imaging and star-sensing operations.

#### **Dynamic-alignment system**

Risk: Low

The use of a closed-loop control system to dynamically maintain the fixed mirror parallel to the moving mirror through its sweep is assumed in this study. If a high-bandwidth control system is needed to implement this function, it would present a technological challenge, and little or no flight history exists.

#### **Reliance on yaw-flip and hemispherical FOV**

Risk: Low

The ABS passive cooling design requires a hemispherical view to cold space. This requires that no solar sail be present on the side of the bus occupied by the radiative cooler. It also requires that yaw flips of the spacecraft be executed at each equinox. Satellite propellant capacity must be able to support periodic momentum-dumping during the mission lifetime. While not an instrument risk, this item is imposed on the bus by the instrument.





## 4. TRADE STUDIES MADE PRECEDING THE POINT DESIGN

### 4.1 OVERVIEW

As stated in Section 1.2.1, the goal of the ABS study was to formulate an instrument point-design meeting the needs of the NWS while avoiding unnecessary risk. While no formal definition of optimization criteria was attempted, the progress of the trade studies was driven by the desire to minimize the size, mass, power consumption, and complexity of the instrument while ensuring that it produce data in accordance with the requirements of Section 2. It was expected that these criteria, along with the use of proven technologies wherever possible, would yield a point design valuable to industry as a basis for further work.

In order to achieve this goal, the instrument was broken down into a collection of functional modules such that each could be individually optimized through a process of trading-off possible design approaches, while bearing in mind the impact these module-level trades have on the overall system performance.

In this section several trade studies are documented which were conducted as the ABS instrument design evolved from a conceptual form to the detailed point-design presented in Section 3. The material in this section serves two purposes: first, it provides much of the background information omitted from Section 3 for brevity; second, it provides justification for the design options selected in converging to a point-design. Although the manner in which design choices made in one subsystem influence the requirements and limitations of other subsystems is not explicitly spelled out in these trade studies, the reader should bear in mind that the iterative method cited in Section 3.1 was a consequence of these often-subtle connections between subsystems.

Each trade study in this section is prefaced by a bulleted list identifying the key points to be addressed in the trade. Section 4.2 compares the performance limitations and cooling requirements of spectrometers based on a diffraction-grating architecture versus a Michelson-interferometer architecture. This trade was carried out to support the choice of an FTS as the basis of the ABS instrument. Section 4.3 details the options considered in the ABS optical design. The following three sections present the trades used to define the IR detector arrays. Section 4.4 considers the radiometric performance of photoconductive and photovoltaic detectors as a function of temperature. Section 4.5 uses predicted retrievals of temperature and humidity profiles to define the longwave detector cutoff. Section 4.6 presents an extensive list of trades which deal with the readout circuits required for the IR arrays. These three sections are closely tied to both the optics of Section 4.3, which must image the ground field-of-view to the detector arrays, and to Section 4.7 which presents passive and active cooling designs for the IR focal planes and aft optics. Section 4.8 details the trades considered in the visible-channel design. Finally, Section 4.9 illustrates the development of a signal-processing architecture to process the data produced by the visible and IR detectors, and prepare it for down-linking.

### 4.2 DIFFRACTION GRATING VS FTS SPECTROMETER

*Key points:*

- *Each approach can produce an instrument capable of meeting ABS requirements.*
- *Textbook “advantages” of the FTS are less relevant than imaging properties and noise considerations.*
- *For comparable SNR, a grating requires more detectors at colder temperature – active cooling of the focal plane is mandatory.*

In Section 4.3 of this report and onward, the assumption will be made that a Fourier-transform Michelson interferometer forms the instrument architecture for the Advanced Baseline Sounder. The purpose of this section is to justify that assumption. While the need for high spectral resolution is clear in order to improve the vertical resolution of retrieved profiles, the best method of obtaining high spectral resolution is less obvious. This section presents the tradeoff between a diffraction grating versus a Fourier transform Michelson interferometer as the architecture of choice for implementing a spectrometer on a satellite platform. Much of the material in this section is based on the work of Beer<sup>10</sup>, and the reader is directed to this source for further details.

#### 4.2.1 Technology Overview

The need for high spectral-resolution images of the earth to support sounding retrievals leads to the consideration of two alternative techniques to obtain such images: the Fourier-transform Michelson spectrometer, (FTS, also called an FTIR for Fourier-transform infrared spectrometer) and the grating spectrometer. Each of these instruments is capable of measuring atmospheric emission spectra with some resolving power  $R$  defined as

$$R = \frac{\lambda}{\delta\lambda} = \frac{\nu}{\delta\nu}. \quad (4-1)$$

Each instrument imposes some optical path difference  $L$  on the incident radiance, whether by a moving mirror in the FTS or a ruled diffraction grating in the grating spectrometer. This leads to a convenient definition of  $R$  as  $L/\lambda$ , the number of wavelengths in the OPD.

These instrument architectures differ fundamentally in the manner in which they encode the spectrum of the observed source and in their performance limitations. A few of the generic differences between the two types of instruments are highlighted in Table 4-1.

**TABLE 4-1**

**General Differences between Grating Spectrometers and Fourier-Transform Michelson Spectrometers**

Characteristic	FT Michelson spectrometer	Grating spectrometer
FOV	Multiple FOV's	Single FOV (echelle grating)
Spectral Resolution	Set by stroke length	Set by detector width
Spectral Range	Set by minimum sampling interval	Set by number of detectors
Coverage Rate	Ndetectors/Tscan	1/Tscan
Dynamic Range	High	Low
Signal Level	High	Low
Moving Parts	Yes	No

In the case of the Michelson spectrometer illustrated in Figure 4-1 the incoming radiation is divided equally between two arms, and is recombined at the beamsplitter producing interference. The beamsplitter is a thin film deposited on a supporting substrate. An identical compensating substrate is

<sup>10</sup> Reinhard Beer, "Remote Sensing by Fourier Transform Spectroscopy," *Chemical Analysis* Vol. 120 (J. D. Winefordner, Ed.), Wiley, 1992.

required to equalize the OPD and dispersion of the two arms. Two images of the scene pixel are produced which have an adjustable optical path difference between them. This OPD is varied by displacing the moving mirror at some constant velocity. At any single wavelength, the interference between the two arms produces a cosinusoidal signal on the detector whose frequency is given by  $2\nu/\lambda$ , where  $\nu$  is the mirror velocity and  $\lambda$  is the wavelength of the radiation. A continuum of wavelengths produces a superposition of such frequencies at the detector, each of which is unique to a spectral component of the scene. This superposition of cosines is referred to as the “interferogram”, and is the acquired time-domain (or equivalently, OPD-domain) signal from the detector, which upon Fourier transformation reproduces the scene spectrum in the frequency (or equivalently, reciprocal-OPD or “wavenumber”) domain.

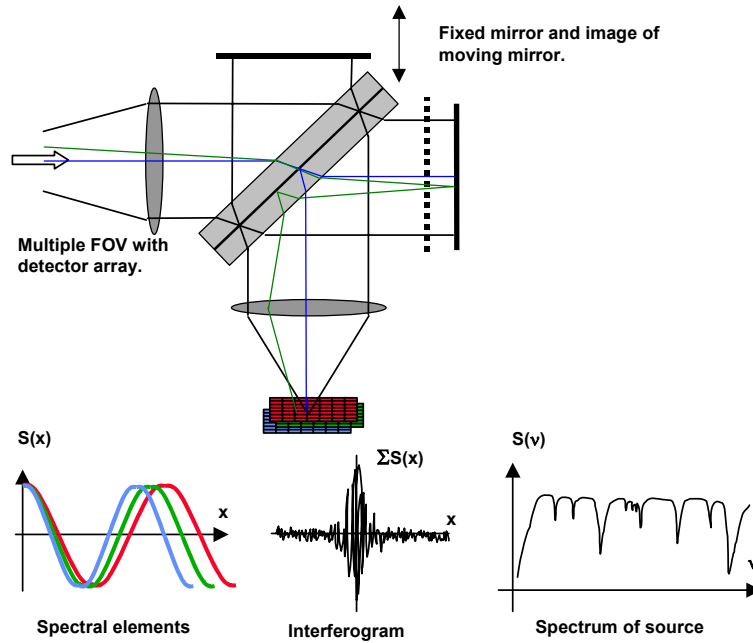


Figure 4-1. The construction of a Michelson interferometer is illustrated at the top. The image of the moving mirror  $M1$  is indicated as a dashed line next to the fixed mirror  $M2$ . The cosines corresponding to different scene wavelengths are shown at the bottom, along with the interferogram obtained by their summation and the spectrum produced by Fourier-transforming the interferogram.

The grating spectrometer, illustrated in Figure 4-2, disperses the polychromatic radiation incident upon it into its constituent wavelengths using a diffraction grating. This encodes the scene spectrum in the angular domain, and requires either a slit to select a wavelength component or uses a line of detectors whose width performs the same function. The use of a blazed grating, as shown in Figure 4-2, results in a large amount of the incident radiation appearing in the diffracted orders of interest. To maximize throughput and resolving power, an “echelle” grating is used<sup>11</sup> in which the order number is  $\gg 1$ . This complicates the optical design because the fringe orders overlap and some additional effort is required to separate the fringe orders spatially. One method of doing this, illustrated schematically in the figure, is to insert additional dispersion into the instrument in the direction orthogonal to that produced by the grating.

<sup>11</sup> Anne Thorne, “Spectrophysics,” 2<sup>nd</sup> Ed. Chapman and Hall, 1988.

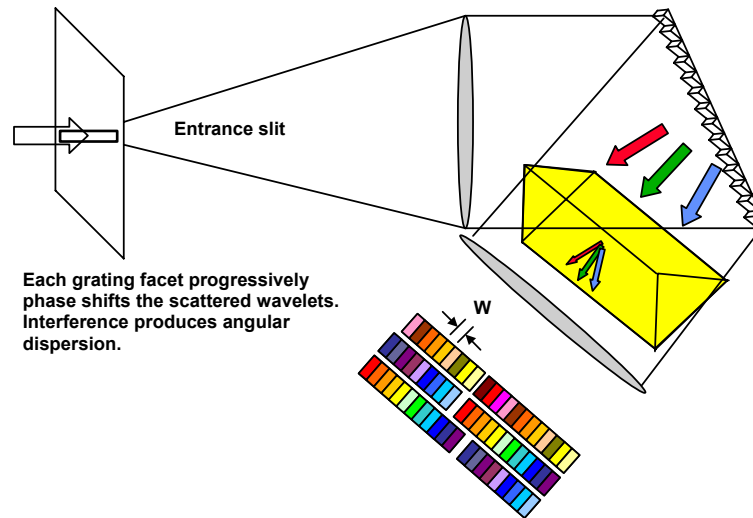


Figure 4-2. An echelle grating is illustrated. The grating determines the spectral resolution, the prism is included to illustrate that some measure is required to separate the fringe orders, which otherwise overlap. The fringe orders are shown imaged to line detectors.

#### 4.2.2 Relative Performance of the Instrument Architectures

In this section, a number of general comparisons will be made between grating and Michelson spectrometers. Only the results are summarized, as the supporting information may be found in Appendix B.

**Conventional Advantages of the FTS.** Two factors are generally cited as the compelling reasons to choose an FTS over a grating instrument; the throughput, or “Jacquinot”, advantage of the FTS and the multiplex, or “Fellgett”, advantage of the FTS. They are named after their discoverers. The first reflects the greater optical throughput which may, in principle, be seen in an FTS instrument, while the second reflects the simultaneous measurement of the source spectrum in an FTS which gives it an integration-time advantage over the sequential measurement of the spectrum in a grating instrument. These advantages generally assume the use of a single detector in each instrument, and the use of a mechanically scanned grating. This makes them more relevant to laboratory instruments than to remote-sensing instruments. A diffraction-limited imaging instrument for the ABS application provides a per-pixel throughput orders of magnitude smaller than that implied by the Jacquinot advantage. An AIRS-type grating instrument overcomes the Fellgett advantage by using a detector array to simultaneously measure the  $M$  spectral-resolution elements of a source pixel.

The trade between these ABS candidate architectures is not made by citing these “textbook” advantages, but rather by factors related to them. The large field of view implied by the Jacquinot advantage allows the FTS to use imaging detector arrays, giving it the large integration-time advantage usually associated with its multiplexing capability. The simultaneous spectral measurement associated with the Fellgett advantage makes the FTS relatively insensitive to thermal carrier generation in the detector because the large population of photogenerated carriers causes detection to be BLIP-limited at higher detector temperatures than is the case with the grating. The effect is to allow the FTS to meet the sensitivity needs of the ABS application with greatly reduced cooling requirements. In summary, the FTS is not inherently *superior* to the grating spectrometer in terms of its sensitivity – it is more *forgiving* in terms of the demands which it places on the detector cooling.

**Integration Time.** We first demonstrate that an FTS may employ a focal plane array to increase its integration time over that available to a grating instrument. Since a grating encodes the spectrum in the spatial domain, and a high-resolution echelle grating requires orders to be separated in the direction orthogonal to dispersion, only one ground spot can be imaged even with a large 2D detector focal plane array. The FTS encodes the spectrum temporally, and so both array dimensions are available for spatial multiplexing in a step-and-stare mode. Figure 4-3 provides an illustration of the imaging modes available to the two instruments. For the assumed ABS coverage rate of 3000 km x 5000 km in 30 minutes, the echelle grating may integrate for 12 ms per ground sample, while an FTS with 16 x 16 imaging arrays may integrate for 3 seconds. The advantage in integration time which is eliminated in an AIRS-type instrument *for a single ground sample* by using a detector array with a fixed grating now reappears due to the ability of the FTS to acquire many ground sample spectra simultaneously. Moreover, the example cited has a detector population of  $\sim 750$  for the FTS and  $\sim M = 1450$  for the echelle grating, a point which will be elaborated upon when cooling is discussed.

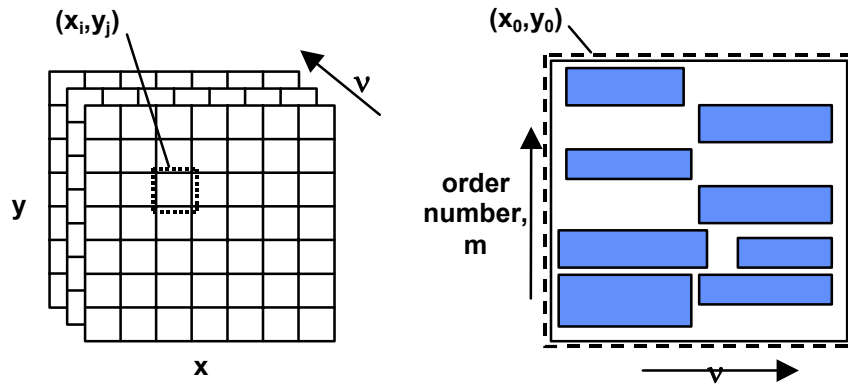


Figure 4-3. The imaging modes available for an FTS (left) and echelle grating (right) are illustrated.

**Instrument Noise and Cooling Requirements.** With the knowledge that the integration time can be substantially larger in an FTS with a detector array than in a comparable grating instrument, a trade between the architectures can be made on the basis of the achievable signal to noise ratio. Noise arises in these instruments from a number of sources, the more important ones being:

- The photon statistics (shot noise) of the scene flux.
- The photon statistics of the instrument background flux.
- The thermal noise of the detectors.
- The electronic noise of the amplifiers and signal processing chain.

Appendix B follows the work of Beer<sup>10</sup> to derive the following highly simplified but illustrative expression for the ratio of the SNR of an FTS and a grating spectrometer

$$\frac{SNR^{FTS}}{SNR^G} \approx \frac{1}{2\sqrt{2}} \sqrt{\frac{\tau_{int}^{FTS}}{\tau_{int}^G}} \cdot \sqrt{\frac{\eta_m (N_{det}^G + \delta\nu \cdot s)}{N_{det}^{FTS} + \frac{\Delta\nu \cdot s}{2}}}, \quad (4-2)$$

where the superscripts of the quantities represent the instrument type to which they apply. The quantity  $\tau$  is the integration time,  $\delta\nu$  is the (small) spectral resolution required for sounding,  $\Delta\nu$  is the (large) spectral bandpass of an FTS waveband,  $s$  is the scene spectral radiance (assumed to be roughly equal in accordance with the earlier conclusion that the throughput is scene-limited),  $N_{det}$  is a measure of the detector noise (thermal electronic noise, and background-induced photocurrent), and  $\eta_m$  is the modulation efficiency of the FTS. What is highlighted in this expression is that the relative SNR of the instruments depends on the time which they spend integrating on each scene pixel, and on the detector noise to which they are subject.

If detector noise  $N$  can be neglected, e.g. if the focal plane is *aggressively* cooled, the grating may have a slight advantage in terms of its smaller spectral bandpass (each detector sees only the flux from a spectral interval of  $\delta\nu$ ) and correspondingly smaller shot noise from the scene and the instrument background. In this case, the relative SNR is of the form

$$\frac{SNR^{FTS}}{SNR^G} \sim \sqrt{\frac{P}{B}} \quad (4-3)$$

where  $P$  is the number of pixels in the FTS field of view, and  $B$  is the width of the FTS waveband expressed as a multiple of  $\delta\nu$ .

In practice, however, the difficulty of achieving very cold detector temperatures means that the design goal should be to operate the focal-plane arrays at the highest temperature at which thermal noise does not overwhelm the other noise sources. This leads to a second FTS advantage: reduced cooling requirements. The FTS spectral bandpass  $\Delta\nu$  is several hundred times larger (228 to 800 times larger in the ABS instrument) than the spectral resolution  $\delta\nu$ . The correspondingly large flux incident on the detector (and large population of photogenerated carriers) causes detection to be BLIP-limited at higher temperatures than for a grating, where each detector receives only the flux in a spectral bandwidth  $\delta\nu$ .

The instrument modeling presented later suggests that ABS can operate at 75 K to 80 K, whereas the AIRS grating instrument is cooled to 58 K. Moreover, the trades carried out later in this report suggest a detector population of  $\sim 750$  for the ABS point design, versus  $M \sim 1450$  for a grating instrument. The necessity of a large amount of cooling capacity for a grating instrument is evident. As discussed in Section 4.7, passive cooling is limited to modest focal plane temperatures and heat loads, and is not practical with a grating instrument. The use of small pulse-tube coolers discussed in Section 4.7 is likewise not feasible. Mechanical refrigerators which can sink substantial amounts of power at  $T \sim 60$  K are available, but consume about 75 Watts of conditioned power, and weigh approximately 10 kg each. The ABS sounding requirements may be met with a smaller, lighter instrument, and with less power consumption, if an FTS is used as the architecture for the instrument.

### 4.3 OPTICS TRADES

*Key points:*

- *Interferometer acceptance angle and diameter must be selected to minimize self-apodization*
- *ZnSe may be used in place of KBr for the beamsplitter*
- *Reimaging vs. non-reimaging telescope design, & implications for mirror size*
- *Field-imaging vs. pupil-imaging back optics, and catadioptric vs. reflective design*

For the purposes of the design trade study the parameters listed in Table 4-2, which are repeated from Section 2, were assumed. A physical mirror sweep (full) of 0.8-cm is used to obtain the desired spectral resolution. For the initial baseline design study, an input aperture of 6 inches was selected. Excursions from the baseline aperture diameter were allowed.

**TABLE 4-2**  
**Assumed Parameters**

Parameter	Value
Nominal Wavebands: Shortwave	3.68 - 4.65 $\mu\text{m}$
Midwave	5.75 - 8.26 $\mu\text{m}$
Longwave	8.70 - 15.38 $\mu\text{m}$
Ground Sample Diameter	10 km
Minimum Ground Field-of-View	60 x 60 km
Interferometer Mirror Sweep (full)	0.8 cm

#### 4.3.1 Interferometer Acceptance Angle

The interferometer is subject to self-apodization, which reduces the modulation of the interferogram as the angle of incidence on the interferometer increases. For good contrast the rule-of-thumb is that the modulation should be maintained at a level above 0.65. The modulation is given by

$$\text{modulation} = \sin(\Omega l \sigma / 2) / (\Omega l \sigma / 2), \quad (4-4)$$

where  $\Omega$  is the solid angle,  $l$  is the maximum OPD due to the mirror sweep, and  $\sigma$  is the wavenumber. The solid angle,  $\Omega$ , is given by

$$\Omega = \pi \sin^2 \theta, \quad (4-5)$$

where  $\theta$  is the interferometer half-angle.

During instrument operation, the interferogram is sampled for the full sweep (max OPD = 1.6 cm) in the longwave channel, half of the sweep in the midwave channel and a quarter of the sweep in the shortwave channel. Figure 4-4 shows the modulation as a function of interferometer half angle for the end points of each waveband. The horizontal line represents the desired minimum modulation of 0.65. As can be seen from the figure, the lowest modulation occurs at the short wavelength end of the longwave channel, i.e. a wavenumber of  $1150 \text{ cm}^{-1}$ . At interferometer half angles greater than 1.325 degrees, the modulation for a wavenumber of  $1150 \text{ cm}^{-1}$  is below 0.65. The maximum allowable interferometer half angle is therefore set at 1.325 degrees in further trade studies.



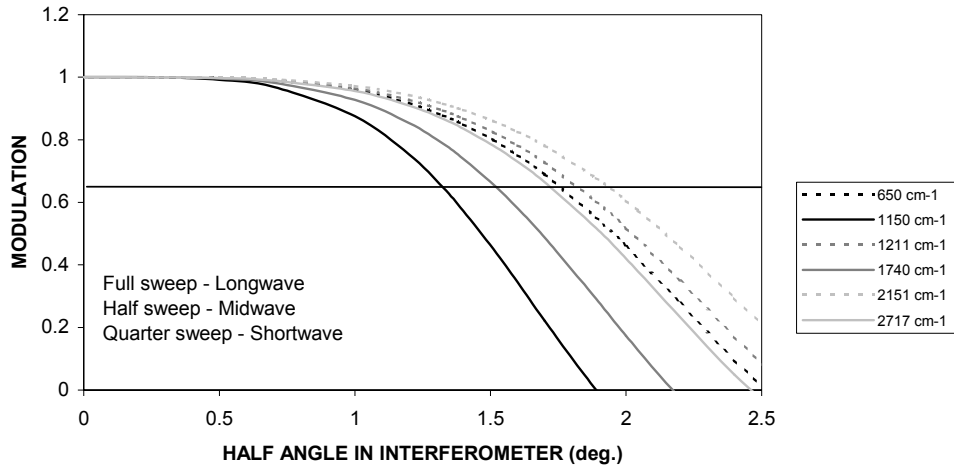


Figure 4-4. Modulation vs. half angle in Interferometer.

#### 4.3.2 Interferometer Aperture Diameter

The input optics in the ABS optical system are afocal. The half angle in object space, which defines the field-of-view on the ground, is related to the half angle in the interferometer by the ratio of the telescope aperture and the interferometer aperture. Systems with 6-inch and 8-inch collecting apertures were considered. As discussed in the previous section, the interferometer half angle should not exceed 1.325 degrees. If the 10-km ground sample diameter is used to size the interferometer aperture, the minimum interferometer aperture diameters are 0.051 and 0.068 inches for 6-inch and 8-inch collecting apertures respectively. Use of these very small collimated beam diameters leads to large angles in the interferometer (due to the instantaneous field-of-view of the optical system with the focal plane array). For a 6-inch collecting aperture system with the 160 x 160 km ground field-of-view and collimated beam diameter of 0.051 inches at the interferometer, the angle-of-incidence on the interferometer beamsplitter would be  $30 \pm 21.2$  degrees. For an 8-inch collecting aperture system with the 100 x 100 km field-of-view and an interferometer collimated beam diameter of 0.068 inches, the angle-of-incidence on the interferometer beamsplitter would be  $30 \pm 13.3$  degrees.

In the nominal design, the interferometer end mirrors are approximately four inches from the aperture stop and the beamsplitter input face is approximately 5.5 inches from the aperture stop. The interferometer components must be made large enough so that there is no vignetting of the field-of-view. Figure 4-5 shows the interferometer mirror diameter and the interferometer beamsplitter diameter (including the effect of the 30-degree angle-of-incidence) required to accommodate the field-of-view for both the 6-inch and 8-inch collecting aperture optical systems. For the 6-inch system, the minimum beamsplitter diameter of 1.052 inches corresponds to an interferometer collimated beam diameter of 0.456 inches. For the 8-inch system the minimum beamsplitter diameter of 0.961 inches corresponds to a 0.416-inch interferometer collimated beam diameter. A standard component diameter of 1.5 inches was selected for the beamsplitter. To minimize the angles-of-incidence on the interferometer beamsplitter, the largest collimated beam diameter that is compatible with the 1.5-inch component was selected. For the 6-inch collecting aperture instrument, the choice was a 1.1-inch interferometer collimated beam diameter. This selected diameter was used for both the 6-inch and 8-inch collecting aperture systems.

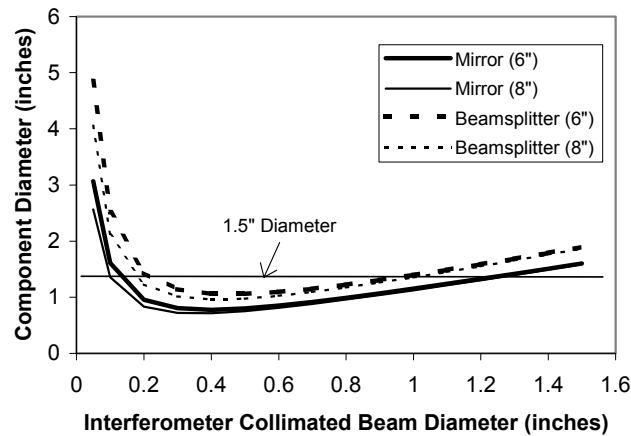


Figure 4-5. ABS Interferometer component diameters.

#### 4.3.3 Beamsplitter Material Selection:

Two materials were considered for the interferometer beamsplitter and compensator. The first was potassium bromide, KBr, and the second was zinc selenide, ZnSe. KBr is a salt with good transmission across a broad spectral range. The material has the drawback of being a hygroscopic material that requires special polishing, handling and storage conditions. ZnSe is a robust polycrystalline material that does not require special handling. It does not, however, have the broad spectral range that KBr has.

Figure 4-6 shows the interferometer transmission as a function of wavelength for the two materials being considered. For these calculations it was assumed that the beamsplitter and compensator plates were 0.2-inches thick, that the beamsplitting surface had a 60-40 splitting ratio, that the non-beamsplitting surfaces had 4% reflection (uncoated KBr or AR coated ZnSe), and that the interferometer end mirrors had 95% reflection. For the shorter wavelengths (up to 13  $\mu\text{m}$ ), performance is comparable for the two materials. At longer wavelengths, the effect of the absorption of the ZnSe substrates can be seen. For systems with cutoff wavelengths longer than 16  $\mu\text{m}$ , the choice of KBr is clear. The ABS system has a long wavelength cutoff of 15.1  $\mu\text{m}$ , as determined in Section 4.5. Although there is a transmission falloff at that wavelength, it was decided that the transmission losses were outweighed by the advantages that the more robust material provides. ZnSe was selected as the beamsplitter material for the ABS point design.

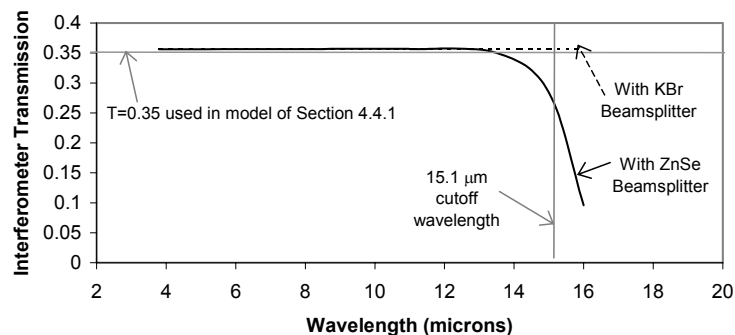


Figure 4-6. ABS Interferometer transmission.

#### 4.3.4 System $f$ Number

The detector array pixel size and the selected input aperture determine the final system  $f$ -number. Two detector pixel sizes were considered for this system; a 50- $\mu\text{m}$  pixel and a 60- $\mu\text{m}$  pixel. The ground sample diameter was fixed at 10-km. Figure 4-7 shows the required system  $f$ -number as a function of input aperture for the two detector pixel dimensions.

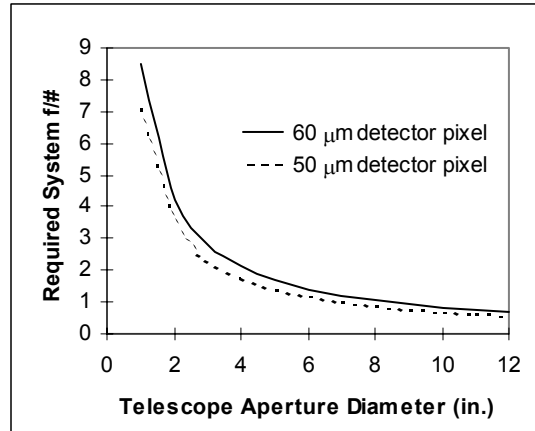


Figure 4-7. System  $f$ -number.

From Figure 4-7 it can be seen that for a given aperture diameter a faster  $f$ -number is required if a 50- $\mu\text{m}$  detector pixel is used. For ease of design, a 60- $\mu\text{m}$  pixel was selected. For a collecting aperture diameter of 8 inches, an  $f/1$  optical system is required. In the design process, an effort was made to keep the system operating slower than  $f/1$ . From Figure 4-5, the 8-inch telescope aperture is compatible with the selected 1.1-inch interferometer aperture diameter and a 16 x 16 array. There is, however, little margin above the recommended 0.65 modulation. If the input aperture were made larger than 8 inches, then it would be necessary to increase the interferometer aperture diameter or sacrifice instantaneous ground field-of-view.

#### 4.3.5 Input Telescope

Two collecting aperture diameters were considered in this study, 6-inch and 8-inch. The 6-inch system has a 160 x 160 km instantaneous ground field-of-view and the 8-inch system has a 100 x 100 km instantaneous ground field-of-view. The input telescope is an afocal optical system that accepts the collimated 6 or 8-inch input beam and produces a 1.1 inch diameter collimated beam. The interferometer imposes an additional constraint on the input telescope: Because of the moving mirror in the interferometer, a hard aperture stop is required after the interferometer. If the input telescope does not have an internal image, the field-of-view of the optical system causes the beam footprints on the primary and the scan mirrors to be large. In the case of a reimaging telescope, an image of the aperture stop can be formed at the primary mirror, the scan mirror or the calibration source. Figure 4-8 shows examples of the two input telescope configurations with 8-inch collecting apertures. The schematic on the left of the figure shows a two-mirror, non-reimaging telescope. The beam footprint on the primary mirror for the point at the center of the field-of-view has a diameter of 8 inches. If the 100 x 100 km field-of-view is used, the primary mirror diameter must be increased to 13.1 inches. The schematic on the right of Figure 4-8 shows a three-mirror, reimaging telescope. Although the two configurations both have the same 100 x 100 km field-of-view, the reimaging telescope has a smaller primary and will require a smaller scan mirror. If the image of the aperture stop is at or near the calibration source, each pixel in the detector will view the same area on the calibration source. This is considered to be a positive feature in the calibration process. The three-mirror telescope configuration has been selected as a baseline.

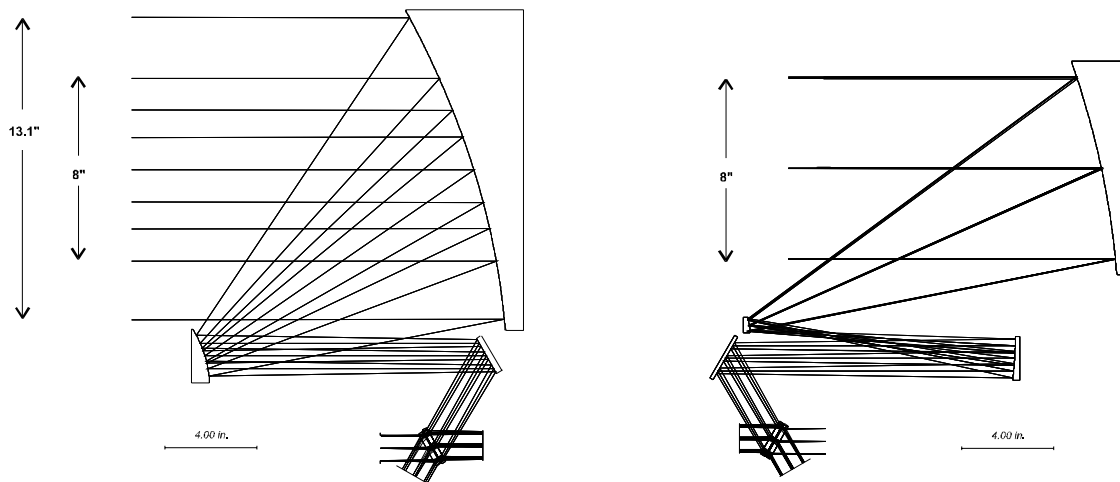


Figure 4-8. Comparison of non-reimaging and reimaging input telescopes.

Figure 4-9 shows the input telescopes for both a 6-inch and an 8-inch collecting aperture. The 8-inch system has the advantage of collecting more scene flux. The 6-inch system has the advantage of smaller volume. Although the telescopes can be designed to have the same field-of-view, the instantaneous ground field-of-view for the 6-inch system is set at 160 x 160 km and that for the 8-inch system is set at 100 x 100 km. The 6-inch telescope was selected as a baseline since it has an adequate collecting aperture, a smaller volume and a wider field-of-view.

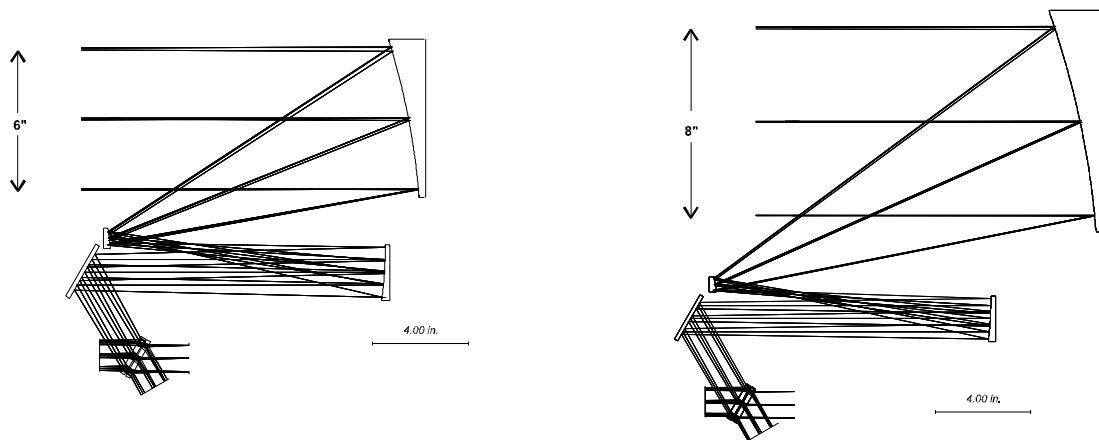


Figure 4-9. 6-inch and 8-inch collecting aperture telescopes.

#### 4.3.6 Aft Optics

The aft optics have a 1.1-inch diameter aperture stop at their input. The radiation is divided into shortwave, midwave and longwave bands by dichroic beamsplitters. It is desirable to minimize the angle of incidence on the dichroic beamsplitter to reduce the wavelength shift caused by the variation in the angle of incidence on the filter. Two trades were considered in the aft optics: pupil vs. field imaging and reflective vs. refractive optics.

**Pupil vs. Field Imaging.** Historically, a pupil imaging system has been used in the GOES sounder. If the pupil is imaged onto the detector, ground information from any point within the selected field-of-view is uniformly distributed across the detector. Such a system is relatively insensitive to detector non-uniformity, since the possibility that a “hot spot” in the FOV may image onto a particularly sensitive region in the detector is eliminated. Detector non-uniformity is a substantial problem with photoconductive detectors due to minority-carrier sweepout effects. This is not generally the case with photovoltaic detectors, arrays of which have been selected in Section 4.4 for the ABS baseline design.

Optical designs for both pupil imaging and field imaging systems were considered. A schematic of the field imaging system is shown in Figure 4-10. In order to reduce the background radiation reaching the detector, an efficient cold stop is present just before the cold detector. An optical system with an intermediate field image is used so that the aperture stop can be imaged onto the cold stop.

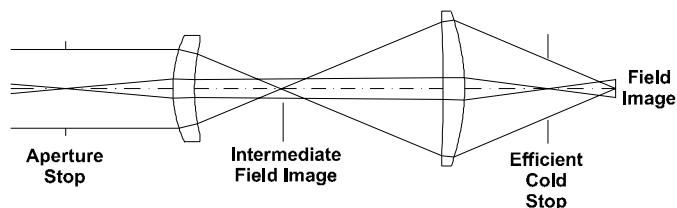


Figure 4-10. Schematic of field imaging optics.

If a pupil imaging system were selected, a cold field stop would be used to limit the background radiation reaching the detector. This is shown schematically in Figure 4-11a for an optical system with a single detector. The cold field stop is located at the image of the ground. The detector is located at the image of the aperture stop. The optical system becomes more complicated if a detector array is substituted for the single element detector. Each detector element must have an independent lens to image the entire pupil onto the detector element. This is shown schematically in Figure 4-11b for a three-detector array. The rays shown as dashed lines emanate from the central ground patch. The bundle of rays fills the aperture stop, uses only the central portion of the imaging lens, and forms an image of the central ground sample on the central element of the field lens array. An image of the entire aperture stop is formed on the detector behind the field lens element. The rays shown as thin solid lines emanate from a neighboring ground patch. This bundle of rays also fills the entire aperture stop, but uses the upper portion of the imaging lens. An image of the associated ground patch is formed on the top element of the field lens array. An image of the entire aperture stop is formed on the detector behind the field lens element.

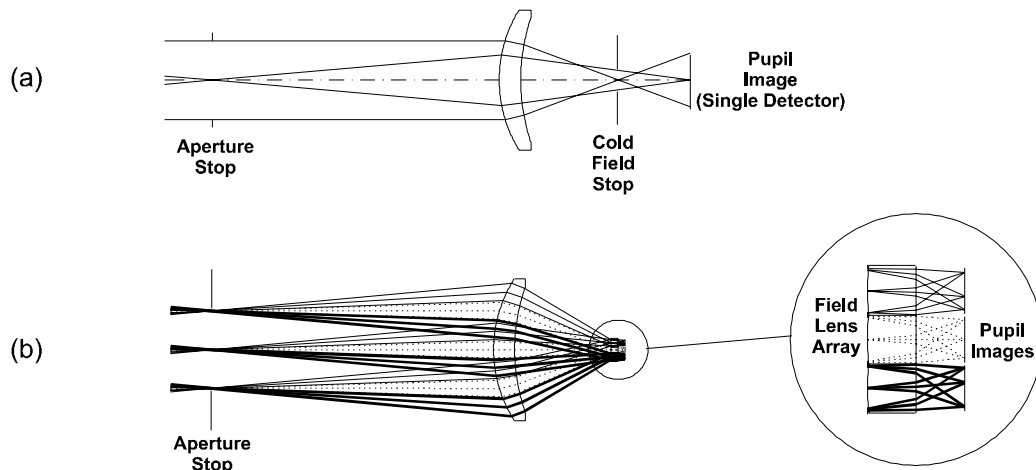


Figure 4-11. Schematic of pupil imaging system for (a) single detector and (b) array.

In order for the pixel pitch to match the detector pitch, the imaging optics must form an image with elements whose size matches that of the detector element. For an array with abutted 60- $\mu\text{m}$  detector elements, the field lens elements shown in Figure 4-11b would need to be 60  $\mu\text{m}$ . The lens elements would be fabricated as a microlens array integrated with the detector array. An alternative, which would allow the microlens array and the detector fabrication to be decoupled, is shown in Figure 4-12. This is a working design for the shortwave channel. The microlens array is located at the intermediate field image. This system requires a well-corrected, telecentric intermediate image. In Figure 4-12, the microlens element is twice the size of the detector pixel. A pupil image is formed by each microlens element. The pupil images could be located on the back of the microlens substrate if the array substrate were thin. For fabrication purposes, a thicker substrate would be preferred and the images would be located within the substrate. These images are then relayed onto the detector pixels by the 2x relay. This same optical system can be used as a field imaging system if the microlens array is removed and a small adjustment is made to the spacing between the imaging optics and the relay.

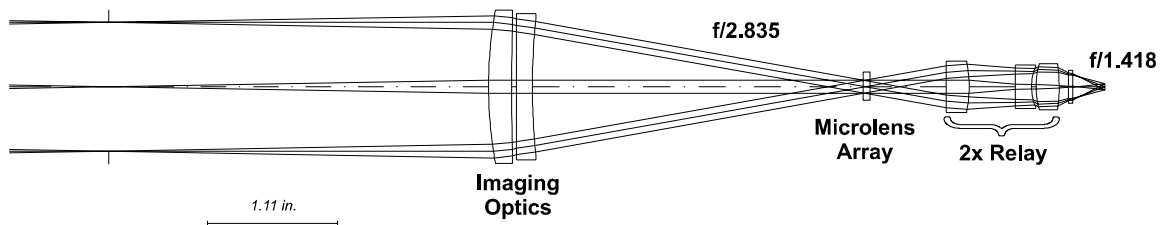


Figure 4-12. Pupil imaging system with microlens array at intermediate image.

Optical systems for either field imaging or pupil imaging aft optics are feasible. The field imaging system was selected since it does not require a microlens array and would be easier to implement. The focal length of the aft optics is selected such that a 10-km ground sample diameter is imaged onto the selected 60- $\mu\text{m}$  pixel.

**Catadioptric vs. Refractive Optics.** Refractive and catadioptric aft optics which are compatible with the 6-inch aperture design with a 160 x 160 km ground field-of-view are shown side by side in Figure 4-13. For compatibility with the cooler, the shortwave, midwave and longwave detector arrays were kept in a common plane. Either aft optics design form can be used.

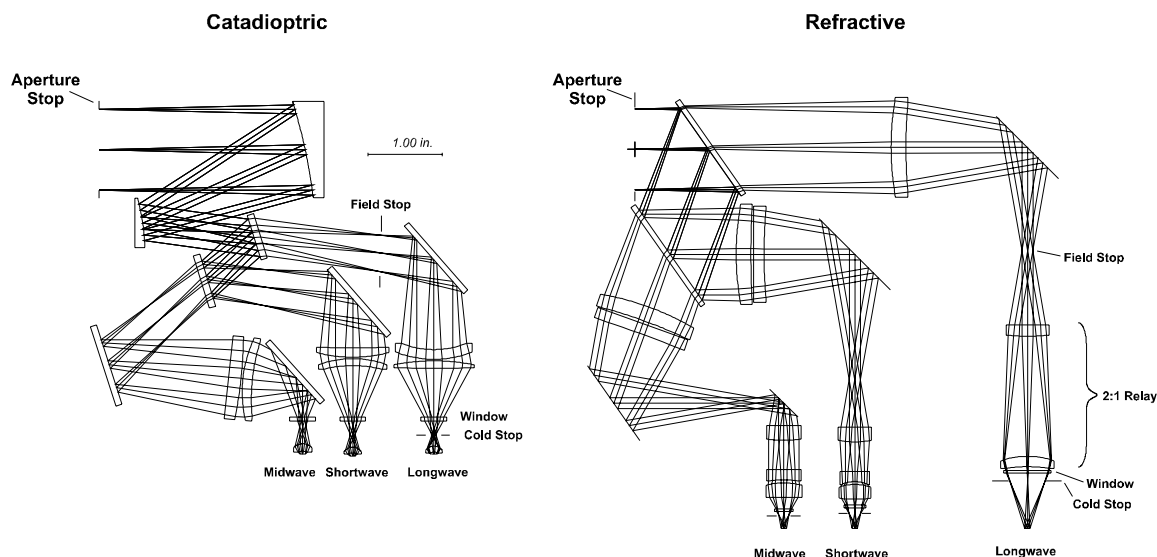


Figure 4-13. Comparison of catadioptric and refractive aft optics.

The catadioptric design form was selected for the point design since it is more compact, is slightly easier to athermalize, has comparable transmission and has common reflective elements forming an accessible intermediate image in each channel. It has slightly larger angle of incidence on the dichroic.

#### 4.4 DETECTOR FOCAL PLANE ARRAY OPTIONS

*Key points:*

- Photovoltaic detectors are required for large arrays
- 65 K is sufficient for LWIR detector to be BLIP-limited, 75 K is near-BLIP
- MWIR and SWIR detectors may be operated up to 100 K and 140 K respectively

One of the key trades in the design of any infrared system is the specification of the detectors. Parameters such as the material, cutoff wavelength, operating temperature, pixel size, detectivity, and readout are intimately connected with the optical and electronic design of the instrument and cannot be carried out entirely independent of these system-level trade studies. The primary objective of this study was to examine the lower bound on the instrument performance, which is determined by the noise characteristics of the detectors. We compared the performance of photoconductive (PC) vs. photovoltaic (PV) detectors in the longwave channel and studied the effects of using relatively large two-dimensional arrays. This section delineates the process by which the detector parameters were chosen.

##### 4.4.1 Inputs to the Instrument Model.

We modeled a baseline design of the sounder to choose the detector parameters. Although a more detailed model encompassing optical, mechanical, and electrical effects (described in Appendix C)

is required to predict the total system noise, this study focused on detector limited instrument performance. Detector limited performance is obtainable in a real instrument. The spectral band, detector cutoff wavelength, spectral resolution, total photon flux, stare time, aperture area, array size, field-of-view, and optical transmission are instrument parameters which determine the detector limited performance. Most of the baseline parameters for this study were derived from a previous study<sup>12</sup>. Previous experience from other programs also helped determine some of the optics transmission and emissivity characteristics that were used in the model. A list of inputs is summarized in Table 4-3.

**TABLE 4-3**  
**Instrument and Satellite Parameters**

<b>Satellite Altitude (km)</b>	35800		
<b>Ground Sample Diameter (km)</b>	10		
<b>Extreme Field Offset (km)</b>	Trade (Section 4.6)		
<b>Aperture Diameter (cm)</b>	Trade (Section 4.6)		
<b>Band</b>	LW	MW	SW
<b>Spectral Band (cm<sup>-1</sup>)</b>	650 - 1150	1250 - 1740	2150 - 2720
<b>Spectral Resolution (cm<sup>-1</sup>)</b>	0.626	1.25	2.5
<b>Stare Time (s)</b>	Trade (Section 4.6)		
<b>Scene Temperature (K)</b>	270	270	270

Items labeled trade in the table were to be determined in the course of the system trade studies. Relevant sections for each trade are indicated in ( ). Notional values were used when necessary during the detector trades. The extreme field offset is determined by the array size and effects the modulation efficiency of the interferometer, which was set to one. In keeping with our design goal of a compact lightweight instrument, the aperture diameter was set to 15 cm. The stare time is also dependent on the size of the array. Two different array sizes were considered in this section: 6 x 6 and 16 x 16. A more complete analysis of aperture diameter and array size was carried out in Section 4.6.

The total photon flux that impinges on the detectors is an important parameter to consider when modeling performance. The total flux is the sum of all photons emitted from both the earthscene and warm optical components of the instrument. The optical properties of the various components in the design were input into the model to determine the total flux. The analysis assumed 35% transmission through the interferometer. Table 4-4, Table 4-5, and Table 4-6 show the components and the optical properties of each, for the LW, MW, and SW channel. The minimum and maximum wavenumbers define the spectral band each component passes. The half-angle refers to the half-angle of the light cone through each component, which is related to the  $f$ -number by

$$\theta = \tan^{-1} \left( \frac{1}{2 \cdot f\#} \right). \quad (4-6)$$

In all three ABS wavebands,  $\theta$  is equal to 17.9°.

<sup>12</sup> Bicknell W.E., Kerekes J.P., and Ryan-Howard D.P. "GOES Advanced Sounder Design Study", *Proc. SPIE*. Vol. 2812.



**TABLE 4-4****Background Inputs for the LW Channel**

Component	Temp (K)	Emissivity	Transmittance	Min Wavenumber (cm <sup>-1</sup> )	Max Wavenumber (cm <sup>-1</sup> )
Filter	220	0.03	0.9	662	5000
Lens 1	220	0.005	0.92	662	1150
Lens 2	220	0.005	0.92	662	1150
Cold mirror 3	220	0.02	0.98	662	1150
LW Dichroic	220	0.1	0.88	662	1150
Cold mirror 2	220	0.02	0.98	662	1150
Cold mirror 1	220	0.02	0.98	662	1150
Window	220	0.01	0.97	662	1150
Interferometer	220	0.1	0.35	662	1150
Vis Dichroic	295	0.1	0.88	662	1150
Tel. Mirror 1	295	0.02	0.98	662	1150
Tel. Mirror 2	295	0.02	0.98	662	1150
Tel. Mirror 3	295	0.02	0.98	662	1150
Scan Mirror	295	0.02	0.98	662	1150

**TABLE 4-5****Background Inputs for the MW Channel**

Component	Temp (K)	Emissivity	Transmittance	Min Wavenumber (cm <sup>-1</sup> )	Max Wavenumber (cm <sup>-1</sup> )
Filter	220	0.03	0.9	1250	5000
Lens	220	0.005	0.92	1250	1570
Lens	220	0.005	0.92	1250	1570
Cold mirror 4	220	0.02	0.98	1250	1570
MW Dichroic	220	0.1	0.88	1250	1570
LW Dichroic	220	0.1	0.88	1250	1570
Cold mirror 2	220	0.02	0.98	1250	1570
Cold mirror 1	220	0.02	0.98	1250	1570
Interferometer	220	0.1	0.35	1250	1570
Vis Dichroic	295	0.1	0.88	1250	1570
Tel. Mirror 1	295	0.02	0.98	1250	1570
Tel. Mirror 2	295	0.02	0.98	1250	1570
Tel. Mirror 3	295	0.02	0.98	1250	1570
Scan Mirror	295	0.02	0.98	1250	1570

**TABLE 4-6****Background Inputs for the SW Channel**

Component	Temp (K)	Emissivity	Transmittance	Min Wavenumber (cm <sup>-1</sup> )	Max Wavenumber (cm <sup>-1</sup> )
Filter	220	0.03	0.9	2150	5000
Lens	220	0.005	0.92	2150	2720
Cold mirror 6	220	0.02	0.98	2150	2720
Lens	220	0.005	0.92	2150	2720
Cold mirror 5	220	0.02	0.98	2150	2720
MW Dichroic	220	0.1	0.88	2150	2720
LW Dichroic	220	0.1	0.88	2150	2720
Cold mirror 2	220	0.02	0.98	2150	2720
Cold mirror 1	220	0.02	0.98	2150	2720
Interferometer	220	0.1	0.35	2150	2720
Vis Dichroic	295	0.1	0.88	2150	2720
Tel. Mirror 1	295	0.02	0.98	2150	2720
Tel. Mirror 2	295	0.02	0.98	2150	2720
Tel. Mirror 3	295	0.02	0.98	2150	2720
Scan Mirror	295	0.02	0.98	2150	2720

**4.4.2 Detector Modeling Input Parameters**

The detector array size, type (PV vs. PC), and operating temperature were allowed to vary in the initial trade study. The constraints on array size depend on detector type. The study focused on the LW channel, which is the most technically challenging from a detector standpoint. The MW and SW band baseline design calls for PV HgCdTe detectors that are routinely used in IR systems applications. In either the PV or PC case, the point-design detector active-area dimensions were 60  $\mu\text{m}$  square. Table 4-7 lists the predicted photon flux, along with other detector parameters for each band.

**TABLE 4-7****Detector Model Input and Output Parameters**

	LW	MW	SW
Photon Flux (ph/cm <sup>2</sup> /sec)	1.8E+16	1.6E+15	3.8E+13
Cutoff Wavelength ( $\mu\text{m}$ )	15.1	8	4.7
Temperature (K)	Trade (Sections 4.4, 4.6 and 4.7)		
Pixel Size ( $\mu\text{m}$ )	60	60	60
Quantum Efficiency	Trade (4.4, 4.5)	0.8	0.75
Responsivity (A/Watt)	Trade (4.4, 4.5)	4.5	2.6
R <sub>o</sub> A ( $\Omega\text{-cm}^2$ )	Trade (4.4, 4.5)	2.6E+05	4.3E+12
D* (cm Hz <sup>1/2</sup> /W)	Trade (4.4, 4.5)	5.8E+11	2.1E+12

*Trade* indicates a parameter that is to be determined in the course of the detector selection trade study. Relevant sections are in ( ).

#### 4.4.3 Detector Selection

The type of detector chosen for the LW channel greatly affects the volume, weight, performance, and cost of the sensor. Recent technical advances in HgCdTe PV technology have extended the obtainable cutoff wavelength at  $\sim 80$  K past  $15\text{ }\mu\text{m}$ , with sufficient performance for atmospheric remote sensing. The advantages of PV detectors, described below, make them the preferred alternative to PC detectors in new instruments. The primary advantage of PV detectors is their ability to be fabricated as large two-dimensional arrays employing multiplexed readouts to minimize the number of electrical leads. PC detectors require discrete pre-amplifiers (an individual amplifier for each detector) which limits them to small arrays.<sup>13,14</sup> A low detector resistance does not allow them to be multiplexed to silicon MOSFET pre-amplifiers. Large discrete PC arrays are impractical because of their large bias-power dissipation. PV detectors are routinely made in arrays  $128 \times 128$  and larger. Pre-amplifiers can be fabricated in silicon in a readout integrated circuit (ROIC). A reversed biased LW PV array can be cold-soldered to the ROIC using indium bump-bonding technology or connected via a fan out board.<sup>15</sup> A design using large format two-dimensional LW PV arrays is aggressive but realistic given the recent improvements in device technology. AIRS, a grating spectrometer sounding instrument scheduled for flight on the EOS-AM platform, utilizes PV HgCdTe linear arrays for detection up to  $13.75\text{ }\mu\text{m}$ , the longest cutoff wavelength is  $15.6\text{ }\mu\text{m}$ , achieved in a PC array operating at  $58\text{ K}$ .<sup>16</sup> This section examines the theoretical performance of both PC and PV detectors using a 1-D diffusion-limited Auger lifetime model, and discusses the implications for the ABS point design.

Figure 4-14 shows  $D^*_{BLIP}$  along with the thermal-noise limited  $D^*$  at detector temperature  $T = 65, 75,$  and  $85\text{ K}$  for PC HgCdTe. Also shown is the ultimate (BLIP) detection limit of a PV detector with a quantum efficiency of 1.

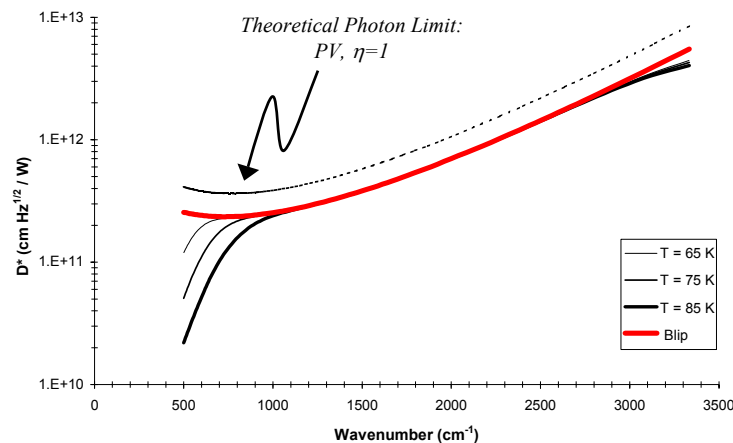


Figure 4-14. Theoretical limit to BLIP  $D^*$  and thermal-noise limited  $D^*$  for PC MCT detectors,  $T = 65, 75, 85\text{ K}$ .

<sup>13</sup> Crowe, D.G., *et.al.*, "Detectors", in *The Infrared & Electro-optical Systems Handbook*, vol. 3, Rogatto, W.D. ED., SPIE optical Engineering Press, 1993.

<sup>14</sup> Reine, M.B., *et.al.*, "Advances in  $15\text{ }\mu\text{m}$  HgCdTe Photovoltaic and Photoconductive Detector Technology for Remote Sensing" in *Proc. SPIE*, vol. 2816, 1996.

<sup>15</sup> Vampola, J.L. "Readout Electronics for Infrared Sensors", in *The Infrared & Electro-optical Systems Handbook*, vol. 3, Rogatto, W.D. ED., SPIE optical Engineering Press, 1993.

<sup>16</sup> Rutter, J.G., *et.al.* "Performance of PV/PC HgCdTe Focal Plane/Dewar Assembly for the Atmospheric Infrared Sounder Instrument (AIRS)." *Proc. SPIE*, vol. 3437, 1998.

The plot is for a 60  $\mu\text{m}$  square,  $n$ -type, 10  $\mu\text{m}$  thick HgCdTe detector. The donor concentration and bias current were held constant at  $3 \times 10^{14}$  and 2 mA respectively. The equivalent blackbody scene temperature was 270 K. The effects of minority carrier sweepout, which results in a non-uniform spatial response for PC detectors, were ignored. Thermal G-R noise dominates the LW portion of the spectrum, while Johnson noise dominates the SW portion of the spectrum because of the larger device resistances in this band.

Figure 4-15 shows the BLIP  $D^*$  along with thermal-noise limited  $D^*$  at detector temperatures  $T = 65, 75$ , and 85 K for unbiased PV HgCdTe.

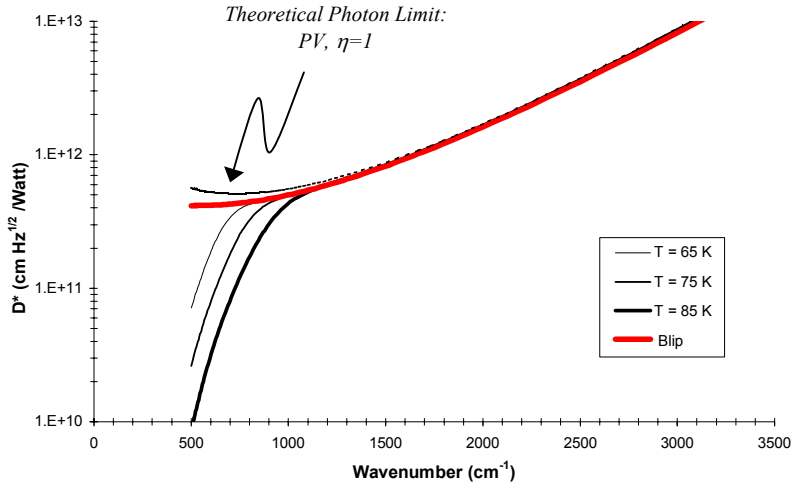


Figure 4-15. Theoretical limit to BLIP  $D^*$  and thermal-noise limited  $D^*$  for unbiased PV HgCdTe detectors,  $T = 65, 75, 85$  K.

The plot is for a 60  $\mu\text{m}$  square,  $p$  on  $n$ , backside-illuminated HgCdTe photodiode. The  $n$ -side donor concentration and absorber layer thickness were held constant at  $1 \times 10^{15}$  and 10  $\mu\text{m}$  respectively. The scene equivalent blackbody temperature was 270 K. Note that in Figures 4-13 and 4-14, the plots correspond to a detectors with the  $\text{Hg}_{1-x}\text{Cd}_x\text{Te}$  Cadmium concentration tuned to produce a detector peaked at each wavenumber; that is, the plots do not correspond to a physically-realizable detector but rather to the performance limit attainable by an optimized set of detectors.

To compare the theoretical performance of PC vs. PV devices the detector limited noise equivalent radiance ( $\text{NEdN}_{\text{det}}$ ) is calculated from

$$\text{NEdN}_{\text{det}} = \frac{c}{\sqrt{t_{\text{stare}}} D_{\lambda}^*}, \quad (4-7)$$

where  $c$  is a constant derived from instrument parameters and  $t_{\text{stare}}$  is the stare time to take one complete interferogram.  $D^*$  depends on the detector type and temperature, while  $t_{\text{stare}}$  depends on the array size. Figure 4-16 shows the theoretical  $\text{NEdN}$  performance of a single array element for both PC and PV detectors as a function of wavenumber. A 6 x 6 PC array is shown along with both a 6 x 6 and 16 x 16 PV array. A 15 cm aperture was assumed to calculate the photon flux at the detectors. The detector temperature was held at 65 K for the comparison. Detector parameters are as described above.

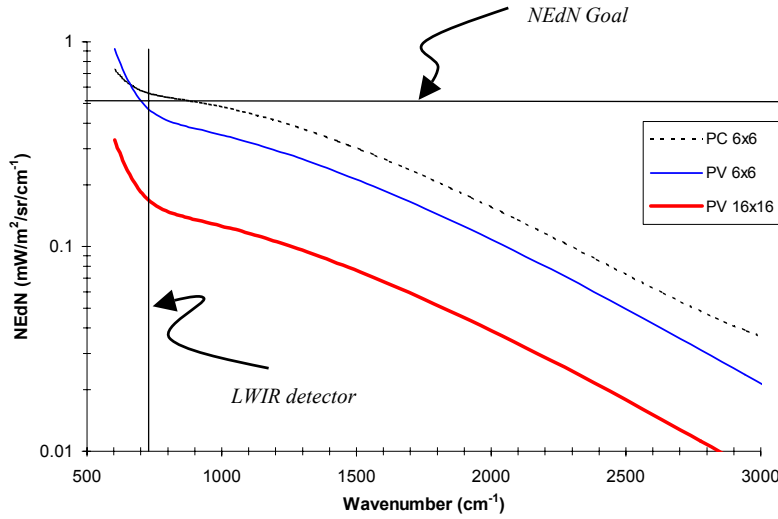


Figure 4-16. Theoretical limit to performance of 6x6 PC and PV arrays compared to a 16 x 16 PV array (all at  $T = 65$  K) as a function of wavenumber.

The plot shows there is a substantial advantage to using a relatively large PV array. The advantage arises from the longer stare time possible when using a large array in a step-and-stare imaging mode. Each detector resolves a 10 km diameter spot on the ground. The ground coverage for this trade study was 3000 x 5000 km in 30 minutes. The time to take an interferogram,  $t_{stare}$ , is 0.4 sec using a 6x6 array and 3.1 sec for a 16x16 array. Only PV arrays can achieve a large array format because of the limitations discussed earlier applying to PC detector arrays.

Figure 4-17 shows the detector-limited NEdN of the instrument using a 16 x 16 PV array as a function of detector temperature, to study the temperature sensitivity of the NEdN in each band. The line is flat when photon noise dominates and exhibits a slope versus temperature, as thermal noise becomes dominant.

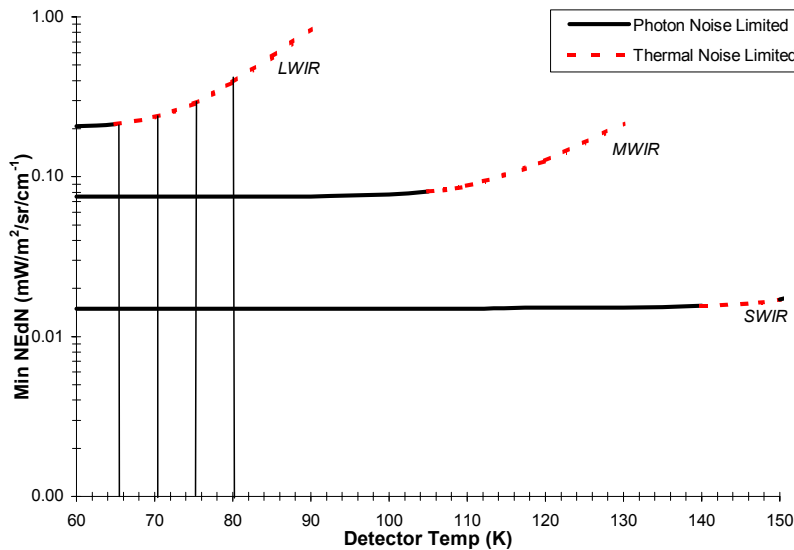


Figure 4-17. LW minimum NEdN in each band as a function of detector temperature.

The plot assumes a 15 cm aperture. Detection is BLIP limited for temperatures below 65 K in the LW band,  $\sim 100$  K in the MW band, and  $\sim 140$  K in the SW band. Although operating the LW detector at 65 K or lower is desirable, this imposes severe constraints on the focal plane cooling, and drives the choice of an active versus passive cooling method. The detector-limited performance in the LW channel at temperatures up to 80 K is less than  $0.5 \text{ mW/m}^2/\text{sr/cm}^{-1}$ . Atmospheric temperature profile retrieval error modeling, presented in Section 4.5, shows that this is acceptable for sounding. The final selection of detector temperature however depends on issues involved with reading out PV arrays. The implications of using relatively large arrays in the LW channel of the Advanced Baseline Sounder are further explored in Section 4.6.

## 4.5 LW-BAND DETECTOR CUTOFF-WAVELENGTH SELECTION

*Key points:*

- *Need to cover at least the  $667 \text{ cm}^{-1}$  to  $710 \text{ cm}^{-1}$  side of the longwave-IR  $\text{CO}_2$  feature*
- *At 75 K, a peak wavelength of  $13.7 \text{ }\mu\text{m}$  is sufficient to provide to provide this coverage*
- *Temperature and humidity retrieval simulations validate this conclusion*

One method of evaluating the performance of infrared detectors is to consider their performance at the device level, e.g. their detectivity ( $D^*$ ). A second method is to incorporate system-level effects that leads to figures of merit such as NEdT and NEdN which are determined both by the detector performance and system characteristics. A third method of assessing detector performance, preferable for specifying the ABS longwave-band detector cutoff, is to evaluate the detector impact on the accuracy of retrieved temperature and humidity values from soundings. Using the detector noise properties, the quality of temperature and humidity results can be simulated via the retrieval calculations. The resulting RMS error profiles for both temperature and humidity can then be compared with the values specified in the 1996 NWS Observational Requirements draft<sup>1</sup>. In this way, it is possible to define what detector noise performance, and particularly what wavelength coverage, are sufficient to meet those requirements. Note that throughout this section, the peak wavelength of the detectors will be specified rather than the cutoff wavelength. The cutoff wavelength (defined as  $1.1 \lambda_{\text{peak}}$ ) is more typically used to specify detectors, however the peak wavelength gives a more intuitive view of the matching of detector spectral characteristics to atmospheric spectral features.

### 4.5.1 Previous Study Results For PC Detectors

An MIT Lincoln Laboratory simulation of retrieved sounder results that modeled PC detector noise was conducted in 1995. In this previous work, the peaks of the weighting functions were plotted as shown in Figure 4-18. To obtain temperature profile information in the 10 – 500 mb region, good coverage of the spectral range between  $667 \text{ cm}^{-1}$  and  $710 \text{ cm}^{-1}$  is required. This coverage does not necessarily require a MCT detector that cuts off  $16 \text{ }\mu\text{m}$  or beyond. In fact as we will demonstrate for the ABS design, the required spectral coverage is provided by a PV MCT detector with a peak response in the range  $13.7 \text{ }\mu\text{m} \leq \lambda_{\text{peak}} \leq 14.0 \text{ }\mu\text{m}$ , or equivalently a cutoff wavelength (defined as  $1.1 \lambda_{\text{peak}}$ ) in the range  $15.1 \text{ }\mu\text{m} \leq \lambda_{\text{cutoff}} \leq 15.4 \text{ }\mu\text{m}$ .

In the previous study, the GHIS instrumental noise for the PC detector was calculated in the form of the noise-equivalent temperature error (NEdT). The NEdT values were then used in calculations of the RMS retrieval temperature error profile. The results showed that a factor of two increase in NEdT in the longwave band only resulted in about a 20% increase in RMS temperature error. The sensitivity of the sounding retrieval to NEdT variation is therefore lower than might be expected. This low sensitivity to NEdT values is valid for both PC and PV detector types.

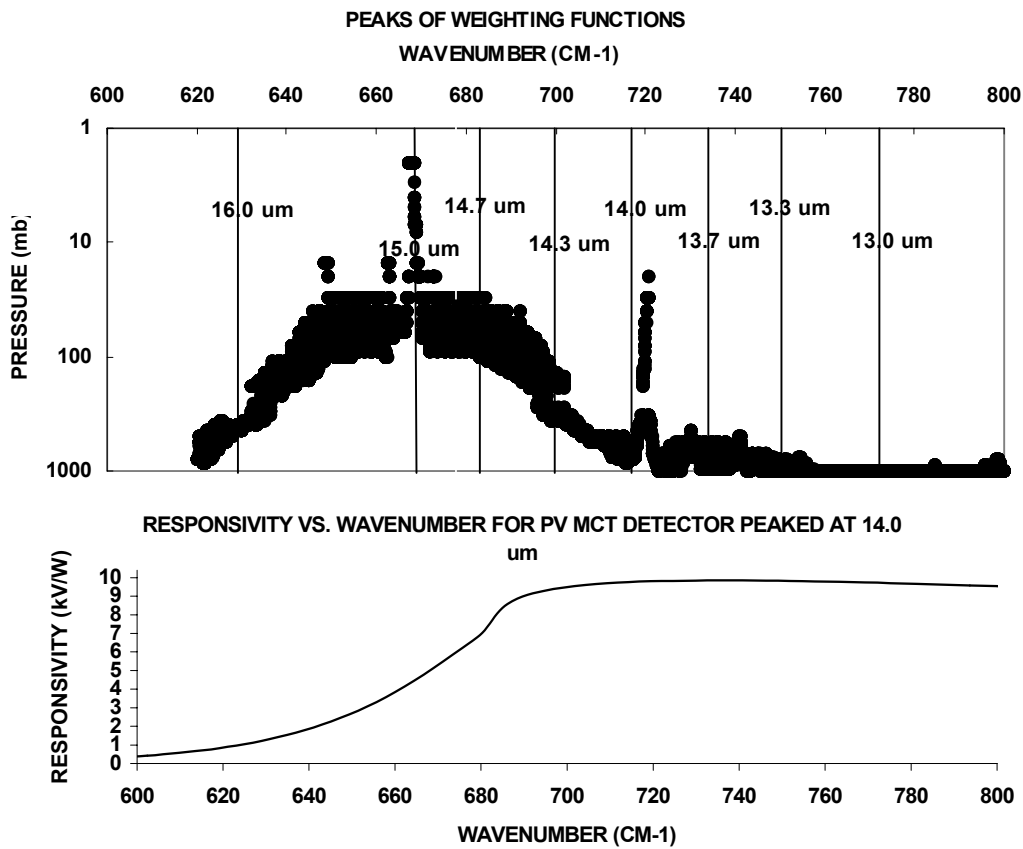


Figure 4-18. The peak pressure of a large number of weighting functions is plotted vs. wavelength. Temperature information in the 10 – 500 mb region requires coverage of at least one side of the CO<sub>2</sub> feature, nominally between 667 cm<sup>-1</sup> and 710 cm<sup>-1</sup>. Plotted at the bottom of the figure is the responsivity of a detector for which  $\lambda_{peak}=13.7 \mu\text{m}$ , illustrating the spectral coverage there.

Another result of the previous study was that increasing the PC detector cutoff wavelength yielded smaller RMS temperature errors. This was attributed to the increasing coverage on the far side of the CO<sub>2</sub> absorption feature, where the signal begins to increase with wavelength beyond about 15 μm. The PV detector did not show this same dependence, as detailed below. The increase in rms temperature error with peak wavelength for the PV detectors is due to the increase in NEdT, which in turn is due to the thermal noise associated with the strong temperature sensitivity of the PV detector R<sub>0</sub>A.

#### 4.5.2 ABS Study Of Longwave PV Detector Cutoff

**Method.** For ABS, we conducted a similar study of PV detector noise and retrieval sensitivity. The radiometric performance model, described in Appendix C, was used to calculate the noise performance properties of a PV detector. The resulting NEdT values were then used as the instrumental noise in simulating the RMS temperature error and the RMS humidity error in the retrieved profiles.

The retrievals were performed by a solution of the radiative transfer equation through an iterative technique. The RMS temperature error versus pressure was computed using profiles from the TOVS Initial Guess Retrieval (TIGR) data set, a version of which has been used for algorithm development by

the NASA/EOS AIRS science team. A subset of that data set was used for testing, composed of 147 profiles with clear sky conditions and “moderate” temperature retrieval difficulty; a different subset of the “moderate” set was used for training purposes. 182 channels were used for retrieval, covering wavenumbers between 610 and 2700  $\text{cm}^{-1}$ . The retrieval was performed using longwave channels that extend to 610  $\text{cm}^{-1}$ . This channel set was chosen for a previous study, and was not optimized for this study. Although this wavenumber is beyond the cutoff of the 16- $\mu\text{m}$  detector, this corresponds to the 50% responsivity point of the detector, thus some wavelength coverage exists at longer wavelengths. When responsivity of the detector becomes very low and the retrieved information becomes noisy, the retrieval process reduces the weighting of the noisiest channels.

In order to study the dependence of the cutoff wavelength on the retrieval results, the Cd concentration was tuned with a fixed temperature to produce NEdT values for peak responsivities at  $\lambda_{\text{peak}} = 13.0, 13.3, 13.7, 14.0, 14.3, 14.7, 15.0, 16.0 \mu\text{m}$ . Each of these data points represents a separate case, and in each case the noise performance was recalculated and the covariance matrix was recomputed. Recall that the peak responsivity occurs at a wavelength that is 10 percent below the defined cutoff wavelength.

**RMS Temperature Error Profiles.** The retrieved RMS temperature error results for a 75 K detector temperature at a series of different HgCdTe detector peak wavelengths are shown in Figure 4-19. The plot shows little difference between peak detection near 13.7  $\mu\text{m}$  – 14.7  $\mu\text{m}$ , all of which remain below 1.0 K error until above 10 mb. The peak detector wavelengths above 14.7  $\mu\text{m}$  begin to show poorer performance. Ultimately, the NEdT values increased with peak wavelength due to the decrease of the energy band gap, permitting collection of more thermally excited electrons. The profiles are not plotted above about 3 mb in order to assure that the layer average in the last bin was calculated with the same number of retrieved level data points in all profiles.

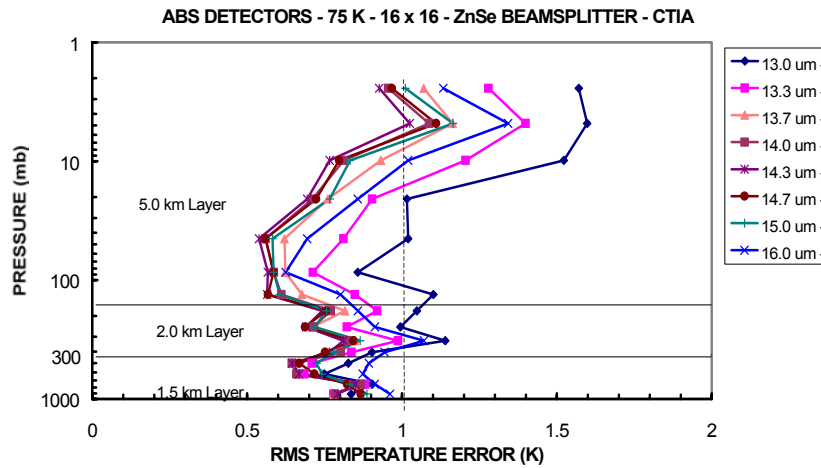


Figure 4-19. The simulated RMS temperature error is plotted vs. pressure for a 16 x 16 array operated at 75 K for peak wavelengths of 13.0, 13.3, 13.7, 14.0, 14.3, 14.7, 15.0, and 16.0  $\mu\text{m}$ . The smallest error is obtained from 14.3  $\mu\text{m}$ , although 13.7 – 14.7  $\mu\text{m}$  are “in-family”.

The thickness of the layers shown here are 1.5 km in the 1000 – 300 mb region, 2 km in the 300 – 100 mb region, and 5 km in the 100 – 10 mb and above region. Layer averaging of level results was



performed using values within the NWS specifications for a geosynchronous sounder: 1-2 km, 2-3 km, and 4-6 km respectively for the 1000 – 300 mb, 300 – 100 mb, and 100 – 10 mb regions.

Near 1000 mb, the sensitivity to the altitude resolution is high. The increase of the error at altitudes below about 800 mb has been taken as a metric of retrieval accuracy. The retrieval errors at the surface were decorrelated from the lowest atmospheric layer in order to make the retrieval errors more realistic near the surface. Because the error values just above the surface were decorrelated from the surface values, the RMS error values increase near the surface with 1-km binning. With 2-km resolution, the increase in error near the surface is averaged away. With 1.5-km binning, any wavelength dependence in the response near the surface remains within the error bars. However, it is important to note that as the resolution is improved to 0.5 km, the results show a noticeable increase in RMS temperature error near the surface.

The closer the binning comes to the upper limit for each region, the smaller the RMS errors become. However, a large discontinuity in the altitude resolution across the border (1 km at 300 mb and 3 km at 10 mb) can produce significant spikes in the rms error profile if the transitions are not handled smoothly. Smith<sup>2</sup> shows a smooth curve for the changing altitude resolution, thus a smooth transition between regions is not unprecedented.

Nine cloud-free pixels (out of twenty-five per sounding cell) is the minimum number used in a retrieval with current GOES sounder data. Therefore the signal and noise associated with nine pixels (9 times the per-pixel signal and square root 9 times the per-pixel noise) were used in the ABS simulation. The use of more cloud-free pixels would reduce the noise.

In any real array of detector elements, the signal and noise of each element has some spread about an average value. To correct for this, the response of each pixel is characterized by some zero-offset and gain, which are characterized by a two-point correction using a blackbody view and space view as scene-temperature standards. We now address whether this pixel to pixel variation, which we have not yet included in our modeling, will limit the retrieval results. The difference in pixel response after this correction (“corrected non-uniformity”) is typically about 0.3%. This would correspond to about a 0.4% increase in NEdT. Because a doubling in NEdT yields a 20% increase in the retrieval values, an increase of 0.4% in NEdT would be expected to increase the RMS temperature error by 0.04%. For a signal to noise value of about 300, the variation would be 0.3%. Thus, the pixel-to-pixel variation immediately after a good two-point correction should have no noticeable effect on the retrieval values computed after assuming the 9 pixels responded with the same signal and noise. The retrieval results thus assume a recent correction for non-uniformity. The stability of the two-point correction over short-term and long-term time scales requires further investigation as the offset of each pixel can drift with temperature and time. Assume that a 2% increase in RMS temperature error over the whole coverage area in about 1 hour is a rough requirement; this would imply that offset drifts increase NEdT by less than 20% and thus non-uniformity values that differ by less than 16% over the hour are required. This in turn implies bias drift of less than about 7% and temperature drift of less than 5 K during that time, both of which should be achievable.

***RMS Temperature Error Versus Cutoff Wavelength at Fixed Temperature.*** The same retrieval simulation performed for a detector temperature of 75 K was repeated for 65 K, 70 K, 80 K, and 85 K temperatures. A fixed peak wavelength was assumed and the Cd concentration was tuned for peak responsivity at that wavelength for the desired temperature. The next three graphs (Figures 4-20, 21, and 4-22) show the mean RMS temperature error in each of the three pressure zones (1000 – 300 mb, 300 – 100 mb, and 100 – 3 mb). The RMS temperature errors in these figures are plotted as a function of wavelength for the five FPA operating temperatures listed above.

For the shortest wavelengths, the rms temperature error is altitude dependent. In the 1000 – 300 mb region, the rms error from about 13 to 14.7  $\mu\text{m}$  decreases slightly with increasing wavelength. In the 300-100 mb and the 100-3 mb pressure zones, the rms error is largest near 13  $\mu\text{m}$  because little temperature information above  $\sim 700$  mb is contained near 13  $\mu\text{m}$ .

For the longest wavelengths, the rms error is temperature dependent. For the lower temperatures (65 K and 70 K) in all three pressure regimes, the extension to the longest wavelengths does not provide significantly reduced noise performance for the PV detectors. From 1000-300 mb, there is a slight error reduction ( $\sim 0.1$  K) but from 100 mb – 1 mb, there is a slight increase in RMS error near 15 – 16  $\mu\text{m}$ . However, with increasing operating temperatures (75 K – 85 K), there is actually a disadvantage associated with requiring peak performance past about 14.3  $\mu\text{m}$ . For a FPA operating temperature of 85 K and warmer, there is a sharp increase in rms error near 15-16  $\mu\text{m}$ . The increased noise there is due to increasing thermal noise in the FPA, which is ultimately tied to the use of commercial PV detectors which utilize MOSFET readouts.

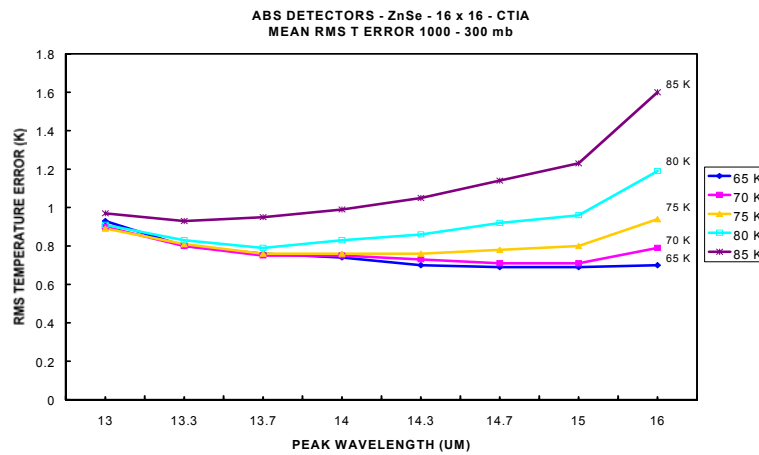


Figure 4-20. Mean RMS temperature error as a function of wavelength in the 1000 - 300 mb zone for detectors tuned to various peak wavelengths (listed in Figure 4-19), with detector temperatures of 65 K, 70 K, 75 K, 80 K, and 85 K.

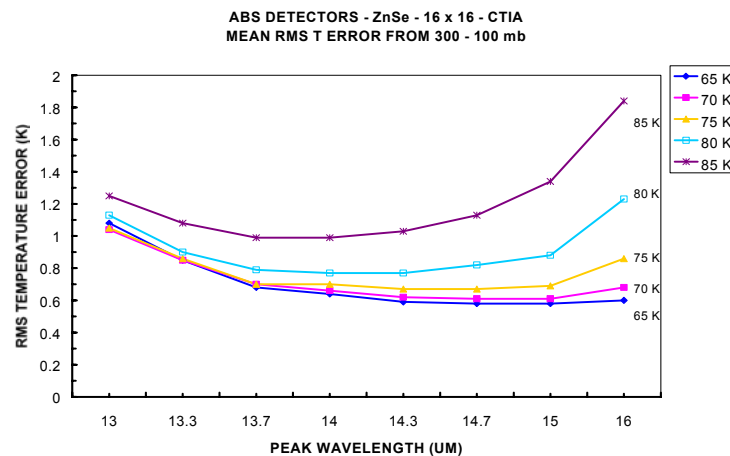


Figure 4-21. Mean RMS temperature error as a function of wavelength in the 300 - 100 mb zone for detectors tuned to various peak wavelengths (listed in Figure 4-19), with detector temperatures of 65 K, 70 K, 75 K, 80 K, and 85 K.

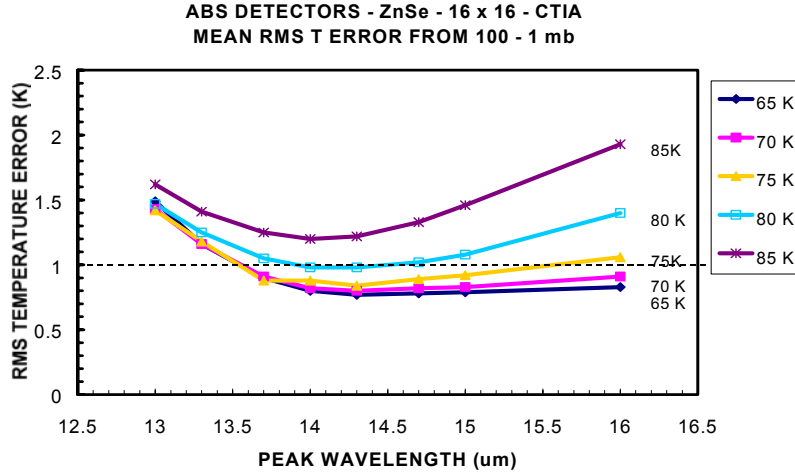


Figure 4-22 Mean RMS temperature error as a function of wavelength in the 100 - 5 mb zone for detectors tuned to various peak wavelengths (listed in Figure 4-18), with detector temperatures of 65 K, 70 K, 75 K, 80 K, and 85 K.

Ultimately, the results also show that a detector with  $\lambda_{\text{peak}} = 14.0 \mu\text{m}$  operating at 75 K meets NWS requirements of 1 K error from 1000 mb up to over 10 mb. Although operation at 80 K may appear to be possible from these graphs, operation at 75 K provides adequate margin in meeting the NWS specifications, especially in the 100 – 1 mb region.

The current retrieval simulation shows the minimum RMS temperature error occurs at peak wavelengths between 14.0 and 14.3  $\mu\text{m}$ . In light of the challenges associated with obtaining good HgCdTe detector yield at long cutoff wavelengths while still maintaining reasonable cost, the shortest detector cutoff that provides the required performance should be chosen. Because there is little change in retrieval performance between a detector operating with a peak of 13.7  $\mu\text{m}$  and a peak of 14.0 – 14.3  $\mu\text{m}$ , it would appear reasonable to decrease the peak value to no shorter than 13.7  $\mu\text{m}$ , implying a cutoff wavelength no shorter than 15.07  $\mu\text{m}$ . For shorter wavelengths, the RMS error is no longer in-family with the 14.0- $\mu\text{m}$  performance. The detector performance simulation does not include tunneling, but the inclusion of this effect in the model should increase noise only at very long wavelengths. It should not significantly change the results near 14  $\mu\text{m}$ .

**Comparison with vendor data.** In order to validate the temperature dependence on the long-wavelength detectors, published  $R_0A$  data from Lockheed Martin Infrared Imaging Systems (LMIRIS), and the relevant operating temperature data, were used. From this the required doping concentrations for the LMIRIS detectors were calculated, followed by NEdT values and RMS temperature errors. The results are shown in Figure 4-23. Our simulations show good agreement with the published LMIRIS detector data. It is important to note that a real detector experiences a change in performance with temperature that does not form a vertical line on this type of graph, but rather a slanted line. The cutoff temperature of a detector decreases with wavelength roughly according to  $\Delta\lambda_{\text{peak}} / \Delta T \approx 0.5 \mu\text{m} / 10 \text{ K}$ .<sup>14</sup> The temperature dependence of the simulated RMS temperature error results for the LMIRIS detectors shows a slightly stronger temperature dependence than our simulated results and therefore about 20% more noise than we simulated at 13  $\mu\text{m}$ , but overall the agreement is good.

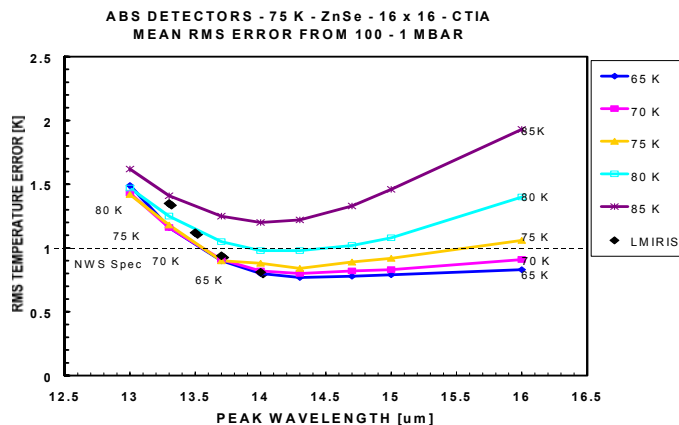


Figure 4-23. Mean RMS temperature error as a function of wavelength in the 100 - 5 mb zone for detectors tuned to various peak wavelengths (listed in previous Figure 4-18), with detector temperatures of 65 K, 70 K, 75 K, 80 K, and 85 K. Values from current detector technology are shown based on published  $R_0A$  and temperature data from LMIRIS.<sup>17</sup>

Using this scaling relationship, we can establish with some confidence whether the detector technology required for the cutoff wavelength implied by our simulation exists. LMIRIS and Boeing have demonstrated the longest cutoff-wavelength PV detector capability. Boeing has published results from a detector with a 14- $\mu\text{m}$  cutoff operating at 100 K<sup>18</sup>, which implies a cutoff near 15.4  $\mu\text{m}$  at 75 K by the above scaling and a peak of 14.0  $\mu\text{m}$ . LMIRIS has published information on a detector with a cutoff of 15.0  $\mu\text{m}$  at 70 K, which can be operated at 75 K for a peak wavelength of 13.2  $\mu\text{m}$  at 75 K and a cutoff wavelength of 14.5  $\mu\text{m}$ . Peak wavelengths of 13.2  $\mu\text{m}$  to 14.0  $\mu\text{m}$  at 75 K, corresponding to cutoff wavelengths of 14.5  $\mu\text{m}$  to 15.4  $\mu\text{m}$ , now exist at the cutting edge of current technology. Note that these cutoffs have been achieved with pixel sizes that are about twice that required for ABS. Whether the properties of detectors with pixels sized appropriately for ABS would prove sufficient for the needs of the instrument requires further investigation.

**RMS Relative Humidity Error Results** RMS Relative humidity errors were also calculated. They are shown in Figure 4-24. The NWS draft specifies a 10 % error between 1000 mb and 300 mb and 20 % error between 300 mb and 100 mb. We do not retrieve relative humidity numbers above 130 mb due to concerns about the reliability of the relative humidity retrieval in a region of the atmosphere with very low water vapor concentration. The retrieval results show about a 13 % error in the lower zone and a 9 % error in the higher zone, although we are only examining the 130-300 mb region there. The increase in relative humidity error near the surface is to be expected while RMS error values above about 230 mb are regarded as low<sup>19</sup>. An estimated relative humidity error profile for the current GOES sounder and s

<sup>17</sup> Reine, M. B., E. E. Krueger, P. O'Dette, and C. L. Terzis, "Photovoltaic HgCdTe detectors for advanced GOES instruments," *GOES-8 and Beyond*, Edward R. Washwell, ed., Proceedings of the SPIE, vol. 2812, p. 12-137, 1996.

<sup>18</sup> D'Souza, A. I., L. C. Dawson, E. J. Anderson, A. D. Markum, W. E. Tennant, L.O. Bubulac, M. Zandian, J. G. Pasko, W. V. McLevige, D. D. Edwall, J. W. Derr, J. E. Jandik, VSWIR to VLWIR MBE Grown HgCdTe Material and Detectors for Remote Sensing Applications, *Journal of Electronic Materials*, vol. 26, No. 6, p. 656-661, 1997.

<sup>19</sup> J. Hawkins, private communication, 9/23/98.

retrieved profile from GHIS from Smith<sup>20</sup> also shows a sharp increase in the rms humidity error just below the cutoff of the plot at 250 mb. We are investigating the apparently better performance obtained from our retrieval in this atmospheric region. This investigation should include an optimization of the channel set, in particular the water vapor bands. We note however that the retrieval performance above 130 mb has the potential to change the rms error in the 300 - 100 mb region.

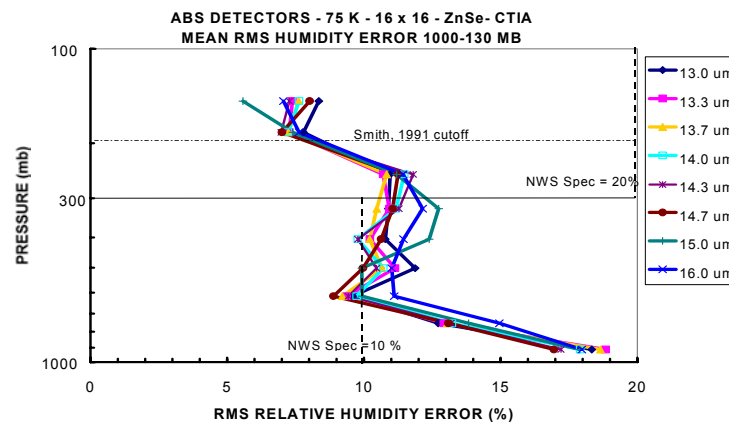


Figure 4-24. Results of retrieval showing mean RMS relative humidity error as a function of height. Smith, 1991 does not quote retrieval errors above 250 mb.

Unlike the RMS temperature results, these results are not particularly sensitive to the longwave detector peak wavelength, as shown in Figures 4-25 and 4-26. The lack of dependence is reasonable because the longwave channel primarily provides information on temperature profile. The water vapor information in the longwave band is only contained in the shortest wavelengths of the longwave band and is thus not affected by changes to the longwave side of the band. The relative humidity results are more sensitive to midwave (5.7 and 8.2  $\mu\text{m}$ ) detector performance because water vapor lines occur there. Decreasing the short-wave NEdT numbers for the PV HgCdTe detectors by about a factor of 2 reduces the relative humidity error from about 11% to about 10%.

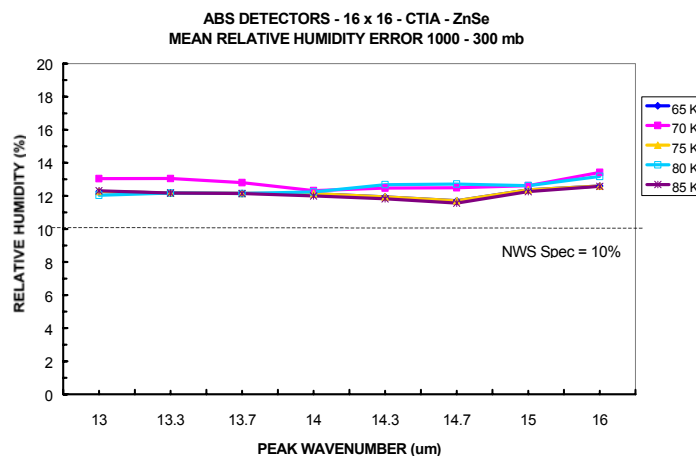


Figure 4-25. Mean RMS relative humidity error in the 1000 -300 mb region plotted versus wavenumber. The NWS specification is 10% in this atmospheric region.

<sup>20</sup> Smith, W. L. et. al., "GHIS - The GOES High Resolution Interferometer Sounder," *Journal of Applied Meteorology*, Vol. 29, pp. 1189-1204, Dec, 1990.

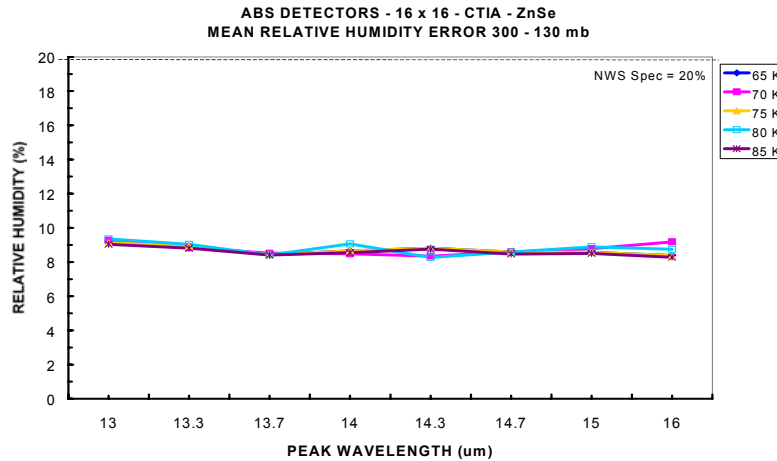


Figure 4-26. Mean RMS relative humidity error from 300 - 130 mb region plotted as a function of peak wavelength. The NWS specification is 20% in this region.

### 4.5.3 Conclusion

The results of our simulated detector and retrieval performance indicates that the optimal cutoff wavelength is no shorter than 15.07  $\mu\text{m}$ , with a peak performance of 13.7  $\mu\text{m}$  at a 75 K operating temperature. Under these conditions, the 1996 NWS draft requirements for the RMS temperature error are met in all three atmospheric regions. The relative humidity error results are met in the lowest altitude region with the current choice of retrieval channel set, but require further investigation above 300 mb. The relative humidity results are independent of this longwave-band detector cutoff.

## 4.6 IR DETECTOR READOUT OPTIONS

*Key points:*

- The increase in integration time afforded by large PV detector arrays is limited by readout IC integrating-capacitor charge storage, or “well-depth”.
- Impedance-matching of LW array to ROIC preamplifiers requires reverse-biasing of detector, increasing dark current.
- Faster readout implies multiple output multiplexers, and larger power dissipation.
- 16 x 16 array size is sufficient to meet NEdN goals in a small instrument, while requiring a single output.

This section presents the readout issues involved with using large “second generation” PV focal plane arrays (FPAs). These issues can greatly impact the overall system architecture including optical, mechanical, and thermal designs. A complex series of trades lead to the choice of array size, detector temperature, and aperture diameter. First, the ground coverage requirement and detector array size define the scan rate, stare time, mirror velocity and ideal sampling rate of the interferometer. Each detector can stare at one point on the ground for a longer time using a large array, and still meet the coverage specification. The S/N of the instrument increases with the square root of the stare time and the number of detectors in the array. Second, the impedance of the detector must be matched to that of the ROIC pre-amplifier to minimize amplifier noise. This requires reverse-biasing of the LW detector, which produces a temperature-dependent leakage current. Third, ROIC pre-amplifiers typically employ an integrate-and-

sample architecture, e.g. a discrete, rather than continuous, interferogram is produced from each detector. Each discrete sample is the detector current summed over a nominal integration time. The integration time is determined by the ideal sampling rate. Fourth, the ROIC integration capacitor has a limited charge-storage capability (or “well depth”) which must accommodate both the signal and leakage current during the integration time. Capacitor size limitations require readout rates faster than the ideal rate when using large arrays. Fifth, the maximum allowable integration time and detector noise (both of which depend on detector temperature) along with the collecting-aperture diameter must yield a NEdN satisfying the requirements. Finally, the readout rate from the ROIC determines the number of output taps that are required, which dominates the power dissipation of the FPA and thus the amount of cooling that is necessary.

The net effect is that the operating temperature of the detectors, aperture diameter, FPA power dissipation, array size, and sampling rate are intimately linked. This section addresses these issues in a step-by-step manner, beginning with ROIC amplifier characteristics, photodiode characteristics, and charge storage capacity. Trade studies determining the number of FPA outputs, aperture diameter, array size, and operating temperature are also presented.

#### 4.6.1 Detector and ROIC Pre-amplifier Types

The ROIC contains a low-noise pre-amplifier for each detector in the array, and includes multiplexers to minimize the number of outputs. Although they can be fabricated using Bipolar Junction (BJT), Junction Field Effect (JFET), or Metal Oxide Semiconductor Field Effect Transistors (MOSFET), ROIC pre-amplifiers are predominately fabricated using MOSFETs. Operation at low temperatures and high power dissipation has discouraged the use of JFETs and BJTs in the past. Two pre-amplifier designs that provide low noise, high gain, and dynamic ranges of 10,000, are the resistor trans-impedance amplifier (RTIA) and the capacitor trans-impedance amplifier (CTIA), shown in Figure 4-27 and Figure 4-28 respectively. Variations on these designs provide an additional source follower front-end and more complex feedback impedance to control frequency response<sup>15</sup>. The source follower device selection is optimized for the source impedance presented by the parallel combination of the detector and feedback resistors. Some form of filtering is required to limit the noise bandwidth prior to the output multiplexer when using the RTIA.

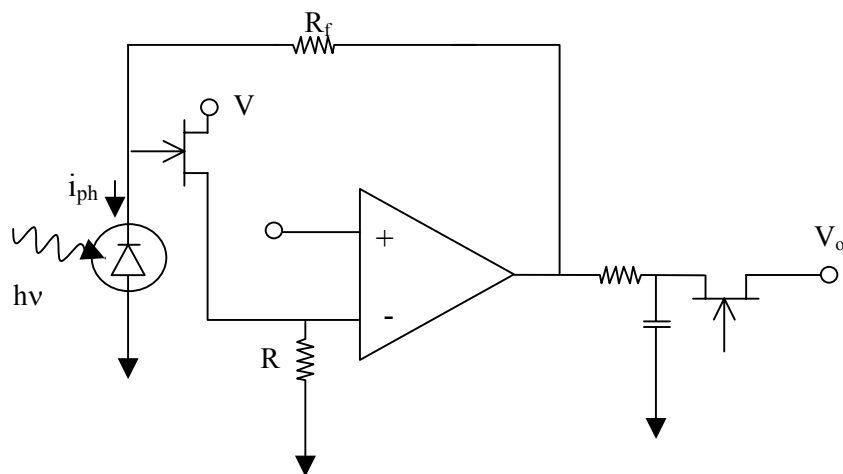


Figure 4-27. The RTIA with a source follower input and output filter.

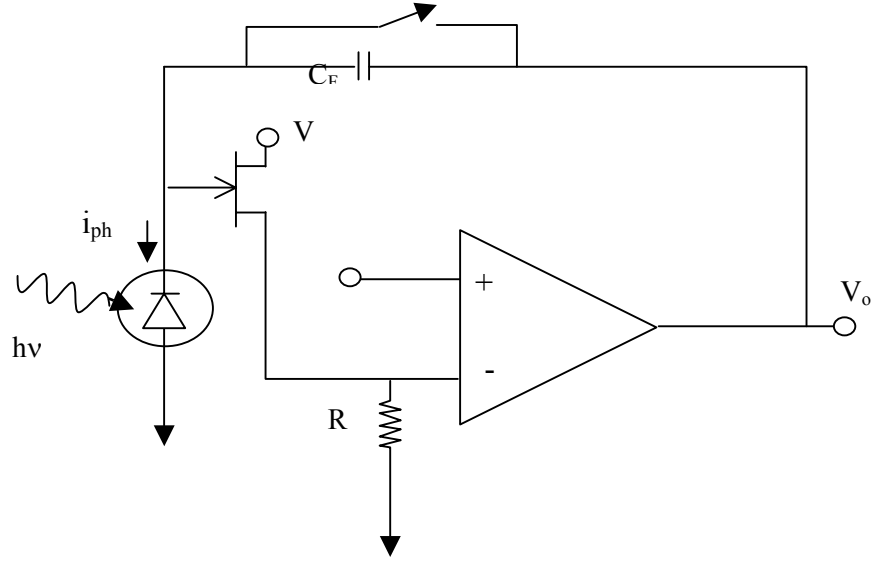


Figure 4-28. The CTIA with a source follower input.

In general, the large resistor values required for the RTIA are difficult to consistently fabricate given the small unit area for each pre-amplifier. The ROIC CTIA design is simpler and more commonly found in remote sensing instrumentation. The noise performance is expected to be similar for both options, dominated by the noise characteristics of the initial source-follower front-end. The ABS point design will use a CTIA MOSFET pre-amplifier.

#### 4.6.2 Pre-amplifier Current and Voltage Input Noise

Amplifier noise is generally referred to the input and modeled as an ideal voltage source in series with the inverting input and an ideal current source in parallel with each of the inputs. The manufacturer of a particular component generally specifies both the noise voltage density,  $e_n$  (nV/ $\sqrt{\text{Hz}}$ ), and current density,  $i_n$  (pA/ $\sqrt{\text{Hz}}$ ). Each term is frequency dependent. The input-referred total current noise is the root sum of the squares (RSS) of the amplifier noise current, the current caused by the amplifier noise voltage across external source resistors (including the parallel feedback and detector resistance), and Johnson thermal noise of the external source resistors. The total noise current referred to the first stage input is

$$i_e^2 = \frac{e_n^2}{R_{\parallel}^2} + i_n^2 + \frac{4kT}{R_{\parallel}} \quad (4-8)$$

where the source resistance  $R_{\parallel}$  is the parallel resistance of the detector and the feedback resistor for the RTIA, or the detector alone for the CTIA. The source impedance is an important parameter to consider when modeling the noise performance of the pre-amplifier. Given a choice, the designer must match a particular amplifier technology with the source resistance.<sup>21</sup> The voltage noise of the amplifier first stage dominates when the source (e.g. detector) impedance is low, while a high-impedance source causes the current noise of the amplifier to dominate. MOSFETs are characterized by low current noise but substantial  $1/f$  voltage noise. Output noise is minimized when used with high-impedance detectors. While this is ideal for the SW and MW detectors, the LW detector requires reverse-biasing to achieve this high impedance.

<sup>21</sup> Horowitz, P. and Hill, W. The Art of Electronics, Second Edition. Cambridge University Press, Cambridge, MA. 1989. pp. 428 – 455.



#### 4.6.3 Diode Resistance and Biasing

Low resistance is an intrinsic property of LWIR HgCdTe photodiodes operated at relatively high temperatures ( $T \sim 80$  K). Applying a reverse bias voltage across the diode junction however, can increase the resistance of the detector. The rate of change of the voltage with current at the bias point  $V$  defines the dynamic source resistance, which is presented by the diode to the first stage in the pre-amplifier. The resistance of real detectors rises to a maximum value and falls off due to excess leakage and the onset of breakdown. The dynamic resistance can be written as a function of the zero-bias resistance, assuming an ideal diode, as

$$R = R_0 e^{\frac{eV}{kT}}, \quad (4-9)$$

where  $e$  is the charge of an electron,  $k$  is Boltzmann's constant, and  $T$  is the diode temperature. The detector noise current density of the reverse-biased diode, from thermal and photon processes (described in more detail in Appendix C), is given by

$$i_{det} = \sqrt{2e^2 \phi_{abs} A + \frac{2kT}{R_0} \left( e^{\frac{eV}{kT}} + 1 \right)}, \quad (4-10)$$

where  $A$  is the detector area and  $\phi_{abs}$  is the photon flux absorbed by the detector. The total noise current from detector and amplifier noise is then

$$i_{Tot} = \sqrt{2e^2 \phi_{abs} A + \frac{2kT}{R_0} \left( e^{\frac{eV}{kT}} + 1 \right) + \frac{e_n}{R_0 e^{\frac{eV}{kT}}} + i_n}. \quad (4-11).$$

Figure 4-29 shows the ratio of amplifier noise current to detector noise current as a function of the detector bias, for detector temperatures between 65 and 80 K. Ideally, this ratio should be much less than 1, when detector noise dominates the system.

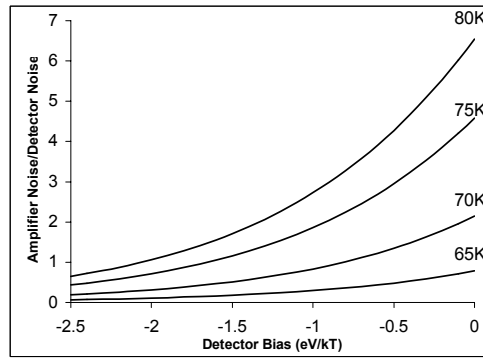


Figure 4-29. The ratio of amplifier noise current to detector noise current as a function of the detector bias, for detector temperatures between 65 and 80 K.

The plot shows that reverse-biasing is required in the LW channel to suppress amplifier noise to an acceptable level. Also, there is a significant advantage to cooling the detector below 80 K. Note that the modeled resistance does not include excess leakage current, which could limit the maximum resistance and ideal operating reverse bias voltage. The effect of reverse-biasing is to increase the

detector resistance, however a constant temperature-dependent leakage current is created. This current, in combination with the photocurrent, is a potential problem for large arrays. The current can fill the pre-amplifier capacitors quickly and force readout rates high enough to require several outputs, which dramatically increases the FPA power dissipation - a parameter dominated by the number of outputs.

#### 4.6.4 Ideal FPA Pixel Readout Rate

The current-voltage characteristics of a photodiode can be described by the ideal diode equation.

$$i = i_o \left( e^{\frac{eV}{kT}} - 1 \right). \quad (4-12)$$

Impurity, tunneling, and breakdown effects are ignored. The constant temperature-dependent saturation current is:

$$i_o = \frac{kT}{eR_o A} \cdot A. \quad (4-13)$$

The ABS coverage specification, spectral bandwidth, array size, and FOV diameter define the moving mirror velocity, scan rate, stare time, and ideal sampling rate ( $r_s$ ) of the instrument. By design, the ideal sampling rate oversamples the data, nominally by a factor of about 22 to reduce quantization and mirror velocity fluctuation noise. Each pixel in the array accumulates charge onto the pre-amplifier capacitor for a time approximately equal to the inverse of the sampling rate. At the end of the integration time, each capacitor is sampled. Pixel samples are then multiplexed onto an output line. In general the pixel readout rate ( $r_p$ ) of the FPA is constant. The pixel rate is equal to the sampling rate of the interferogram multiplied by the number of pixels in the array,

$$r_p = r_s N. \quad (4-14)$$

Table 4-8 shows the ideal sampling rate and fixed pixel rate for several array sizes between 6 x 6 and 32 x 32. Also shown is the stare time for the array to collect one interferogram and the required capacitor integration time.

**TABLE 4-8**

**The Ideal Sampling Rate, Detector Stare Time, Capacitor Integration Time, And Fixed Pixel Rate For Several Array Sizes Between 6 x 6 And 32 x 32**

Array size	$t_{\text{stare}}$ (s)	$t_{\text{int}}$ (ms)	Sampling Rate (kHz)	Pixel Rate (Mpix/s)
6x6	0.43	25	40	1.5
10x10	1.2	67	15	1.5
16x16	3.1	172	5.8	1.5
32x32	12.3	667	1.5	1.5

The required capacitor integration time increases linearly with the number of detectors in the array. Limitations on the size of preamplifier capacitors determines the maximum integration time in the LW channel. The large photocurrent in combination with the leakage current saturate the LW channel well quickly. In the next two sections, the charge storage capacity of the readout is defined, and the implications on the readout rates and number of outputs are explored.

#### 4.6.5 Preamplifier Charge Storage Capacity

During the single sample integration time in a CTIA, the signal is integrated in on-chip capacitors. The capacitor readout is usually designed to operate on a fraction of the full capacity and multiple samples may be required during an integration time to prevent saturating the capacitor. The charge stored on a readout chip capacitor is

$$C = \frac{\epsilon_0 \kappa A}{d}. \quad (4-15)$$

Here  $\epsilon_0 = 8.85 \times 10^{-2}$  pF/cm and the dielectric constant  $\kappa$  for  $\text{SiO}_2$  is 3.9. Processing capacitors thinner than  $0.1 \mu\text{m}$  is difficult due to defects in the  $\text{SiO}_2$ . We assume a thickness of  $0.05 \mu\text{m}$ . For a  $60 \times 60 \mu\text{m}$  area the capacitance is 2.5 pF if all the area under the pixel could be used. This is close to  $0.6 \times 10^{-3}$  pF/ $\mu\text{m}^2$ , a technological limit that manufacturers have mentioned during a separate investigation of LWIR detector array technology. Assuming a 10-volt swing the charge on a single capacitor would be  $1.6 \times 10^8$  electrons. The operational voltage of the chip is limited by localized breakdown considerations. Ideally the breakdown field for  $\text{SiO}_2$  is  $700 \text{ V}/\mu\text{m}$  but in practice defects limit that to about  $200 \text{ V}/\mu\text{m}$ . The applied field strength of a 10 V swing is  $200 \text{ V}/\mu\text{m}$  with a  $0.05 \mu\text{m}$  layer, which is within the design range. The total stored charge as a function of area and electric field is shown in Figure 4-30. Also shown are some vendor's estimates of maximum stored charge during normal operation of their arrays. Assuming 2/3 of the area under the detector can be used as a capacitor, a typical full-well charge capacity would be  $10^8$  electrons per pixel. The advantage of using a relatively small array, such as a  $16 \times 16$  array, is that a large capacitor can be fabricated elsewhere on the silicon readout chip for each pixel in the array. This provides more electron storage than is possible using only the area under the detector. Alternatively, the detector fill-factor per pixel could be reduced in small arrays to provide additional storage. Thus, the nominal charge storage capacity that was assumed for a relatively small ABS array is approximately  $2.8 \times 10^8$  electrons per pixel, indicated on the plot with arrows.

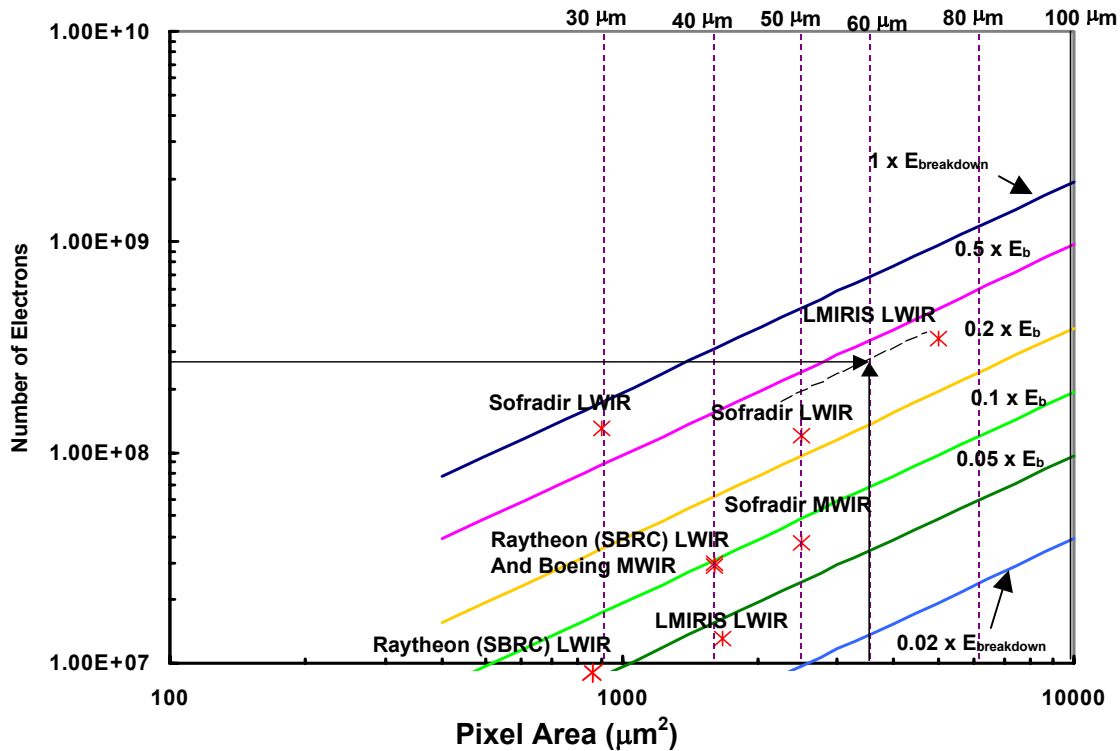


Figure 4-30. The readout capacitor storage capacity as function of area and breakdown electric field and vendor capacities. The maximum capacity under a 60x60  $\mu\text{m}$  detector is approximately  $2 \times 10^8$  electrons.

#### 4.6.6 Minimum Readout Rates and Number of FPA Output Taps

The minimum sampling rate is set by the maximum size of the integration capacitor on the readout chip. The minimum pixel readout rate (number of samples per second read from the array) is equal to the minimum sampling rate times the number of pixels in the array, as discussed in section 4.6.4. The ABS design goal was to keep the pixel rate below the maximum readout rate of a single FPA output tap, assumed to be approximately 1.5 Million samples per second. Pixel rates above 1.5 Ms/sec may require multiple outputs from the FPA. We also assume each focal plane dissipates approximately 30 mW of thermal power during operation – approximately half this figure is associated with the output, the remainder is the (small) pixel dissipation and an allowance to retain some design margin. The increased thermal load of multiple outputs would require a larger passive cooler, or possibly active cooling. To keep with the goal of a compact, lightweight instrument, each FPA should have only a single output tap.

The minimum readout rate to prevent saturation at  $2.8 \times 10^8$  electrons is shown in Figure 4-31 for the LW band assuming only photocurrent fills the capacitors. The minimum rate is also shown as a function of detector temperature for a fully reverse biased detector. Current estimates used to derive the required sampling rates were based on a nominal ABS instrument design, a 15 cm aperture, 10 km ground field-of-view, and a throughput-conversion efficiency product of approximately 10%. The minimal sampling rate on the array is approximately 5050 Hz viewing a 320 K blackbody earth scene for an unbiased detector with a bandpass from 650 to 1150  $\text{cm}^{-1}$ . The slightly increases to 5222 Hz for a reverse biased detector at 65 K. The rate jumps to 9287 Hz to accommodate the higher thermal saturation current for reversed bias operation at 80 K.

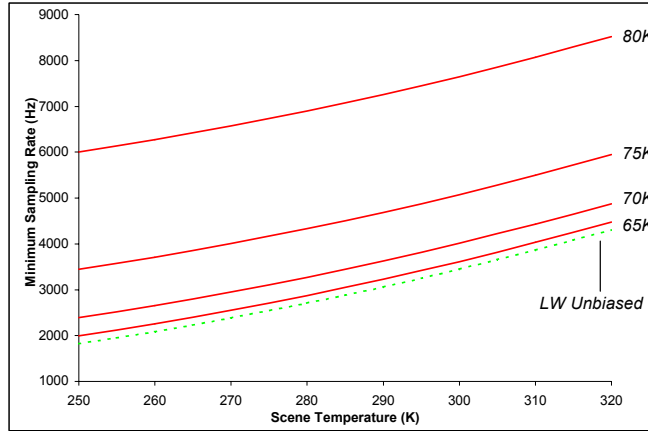


Figure 4-31. The minimum readout rates required viewing an earth scene with a  $2.8 \times 10^8$  electron integration capacity. Dashed curves for zero bias and photon generated current only, solid curves for a reversed biased detector with photon and thermal currents at listed detector temperatures.

Table 4-9 shows the minimum zero-bias readout rates for each band to prevent saturation at  $2.8 \times 10^8$  electrons. Table 4-10 shows the minimum readout rates for the LW band when fully reverse biased at different detector temperatures. Table 4-11 shows the pixel rate for different array sizes at temperatures between 65 and 80 K, fully reverse biased. A 16 x 16 array operating at 80 K requires multiple outputs. By reducing the temperature to 75 K the pixel rate is reduced, and one output is obtainable. A 10 x 10 array could operate with one output up to at least 80 K. For the range of temperatures shown, a 32 x 32 array would always require multiple outputs, and likely active cooling. Each rate was based on a 15 cm aperture and 10 km ground FOV.

**TABLE 4-9**

**The Minimal Zero Bias Readout Rate To Prevent Saturation At  $2.8 \times 10^8$  Electrons**

Band (cm <sup>-1</sup> )	Scene Temperature (K)/ Sampling Rate (Hz)							
	250	260	270	280	290	300	310	320
LW 662-1150	1824	2086	2379	2703	3057	3443	3859	4306
MW 1250-1740	185	229	285	354	438	538	656	793
SW 2150-2720	3	5	7	9	13	19	27	37

**TABLE 4-10**

**Minimum Readout Rates For The LW Band Fully Reverse Biased At Different Detector Temperatures**

Det Temp (K)	LW Band scene Temperature (K)/ Sampling Rate (Hz)							
	250	260	270	280	290	300	310	320
65	1994	2257	2550	2874	3228	3614	4030	4478
70	2390	2653	2946	3270	3625	4012	4429	4876
75	3448	3712	4007	4332	4688	5076	5494	5944
80	6004	6270	6568	6896	7255	7646	8069	8522

**TABLE 4-11**

**Minimum Pixel Rates For The LW Band Fully Reverse Biased For Several Array Sizes And Temperatures**

Array Size	Det Temp (K) / Pixel Rate (Hz)			
	65	70	75	80
<b>6x6</b>	1.6E+05	1.8E+05	2.1E+05	3.1E+05
<b>10x10</b>	4.5E+05	4.9E+05	5.9E+05	8.5E+05
<b>16x16</b>	1.1E+06	1.2E+06	1.5E+06	2.2E+06
<b>32x32</b>	4.6E+06	5.0E+06	6.1E+06	8.7E+06

**4.6.7 Aperture Diameter, Detector Temperature, and Array Size**

In this section, the well-depth and readout-rate characteristics expected of the ABS LW detectors are used to perform tradeoffs between the diameter of the instrument aperture, detector array size, detector operating temperature and number of outputs. The detector temperature and number of outputs have profound implications on the cooling trade discussed in Section 4.7. These trades are conducted for the LW band only because this band dominates the instrument cooling, and demands particular attention.

In an effort to design a lightweight, low risk instrument, these studies focused on relatively warm detector temperatures, between 75 and 80 K, so that passive cooling is a viable option. Note that the minimum aperture diameter that can be used in the 36000 km geostationary orbit, while maintaining a 10 km diameter spot on the ground, is 15 cm. Diffraction effects increase the ground spot with a smaller aperture. With this minimum, we determined the necessary aperture diameter as a function of array size to produce a LW NEdN of  $0.5 \text{ mW/m}^2/\text{sr/cm}^{-1}$  at  $720\text{cm}^{-1}$ . This is approximately where the LW performance peaks using a  $15.1 \mu\text{m}$  cutoff detector.

Figure 4-32 shows the aperture diameter and pixel rate required to meet our LW NEdN goal as a function of array size, assuming the array is operated at 80 K. Figure 4-33 shows the aperture diameter and pixel rate required to meet the goal as a function of array size, assuming a 75 K array temperature. The reduction in temperature decreases the saturation current, allowing fewer outputs. This is highly attractive because the impact on the thermal design of cooling the FPA to 75 K is more than offset by the reduced power dissipation of fewer output taps. Figure 4-33 is misleading, however, in that it implies an aperture smaller than 15 cm for large arrays. We have already demonstrated that apertures smaller than 15 cm are incompatible with a 10-km ground sample. Figure 4-34 assumes the use of a 15-cm aperture, and illustrates that increasing the array size to improve performance is not a viable option. The performance increase is slight considering the potentially severe penalty of requiring multiple outputs. Smaller arrays can operate with a single output, however the NEdN is increased. The approximate number of outputs shown on each plot is based on 1.5 MHz taps.

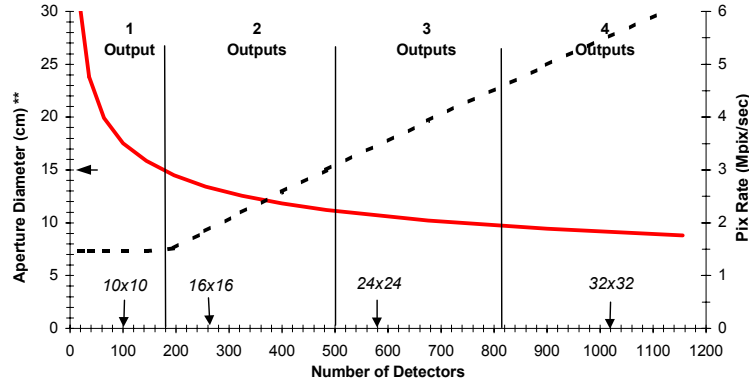


Figure 4-32. Aperture diameter (solid curve) required to meet our NEdN goal as a function of array size for a  $T = 80$  K array, the pixel rate (dashed curve) is plotted on the right vertical axis. The number of outputs required for each point is indicated based on a 1.5 MHz output tap.

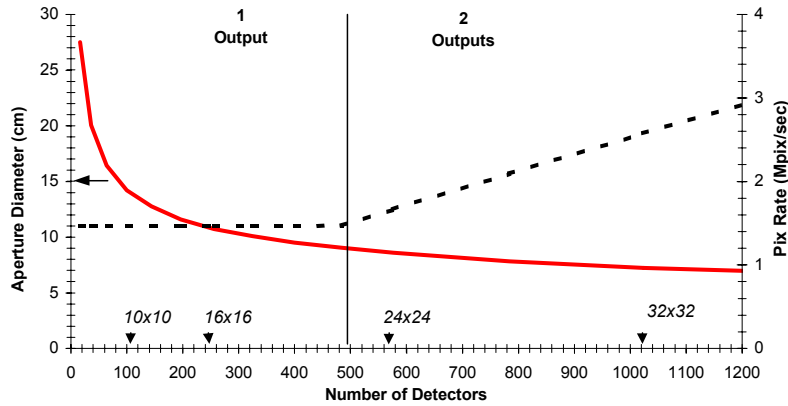


Figure 4-33. Aperture diameter (solid curve) required to meet our NEdN goal as a function of array size, assuming a 75 K array temperature, the pixel rate (dashed curve) is plotted on the right vertical axis. The number of outputs required for each point is indicated based on a 1.5 MHz output tap.

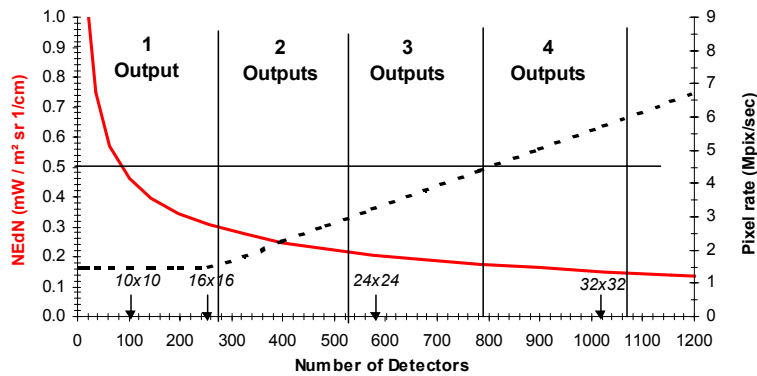


Figure 4-34. NEdN (solid curve) as a function of array size for a fixed 15 cm aperture, with the array cooled to 75 K, the pixel rate (dashed curve) is plotted on the right vertical axis. The number of outputs required for each point is indicated based on a 1.5 MHz output tap.

With the knowledge that a 16 x 16 array size appears to be the best choice, it is worth exploring whether some benefit is gained by going to a larger aperture. Figure 4-35 shows the NEdN and required pixel rate as a function of aperture diameter for a 75 K 16 x 16 array. The vertical dotted line on this plot corresponds to our need for a 15 cm minimum aperture to match the diffraction spot to a 10-km ground sample. Larger apertures offer improved performance, but at the expense of more output taps. In conclusion, 16 x 16 is the ideal array size for operating with one output and a 15 cm aperture.

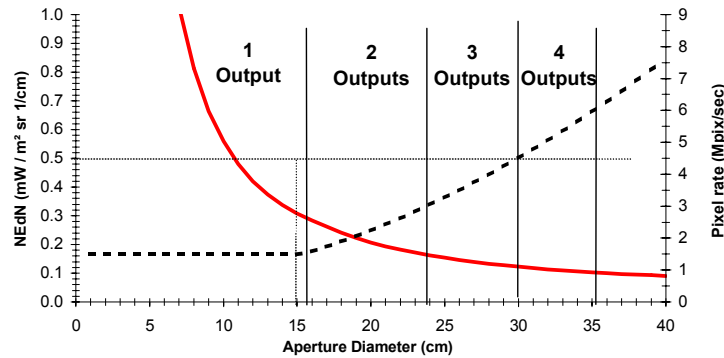


Figure 4-35. NEdN (solid curve) as a function of aperture diameter for a 75 K 16x16 array, the pixel rate (dashed curve) is plotted on the right vertical axis. The number of outputs required for each point is indicated based on a 1.5 MHz output tap. 15 cm is the minimum allowable aperture diameter.

These trade studies provide guidance in defining the ABS point design. Viable instrument parameters have been developed after examining the input aperture diameter, array size & temperature, and ROIC issues. The results allow for a relatively low risk, lightweight instrument. They show that a 15 cm aperture, 16 x 16 photovoltaic HgCdTe array in each band, and detector temperature of 75 K in the LW channel can be used. If convenient for the thermal design, the analysis of Section 4.4 demonstrates that the SW detector may be operated at up to 140 K, and the MW at up to 100 K. Such a combination will produce an instrument with a minimum LW NEdN around  $0.3 \text{ mW/m}^2/\text{sr/cm}^{-1}$ . Using colder or larger arrays, at the expense of a more complex design, can only marginally improve the performance. Colder arrays imply a larger passive cooler or greater active cooler power consumption. Similarly, the performance can be only marginally improved by increasing the aperture size, at the expense of a larger, heavier instrument. Table 4-12 gives a complete list of instrument parameters as a result of the detector and readout trade studies.



**TABLE 4-12****Trade Study Resulting Instrument, Satellite, and Signal Processing Parameters**

<b>Satellite Altitude (km)</b>	35800		
<b>Ground Sample Diameter (km)</b>	10		
<b>Extreme Field Offset (km)</b>	113		
<b>Aperture Diameter (cm)</b>	15		
<b>Band</b>	<b>LW</b>	<b>MW</b>	<b>SW</b>
<b>Spectral Band (cm<sup>-1</sup>)</b>	662 – 1150	1250 - 1740	2150 - 2720
<b>Spectral Resolution (cm<sup>-1</sup>)</b>	0.626	1.25	2.5
<b>Interferogram Sweep Time (s)</b>	3.07	1.535	0.7675
<b>Sampling Rate (Hz)</b>	6000	6000	6000
<b>Integration Time (us)</b>	165	165	165
<b>Photon Flux (ph/cm<sup>2</sup>/sec)</b>	1.8E+16	1.6E+15	3.8E+13
<b>Det. Cutoff Wavelength (μm)</b>	15.1	8	4.7
<b>Det. Temperature (K)</b>	75	75	75
<b>Pixel Size (μm)</b>	60	60	60
<b>Quantum Efficiency</b>	0.7	0.8	0.75
<b>Responsivity (A/Watt)</b>	7.7	4.5	2.6
<b>R<sub>o</sub>A (Ω-cm<sup>2</sup>)</b>	3.2	2.6E+05	4.3E+12
<b>D* (cm Hz<sup>1/2</sup>/W)</b>	1.8E+11	5.7E+11	2.1E+12

**4.7 PASSIVE RADIATIVE COOLING VS REFRIGERATION OF FOCAL PLANES**

*Key points:*

- *Temperature and power dissipation are near, but within, limits of passive cooling.*
- *Available small pulse-tube coolers are not constructed for redundancy.*
- *Detector and cold-optics temperatures are compatible with an acceptable cooler size.*

In this section, the trade study between a radiatively cooled versus a mechanically refrigerated detector focal plane array is presented. Mechanical refrigeration has become more attractive in recent years as a result of continuing development of pulse-tube coolers, which contain only a single moving part and no moving parts at the cold end. Passive radiative cooling to cold space is a more mature technology, but the detector power dissipation and operating temperatures of the ABS instrument result in a fairly large cooler geometry. The generic characteristics of the two cooling methods are summarized in Table 4-13.

TABLE 4-13

**A Few General Differences Between Passively-Cooled  
And Actively-Cooled Systems Are Highlighted**

Characteristic	Passive Cooling	Active Cooling
Detector temperature	> ~ 65 K	As low as 40 K
Detector dissipation	< ~ 200 mW	Hundreds of mW
Power consumption	None	Tens of Watts (radiate to space)
Vibration	None	mg level
Lifetime	Unlimited	10 years expected
Degradation	Graceful	Catastrophic w/o redundancy
Technology maturity	Very mature	Immature

**Assumptions.** In order to obtain a realistic trade between the use of a passive cooler radiating to the 4 K background of space, and an active pulse-tube cooler (PTC) powered from the bus and radiating waste heat to space, the following assumptions were made:

1. The detector temperature (patch or cold block) would be designed for 65 K, 70 K, and 75 K, with Joule heating used to maintain the detector at a controlled temperature 5 K higher (70, 75, and 80 K, respectively).
2. The end-of-life (EOL) emissivity of all radiating surfaces is assumed to be 0.90. Periodic outgassing of adsorbed material is assumed in the space environment for cryogenic radiators. Parasitic radiative coupling between surfaces is carried out assuming that each surface is coated with gold.
3. Three focal plane arrays (FPA's) are assumed, each dissipating a fixed amount of heat per output, and an additional fixed amount of heat per pixel. It was difficult to obtain precise figures from manufacturers, so a conservative estimate was used. A discussion of the impact of the number of outputs on FPA dissipation is included in Section 4.6.6. For the 16 x 16 arrays assumed in this trade, we use FPA dissipation of 30 mW for the SW and MW bands, and either 30 or 60 mW for the LW band, corresponding to one or two outputs, respectively, in this band.

Heat conduction via the wiring to the focal plane was estimated by assuming 10 mil diameter constantan (45% Ni, 55% Cu) wires, 20 cm long. From the electrical resistivity of this material, 49  $\mu\Omega$ -cm, and the thermal conductivity, 0.21 W/(cm K), the electrical and thermal resistance are 2  $\Omega$  and 190,000 K/W respectively. Allowing for 30 wires (including heaters, power leads, and serial data lines) onto the patch, and a 60 K temperature differential, a 10 mW allowance for wire heat conduction was used.

Passively-cooled and actively-cooled point designs were formulated for each of the three temperatures (70 K, 75 K, and 80 K) and two heat loads (100 mW and 130 mW) discussed above, and a determination of the preferred cooling method was done based on the size, mass, power consumption, and reliability of the resulting point designs.

#### 4.7.1 Passively-Cooled Design Cases

The sizing of the passive cooler was done by assuming fixed heat loads on each of three cooler stages: the patch (coldest stage), radiator (intermediary stage), and housing (warmest stage) – the names correspond to those of the GOES-N radiative cooler. The temperature of the bus and patch were fixed at some assumed value, and the remaining temperatures were allowed to vary to determine a minimum overall cooler size. The area of each stage was evaluated by solving the heat balance equations applying to it, and the sum of the three areas was determined to arrive at an overall cooler size. The process is illustrated in Figure 4-36.

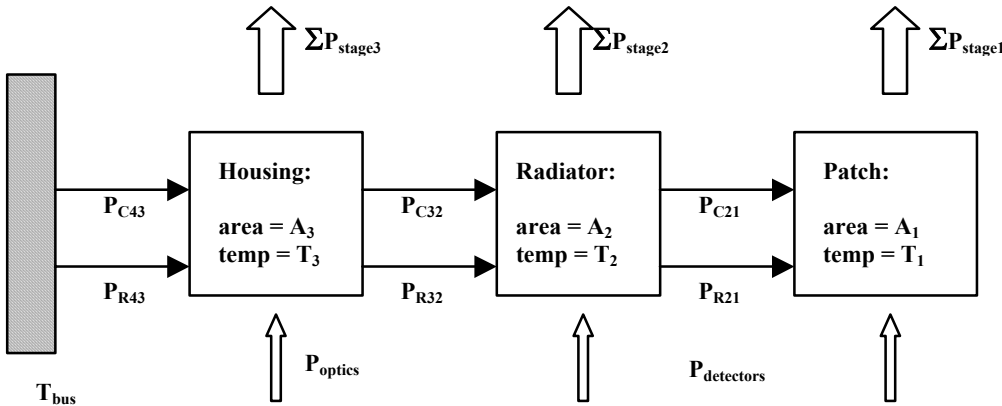


Figure 4-36. The process by which the cooler size was determined is illustrated here. Radiative terms are evaluated analytically, conductive terms are evaluated using the assumed support structure in Figure 4-37.

Application of the Stefan-Boltzmann law to the assumed 133 mW FPA dissipation results in a calculated radiator area of about 1100 cm<sup>2</sup> at 70 K, or about 13" square. Adding an allowance for conducted and radiated parasitic heat into the patch so that 200 mW total must be radiated leads to a figure of 1630 cm<sup>2</sup>, or about 16" square. Assuming that the patch is fabricated from a quarter-inch thick aluminum plate lightened to 60% of its nominal density of 2.923 g/cm<sup>3</sup>, a patch mass of about 2 kg is arrived at.

The assumed mechanical layout of the passive cooler is shown in Figure 4-37. It has three square stages, each nested within the next-warmest stage. The support structure isolating the cooler stages from each other must be mechanically rigid, have minimal thermal conductance, and must maintain the alignment between the interferometer back optics and the detectors when it cools to its operating temperature. A suitable structure to support the above-derived patch mass is shown in Figure 4-37. It employs eight G-10 fiberglass-epoxy structures, each 1.84 " long, 3/4 " wide, and 1/32 " thick. This construction was chosen to avoid vibrational resonant modes under assumed satellite operating conditions. Using a thermal conductivity for G-10 of 2.94 mW/(cm K), a thermal conductance  $G=0.100$  mW/K is obtained for each leg, and  $G=0.804$  mW/K for the overall structure. The thermal conductivity used in the calculation applies at 300 K – the value at 100 K is about 40% lower<sup>22</sup>, however in the interest of maintaining some design margin we neglect the temperature dependence of thermal conductivity.

<sup>22</sup> R. P. Reed and A. F. Clark, "Materials at Low Temperatures", American Society of Metals, 1983

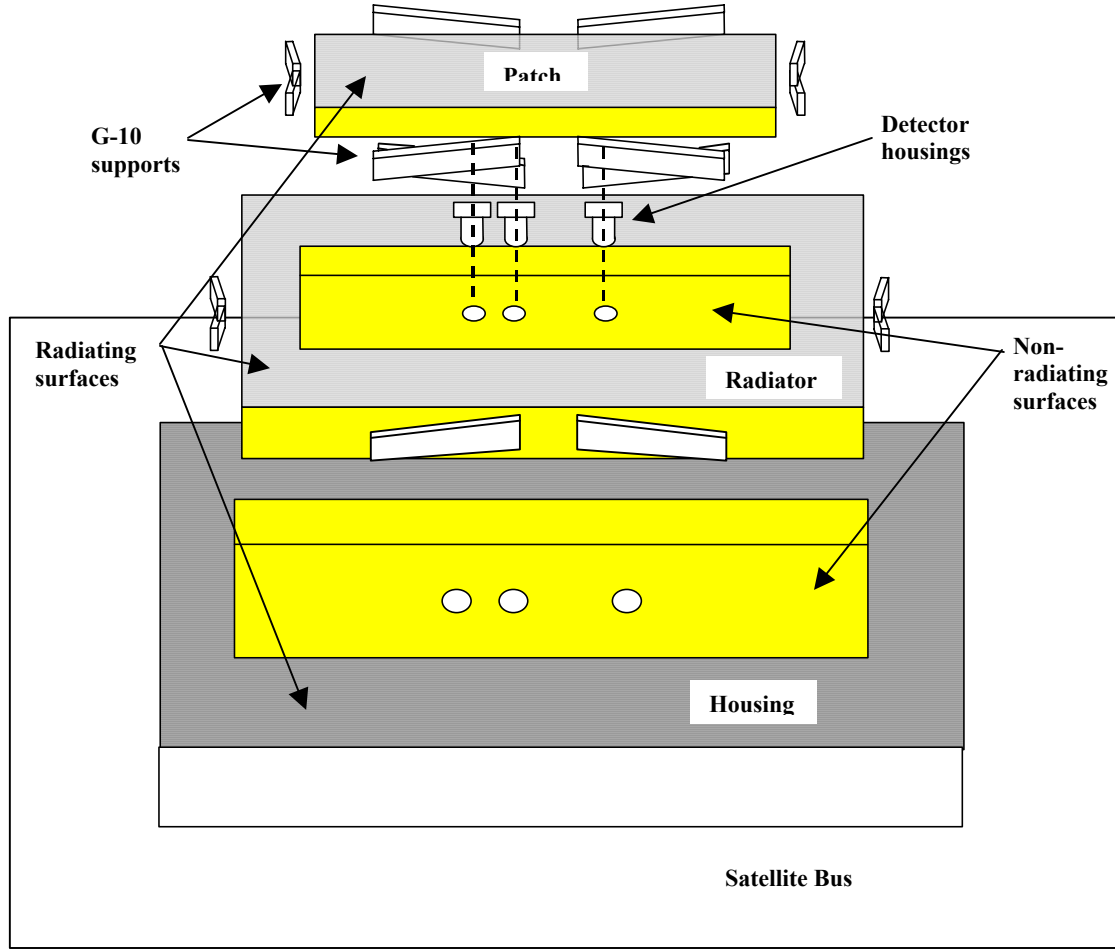


Figure 4-37. The mechanical layout of the radiative cooler is illustrated.

It was next assumed that these thermal conductances doubled between cooler stages: that is, it was assumed that the radiator mass could be limited to that of the patch, and the housing mass could be limited to twice that of the patch. The conductive inputs were then estimated for each of the three stages using the expression

$$P_{Cji} = G_{ji} (T_j - T_i), \quad (4-16)$$

where the subscripts j and i conform to the notation of Figure 4-36. The radiative inputs were estimated using

$$P_{Rji} = \epsilon_{eff} \sigma (A_j + A_i) (T_j^4 - T_i^4). \quad (4-17)$$

The effective emissivity of the gold-to-gold radiative input between the cooler stages is found from<sup>23</sup>

$$\epsilon_{eff} = \frac{\epsilon_1 \epsilon_2}{\epsilon_1 (1 - \epsilon_2) + \epsilon_2} = 0.0101, \quad (4-18)$$

<sup>23</sup> Russell B. Scott, "Cryogenic Engineering", Van Nostrand, 1959.

where  $\varepsilon_1$  and  $\varepsilon_2$  are assumed to be 0.02 for gold. The  $A_j$  term in equation (4-17) accounts for radiative input to the back of the radiating portion of the stage in question, while the  $A_i$  term accounts for the radiative input to the back of the nonradiating portion of the stage, i.e. to the portion of the stage underlying the next-colder stage. This second term is omitted in the patch.

The overall stage area was found by arranging the heat balance to solve for the area of the stage in question:

$$A_j = \frac{P_j + P_{Cji} + \varepsilon_{eff} \sigma A_i (T_j^4 - T_i^4)}{\varepsilon_r \sigma (T_j^4 - T_b^4) - \varepsilon_{eff} \sigma (T_j^4 - T_i^4)} \quad (4-19)$$

The overall cooler size is then found by adding three instances of equation (4-19), one for each stage, to obtain an expression for the total stage area as a function of six parameters: the three stage temperatures, and the three (non-parasitic) heat loads. These parameters can be varied to try to find the smallest overall cooler size.

As an example of this process, assume that the detectors are all heat-sunk to the patch, which must be maintained at some temperature  $T_p$ . The interferometer and back-optics are heat-sunk to the housing at  $T_h$ . The radiator carries no heat load other than parasitic terms, and can be maintained at any temperature  $T_r$  which is convenient. The passive cooler was sized for uncontrolled patch temperatures of 65, 70, and 75 K. Once the cooler dimensions were determined, the quantity of joule heating was calculated necessary to maintain the patch control temperatures of 70 K, 75 K, and 80 K, respectively. The cooler area was solved over the range  $90 < T_r < 140$  K. An example of the results for one design case (130 mW detector power on the patch at 70 K) is shown in Figure 4-38. There is a minimum in the overall cooler size corresponding to a 125 K radiator stage.

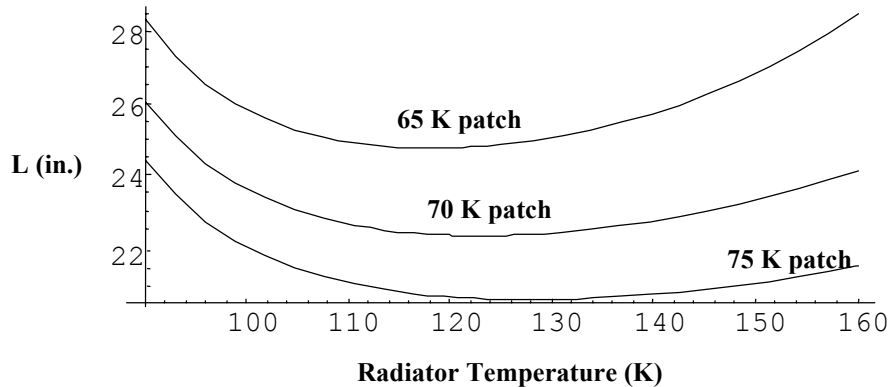


Figure 4-38. A plot of the side length of a square three-stage cooler is shown for a 70 K (uncontrolled) patch temperature as a function of the radiator temperature.

Radiant coolers were sized for the three uncontrolled patch temperatures mentioned above, and for three detector options:

1. All detectors heat-sunk to the patch

2. SW detector heat-sunk to the radiator, with  $T_{\text{radiator}}$  allowed to assume the value which minimizes the overall cooler area (the MW detector is BLIP up to 140 K).
3. SW and MW detectors sunk to the radiator, with  $T_{\text{radiator}} = 100$  K to maintain the MW detector in the BLIP condition.

The dimensions for these design cases is summarized in Table 4-14, along with the quantity of control power necessary to maintain the patch (and the detectors) at a temperature 5 K higher. The table is organized in terms of this control point, since all other sections in this report are presented in terms of this temperature.

**TABLE 4-14**  
**A Summary Of The Passive Cooler Design Cases**  
**Considered In The Trade Study**

Parameter	Focal plane dissipation = 100 mW			Focal plane dissipation = 130 mW		
$T_{\text{patch}}$ control	70 K	75 K	80 K	70 K	75 K	80 K
Case 1: All three detectors sunk to patch						
$T_{\text{radiator}}$ (K)	120	125	130	120	125	130
$A_{\text{patch}}$ (cm <sup>2</sup> )	1797	1311	981	2171	1585	1186
$A_{\text{radiator}}$ (cm <sup>2</sup> )	406	275	194	455	305	212
$A_{\text{housing}}$ (cm <sup>2</sup> )	1324	1320	1318	1325	1321	1319
$A_{\text{overall}}$ (cm <sup>2</sup> )	3527	2907	2493	3952	3211	2716
$P_{\text{control}}$ (mW)	67	60	55	80	72	65
Case 2: LW and MW detectors sunk to patch, SW detector sunk to radiator						
$T_{\text{radiator}}$ (K)	120	125	130	120	125	130
$A_{\text{patch}}$ (cm <sup>2</sup> )	1385	1011	756	1797	1312	981
$A_{\text{radiator}}$ (cm <sup>2</sup> )	388	272	199	439	302	217
$A_{\text{housing}}$ (cm <sup>2</sup> )	1323	1320	1318	1325	1321	1319
$A_{\text{overall}}$ (cm <sup>2</sup> )	3097	2604	2274	3561	2935	2517
$P_{\text{control}}$ (mW)	53	47	43	67	60	55
Case 3: LW detector sunk to patch, MW and SW detector sunk to 100 K radiator						
$A_{\text{patch}}$ (cm <sup>2</sup> )	707	483	336	1136	796	572
$A_{\text{radiator}}$ (cm <sup>2</sup> )	918	843	793	1044	930	855
$A_{\text{housing}}$ (cm <sup>2</sup> )	1338	1336	1335	1342	1339	1337
$A_{\text{overall}}$ (cm <sup>2</sup> )	2964	2662	2465	3522	3065	2763
$P_{\text{control}}$ (mW)	27	24	21	42	36	32

In order to make a trade decision between passive and active cooling, we now consider actively-cooled designs for a similar set of focal plane temperature and power dissipation assumptions. These will then be compared with the results in Table 4-14.

#### 4.7.2 Actively-Cooled Design Cases

Mechanical refrigeration of infrared sensors has long been practical, however reliability concerns have precluded its use in spaceborne remote-sensing applications. Continued development of Stirling-cycle and pulse-tube coolers has brought projected lifetimes up to the ten-year range, and greatly reduced mass and volume. The flexure bearings used in these coolers make them highly reliable, and in the case of pulse-tube coolers no moving parts are present on the cold head.

A Stirling-cycle cooler relies on the use of two pistons located on the opposite sides of a regenerator which may be described as a “heat sponge”, alternately absorbing heat from the working fluid (usually helium) and returning heat to it. The Stirling-cycle cooler cycles through a four-step process, which is composed of the following steps:

1. Compression of the working fluid at the warm side of the regenerator. The heat of compression,  $Q_h$ , is removed by a warm-side heat exchanger so that the temperature  $T$  remains constant.
2. Transfer of the (compressed) working fluid through the regenerator, from warm side to cold side. The fluid cools at constant volume, with heat transfer to the regenerator.
3. Expansion of the working fluid at the cold side of the regenerator. Heat  $Q_c$  from the cold tip of the refrigerator is added to the fluid by a cold-side heat exchanger so that  $T$  remains constant.
4. Transfer of the (expanded) working fluid through the regenerator, from cold side to warm side. The fluid warms at constant volume, with heat transfer from the regenerator. The refrigerator has now returned to its initial state.

A pulse-tube cooler operates on principles similar to those of the Stirling cycle cooler, except that the cold-side piston is replaced by a compressible volume of fluid. The heat flow in the PTC is from a cold heat exchanger at the end of the pulse tube adjacent to the regenerator to a warm heat exchanger at the opposite end of the pulse tube.

The active cooler chosen for the trade study was the TRW PTC 7203, a small space-qualified pulse-tube cooler featuring an expected lifetime of 10 years and a mass of 2 Kg. The characteristics of the PTC 7203 are compiled<sup>24</sup> in Table 4-15. For the purposes of the trade study, only the demonstrated performance of the TRW coolers was used. Conversations with TRW engineers indicate, however, that substantial gains are expected in the near term (2 to 3 years) which will make the pulse-tube coolers a more attractive choice for the ABS application.

The primary disadvantage of the PTC 7203 is that it was not designed for use in a redundant configuration, where the off-state thermal load of the de-energized cooler is substantially larger than the FPA dissipation. Although thermal switches have been developed which can be used to disconnect a de-energized cooler from the detectors<sup>25</sup>, they are unlikely to be available for small coolers. The task of

---

<sup>24</sup> Disclaimer: our selection of the PTC 7203, and use of figures quoted in this table, are made only as necessary to support the design cases in this section. We believe these figures are accurate.

<sup>25</sup> T. Slater, et. al., “Thermomechanical characteristics of a thermal switch,” *Sensors and Actuators A*, Vol. 53, pp. 423-427, (1996).

disconnecting a failed cooler from the focal plane may be achievable through one-time-only (e.g. explosive) actuators, but the risk of ruining the alignment of the optics is considerable.

**TABLE 4-15**

**The Performance Of The TRW PTC 7203 Is Summarized**

Parameter	Demonstrated as of August, 1998
Compressor	Flexure bearing, linear drive
Working fluid	Helium, 400 psig
Vibration	<0.1 N, 3 axes (1N = 0.098 g-Kg)
DC Magnetic field	200 mG @ 50 cm ( $1/R^3$ )
Size	31 cm long, 11 cm dia
Mass	2 Kg
Temperature range	255-320 K
Off-state load	400 mW
Thermal switching	None
Maximum input power	24 W
Refrigeration	60 K no-load, 33 mW/K @ rated max. 60 K no-load, 28 mW/K @ 20 W input 63 K no-load, 23 mW/K @ 15 W input

For the purposes of the trade study, point designs for an actively-cooled instrument using one and two PTC-7203's were generated. Designs using a single PTC would become inoperative upon failure of the cooler. Designs using two PTC's would be redundant at a detector temperature of 80 K (where one PTC can sink the thermal load of both the detectors and the de-energized cooler). Designs at colder temperatures would require running both coolers and would operate at a back-up temperature of 80 K upon failure of one PTC. Passive coolers are retained, one to dissipate the 15 W load from the optics bench at 220 K, and a second cooler to dissipate the waste heat (primarily the electrical power consumption) from the PTC's at 300 K. The active cooling scheme is illustrated in Figure 4-39.

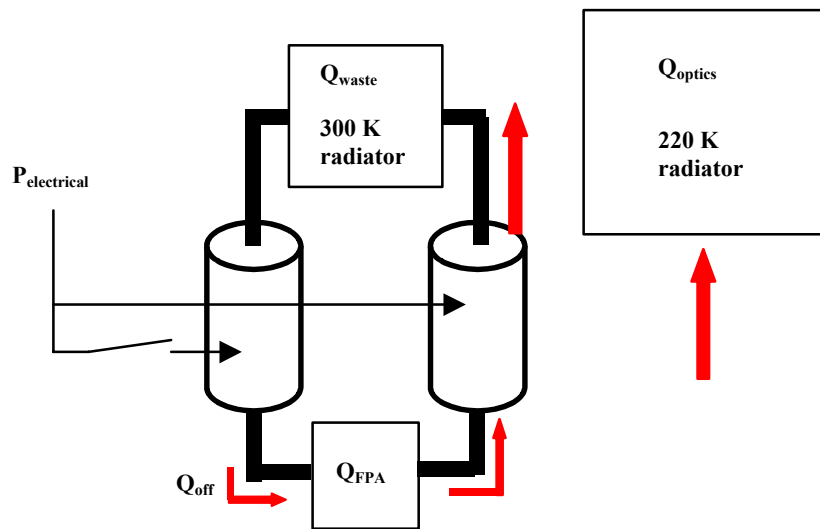


Figure 4-39. The assumed configuration for an actively-cooled design is shown, with one PTC de-energized. If both PTC's operate, they each pump heat symmetrically.



**TABLE 4-16**

**Actively-Cooled Designs Considered In The Trade Study**

Parameter	P = 130 mW		
T <sub>patch</sub>	70 K	75 K	80 K
Case 1: Single non-redundant cooler			
A <sub>220K</sub>	1255 cm <sup>2</sup>		
A <sub>300K</sub> (cm <sup>2</sup> )	496	375	375
Redundant?	No	No	No
T <sub>backup</sub>	-	-	-
P <sub>electrical</sub> (W)	20	15	15
P <sub>control</sub> (mW)	150	145	260
Case 2: Two coolers, with backup operation upon failure of one			
A <sub>220K</sub>	1255 cm <sup>2</sup>		
A <sub>300K</sub> (cm <sup>2</sup> )	738	738	496
Redundant?	Partially	Partially	Yes
T <sub>backup</sub>	80	80	80
P <sub>electrical</sub>	30	30	24
P <sub>control</sub>	150	145	260

The actively-cooled designs for various detector operating temperatures and cooler configurations are summarized in Table 4-16. No figures are shown for 100 mW power dissipation because no substantial change in the figures is seen. Comparing this data to that for the passively-cooled designs in Table 4-14, what immediately becomes clear is that a substantial area on the instrument must still be dedicated to passive cooling. This is largely due to the assumption that the 220 K optics bench must be passively cooled.

### 4.7.3 Passive/Active Trade Decision

The radiators which are retained in the active cooling scenario occupy roughly half the footprint of the purely passive case, and the deleterious effects (vibration, DC magnetic field) of the active cooler make this a less attractive proposition than purely geometric arguments might imply. It is true, however, that pulse-tube coolers are improving substantially in their performance as time goes on, and if the projected (rather than current) performance of these units were used the advantage of passive cooling would be less clear, particularly at 70 K. Based on current PTC performance, however, the decision was made to pursue a passively-cooled system. Moreover, as Table 4-14 makes clear, there is no substantial benefit to be gained by moving some of the detectors to the radiator stage. We conclude that for the point-design, all three detectors are heat-sunk to the patch at 75 K (control point), that the radiator operates at 125 K, and that the optics bench is heat-sunk to the housing at 220 K.

## 4.8 VISIBLE CHANNEL DESIGN

*Key points:*

- *The same channel can be used for cloud-cover imaging and star-sensing operations.*
- *Nighttime cloud-cover imaging is possible for approximately half of each month.*
- *The star-sensing method is simplified by use of a CCD array.*

The best retrieval results are obtained from clear sky conditions; therefore, it must be possible to verify that the ground sample for which a sounding is being performed is free of cloud cover, which can corrupt the retrieved profile. This requires the presence of a visible channel in the sounder, with its IGFOV's co-aligned with the infrared fields of view. An accurate measurement of the degree to which clouds encroach on the 10-km IR samples requires that the visible sample IGFOV must be substantially smaller for higher resolution. Moreover, image navigation and registration requires a visible channel for star-sensing in order to calibrate the INR system. This section describes the visible channel that is incorporated into the ABS instrument design to support both of these functions.

#### **4.8.1 Required coverage**

The trade studies conducted in Section 4.6 led to the assumption that the IR array format will be 16 x 16 pixels. When combined with the 10-km ground sample diameter, this leads to the requirement for visible coverage of 160 km x 160 km. In order to provide ground samples of 0.5 km x 0.5 km while utilizing the same scan mirror, an array of 320 pixels x 320 pixels is required. Although using a somewhat larger visible array would provide more ground coverage in the visible channel at the cost of a larger data volume, the ground resolution would not be maintained due to the increasing off-axis optical aberrations. Because a 320 x 320 array size is not commonly produced by vendors, two options exist for the array format: either a 320 x 320 format that is transmitted to the ground, or a 1024 x 1023 format with only a 320 x 320, edge-located portion that is transmitted to the ground.

#### **4.8.2 CCD Requirements**

Requirements for a CCD array begin with a fast frame rate, so that the time to read out an image is small compared to an integration time. This is necessary because as the image is clocked out of the CCD it will be smeared by the continued exposure to scene flux, and a mechanical shutter adds a mechanism with the possibility of wear and failure. A commercial frame transfer device is available which can shift 320 rows of pixels to the buffer in 1 ms. By observing for 10 times longer, the gradient of collected flux across the image should be less than 10% in the last row, which would suffer the greatest impact.<sup>1</sup>

For a ground sample diameter of 0.5 km, resulting from the above sub-sampling requirement, and the 86.4-cm focal length from the optical design, a pixel size of 12  $\mu\text{m}$  is required. Since no signal to noise ratio (SNR) is specified for this channel, we use the imager visible band requirements as a guideline. The NWS draft requires a visible SNR of about 600 at 100% albedo for the imager, compared to the SNR of about 300 from the current GOES imager<sup>2</sup>. The expected photon flux therefore requires an electron storage capacity ("well depth") of about  $(600)^2$  or  $3.6 \times 10^5$  electrons. This is within the capability of currently available CCD's and will not challenge the design.

Commercial devices are available with low dark current at 25°C, which permits a thermoelectric temperature stabilization of the CCD temperature. The simulated performance results can meet the signal to noise requirements when the characteristics of the previously- mentioned commercial array are used. The array has 12- $\mu\text{m}$  pixels, 400,000 electron capacity per pixel, a quantum efficiency of 30%, a read noise of  $\pm 18$  electrons per pixel, and a dark current of about 180 electrons per pixel per second.

#### **4.8.3 Cloud Cover Detection**

In the baseline design, the visible channel will sense clouds in the daytime with a signal to noise ratio of 590 in a 10 ms integration. This assumes a visible path transmittance of 60%, which is based on

---

<sup>1</sup> G. Berthiaume, LL internal study, private comm.

the assumptions of 99% transmittance on each of 5 lens surfaces, 85% transmittance for the visible/IR dichroic, 75% transmittance for the 0.52  $\mu\text{m}$  to 0.72  $\mu\text{m}$  visible filter, and a neutral density filter. The 10 ms integration time required to minimize image blurring also requires a neutral density filter that reduces the incoming flux by a factor of 3.5. Requiring a lower signal to noise ratio would require either a shortened integration time or a decreased neutral-density-filter transmittance. The latter would reduce the visible channel performance when the array is used for star sensing navigation.

Nighttime cloud detection using moonlight is possible, but its effectiveness varies during the lunar cycle as the amount of available moonlight changes. We assume that the neutral density filter that attenuated the light by a factor of 3.5 is permanently located in the optical path. For the full moon, the signal to noise would be 8.5 for 0.5-km resolution (neglecting jitter), using the IR integration time of 3 seconds. For 1.5-km resolution (achievable by summing adjacent pixels), a signal to noise of 29.3 could be obtained in 3 seconds, and for 5-km resolution the SNR would be 99.7. By the quarter moon (seven days before or after the full moon), the illumination would afford a signal to noise of only 1.0 in 3 seconds with 0.5 km resolution (neglecting jitter), a signal to noise of 3.5 with 1.5-km resolution, and a SNR of 12 with 5-km resolution. This assumes 100% albedo at the earth. Therefore the presence of some clouds could be detected at night during about half of the month, provided a reduction in resolution is acceptable.

The visible pan band can also be used for other observations of the earth. If an expansion of the capabilities of the instrument were called for, it would be possible to investigate the addition of a filter wheel mechanism for narrow visible band coverage.

#### **4.8.4 Star Sensing**

The current GOES sounder has separate detectors for IR coverage and for mirror position error correction performed by viewing a known star location. As described in the operational manual for the GOES I-M Sounder<sup>3</sup>, the scan mirror is rotated toward a known star position. The mirror is held fixed while a star drifts through the field of the detectors at a rate of 72  $\mu\text{rad}/\text{sec}$ . Sampling the output of all 8 detectors in the array will indicate which pixel saw the star, this providing location information in one direction. Information in the other direction is obtained by determining the exact time of crossing of the array from the sampled output.

With a CCD array, the scan mirror would be rotated to point at the known star's coordinates, positioning that spot in the sky onto the center pixel of the 320 x 320 array. Error in the mirror positioning would then be evident as an offset between the known star's image and the center of the array. These two methods are illustrated in Figure 4-40.

---

<sup>3</sup> *Sounder Operational Reference Manual* prepared by ITT Aerospace/Communications Division, Fort Wayne, IN, for Space Systems/Loral, Palo Alto, CA, October 1993.

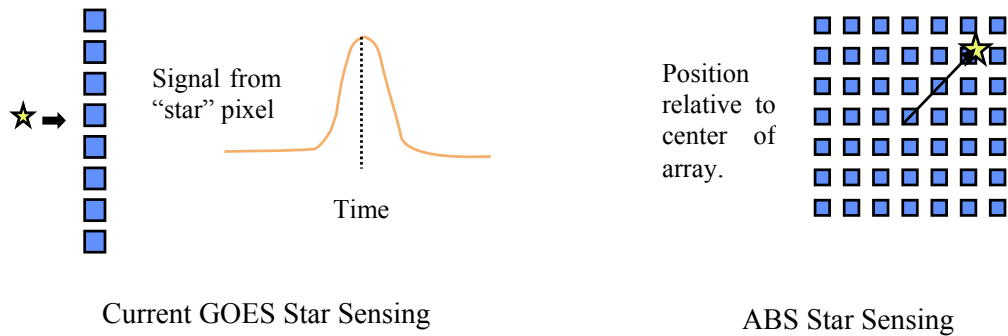


Figure 4-40. Current GOES star sensing methodology versus ABS star sensing methodology.

The star sensing requirements for the current GOES is to be able to detect a fourth magnitude star ( $m_v = 4$ ) of spectral class B0 (or greater) with a signal to noise ratio of 6.<sup>4</sup> The blackbody temperature of a class B0 star is about 23,100 K while the M0 class temperature (greater) is about 3,500 K providing about roughly half of the irradiance of the B0 star. Although 7 seconds are allocated for the star's image to drift across the detector in the current GOES sounder, the B0 star could be detected in about 9 ms, while the M0 star could be detected with a signal to noise ratio of 6 in about 30 ms.

For the same fourth-magnitude, class-B0 star, the signal to noise ratio from the CCD array would be 9 in 100 ms with the presence of the neutral density filter required for the daytime earth observations. For a class M0 star, the signal to noise ratio should be 5 in 100 ms. The star would have drifted about 7  $\mu\text{rad}$  during the integration. This should be compared against the angular pixel size of about 14  $\mu\text{rad}$ , which is about twice as large.

Although the sensor meets the signal to noise of the current star sensor, larger signal to noise ratios could be obtained from the array with longer integration times. By allowing a star to streak across multiple pixels, longer integration times would be permitted. A centroiding technique could then be used on the streak to determine the exact location of the image of the star at a fixed point in time. For a class B0 star, a signal to noise value of 23 could be obtained in one second from a star image that extended over roughly 5 pixels in length.

#### 4.8.5 Visible Data Impact

The baseline design assumes that one, 320-pixel x 320-pixel, visible image is transmitted for each 3-second IR integration. Section 4.9.1 considers the resulting 400 kbps data stream, and demonstrates that it is negligible in comparison with the IR data stream.

#### 4.8.6 Conclusion

A 320 pixel x 320 pixel, frame transfer, CCD array will provide simultaneous coverage of the same ground coverage as the IR array but with 0.5-km resolution, which is very good resolution of the earth for cloud detection. Because commercial availability of this format may be a problem, a 1024 x

<sup>4</sup> *GOES Imaging and Sounding Subsystems: Special Analysis Report on Radiometric Performance of the Imager and Sounder*, Vol.1, prepared by ITT Aerospace/Communications Division, Fort Wayne, IN, for Space Systems/Loral, Palo Alto, CA, November 1993.

1024 pixel array may be used, provided only the data from a 320 x 320 portion of the array adjacent to the frame transfer buffer is transmitted to ground. The data accumulation rate is only about 5% of the IR data accumulation rate.

The signal to noise provided by this visible array would be about 600 in 10 ms in the daytime, assuming the presence of a neutral density filter to decrease the flux by a factor of 3.5. The presence of the filter is necessary to reduce the image smear to < 10% during the readout of the array. This is the baseline visible-channel capability. Nighttime cloud detection using moonlight can be performed during about one half of the month with signal to noise values greater than about 12, provided reduced ground resolution to 5 x 5 km is permitted.

Star sensing can also be accomplished by the same array, with the mirror positioning error determined by placing the expected position of a known star at the center of the array and measuring the offset to the observed stellar image. The signal to noise requirement of 6 for a B0 or better class star can be met by a commercial CCD array even in the presence of the neutral density filter. If star streaking and centroiding is permissible during the integration, significantly improved signal to noise values can be obtained with the CCD by simply increasing the integration time.

## 4.9 DATA-PROCESSING ELECTRONICS TRADES

*Key points:*

- *The high raw data rates can be processed to fit within the existing GOES downlink bandwidth using FIR filtering of oversampled data implemented via a DSP engine.*
- *If bandwidth can be expanded, other operational modes (e.g. multiple visible bands) become possible.*
- *14-bit A/D conversion is sufficient to minimize quantization noise.*

### 4.9.1 Overview

This section briefly describes the signal-processing architecture for the Advanced Baseline Sounder. The scheme uses on-board decimation processing of interferometer data, thereby implying over-sampled operation. An earlier MIT Lincoln Laboratory study<sup>26</sup> on the GHIS sounder concept evaluated various processing options and concluded that a decimating FIR filter algorithm, without any on-board FFT spectral conversion, would meet GOES bandwidth and coverage rate requirements. Similar constraints govern ABS operation, and thus conclusions about GHIS signal processing are generally applicable to potential ABS implementations.

The ABS needs to cover an area of 3000 km by 5000 km within thirty minutes. Every hour, the instrument should also be able to accommodate 5-10 minutes worth of IR calibration and an occasional 1000 km x 1000 km sounding. These coverage requirements thus establish the raw, unprocessed data rate. To gauge the magnitude of this rate, consider a nominal operating configuration as indicated in Table 4-17. (Alternative operational modes are discussed below.) The integration period stems directly from the coverage rate, pixel ground spot size, and array size:

$$256 \cdot (30 \text{ min} \cdot 60 \text{ s/min}) \cdot \frac{10 \text{ km} \times 10 \text{ km}}{3000 \text{ km} \times 5000 \text{ km}} \approx 3.1 \text{ s} . \quad (4-20)$$

---

<sup>26</sup> W. E. Bicknell, et. al., "GOES High-Resolution Interferometer Study," MIT Lincoln Laboratory, Lexington, MA, Project Rep. NOAA-12 (5 June 1995).

**TABLE 4-17**  
**ABS Nominal Operation**

<b>Instrument Parameter</b>	<b>Default Design Value</b>
IR Detector Array Size	16x16 pixels
Integration Time	3.1 s
Interferometer Mirror Turn-around Time	0.025 s
Metrology Sampling Rate	11000 cm <sup>-1</sup>
Maximum Spectral Resolution	0.625 cm <sup>-1</sup>
A/D Size	14 bits

Assuming a double-sided interferogram (with total OPD range of 1.6 cm for the longwave channel) thus produces:

$$\frac{11000\text{cm}^{-1}}{0.625\text{cm}^{-1}} \cdot \frac{1}{3.1\text{s}} \approx 5730\text{ frame/s of } 16 \times 16 \text{ data} . \quad (4-21)$$

This corresponds to:

$$256 \cdot 5730 / \text{s} \cdot 14 \text{ bits} \approx 20.5 \text{ Mbps} . \quad (4-22)$$

Similar calculations apply for midwave (OPD = 0.8 cm) and shortwave (OPD = 0.4 cm) channels, with the total throughput of valid data decreasing at each scan-range transition. The maximum rate would occur around  $\pm 0.2$  cm OPD when all three channels are simultaneously generating valid interferograms, and yields  $3 \cdot 20.5 \approx 61.6$  Mbps. Considering only the valid data scan regions results in  $20.5 + 10.2 + 5.1$  or approximately 35.8 Mbps for all three channels. It is also possible to use a different sampling rate for each band, but this approach is somewhat more complicated to implement in hardware and is not adopted here.

Add to this rate an additional data stream corresponding to simultaneous 320 x 320 pixel visible imagery sampled at 12 bits:

$$320 \times 320 \cdot \frac{1}{3.1\text{s}} \cdot 12 \text{ bits} \approx 0.4 \text{ Mbps} . \quad (4-23)$$

The IR calibration data rate is insignificant by comparison, and therefore is not a driver on throughput requirements. An occasional mesoscale 1000 km x 1000 km sounding, with rate:

$$\frac{1000 \times 1000}{3000 \times 3000} \cdot 35.8 \text{ Mbps} \approx 4 \text{ Mbps} , \quad (4-24)$$

together with 0.4 Mbps visible data, would also not represent a stressing operational mode for sounder throughput.

The maximum total unprocessed data rate is therefore  $35.8 + 0.4 \approx 36$  Mbps. The ABS instrument's primary signal-processing objective is to fit this raw data rate into a reasonable projected

allocation for the advanced sounder's communication downlink. As indicated above, the method adopted for the Lincoln Laboratory point-design uses a decimating FIR filter on the over-sampled interferograms.

Figure 4-41 depicts the signal flow for each of three different IR wavebands. After amplification, the IR detector signals are filtered with a lowpass, anti-aliasing filter prior to digitization. To ensure reasonable transition characteristics for this analog filter, the signal is over-sampled and then decimated before transmission to ground. Such a scheme permits trading off the sampling rate against analog filter complexity. Over-sampling has the added benefit of reducing the required number of bits on the A/D for a given signal-to-noise ratio. The price, however, is a greatly increased raw data rate. A decimating bandpass filter, implemented with digital hardware, reduces this raw data rate by isolating the relevant spectral region for each waveband channel without requiring any on-board FFT conversion.

An appropriate decimation factor will depend on how fast the metrology system generates sample clock pulses. The ABS instrument, if implemented as an FTS, will need a reference interferometer to permit spatial rather than temporal sampling.<sup>27</sup> This allows the sampling clock to track any variations in the FTS's moving mirror. Such a metrology system generally uses a narrowband source to create quasi-monochromatic fringes for triggering the A/Ds. A laser source is ideal, but there has not been much long-life flight experience with lasers. The point-design adopted here proposes a diode laser for use as the metrology source, with a wavelength in the 0.8-1.5  $\mu\text{m}$  range. Reliability of this laser will clearly be an important design concern.

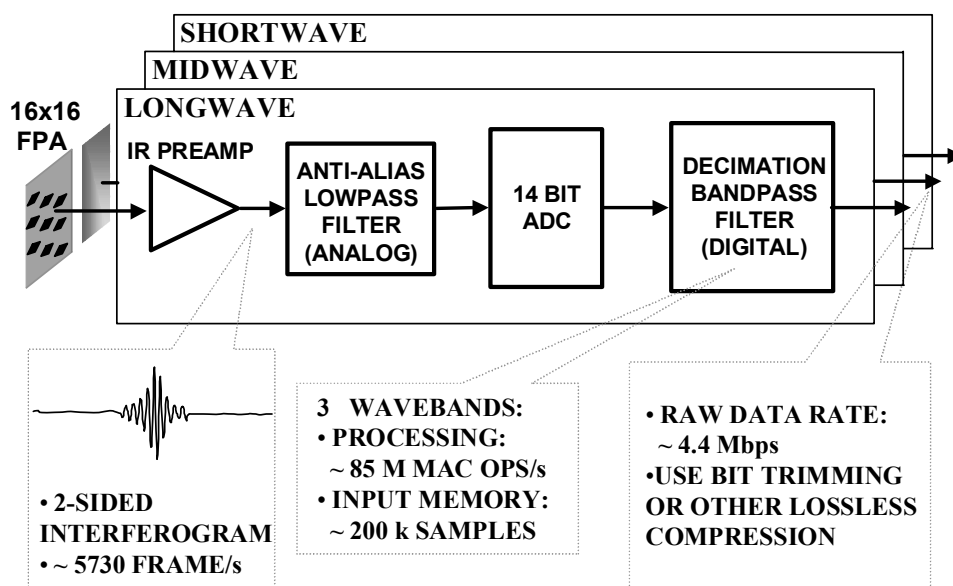


Figure 4-41. ABS Signal Processing Architecture.

The metrology system for MIT/LL's GHIS brassboard had a 1.5  $\mu\text{m}$  diode laser, and used every rising and falling edge to yield approximately  $13055 \text{ cm}^{-1}$  for the effective sampling rate.<sup>28</sup> The nominal

<sup>27</sup> L. M. Candell, et. al., "Electronic Considerations for a Geostationary Interferometer Sounder," SPIE Proc., Vol. 2812, pp. 446-52, 1996.

<sup>28</sup> W. E. Bicknell, et. al., "GOES High-Resolution Interferometer Sounder (GHIS) Brassboard Test Program," MIT Lincoln Laboratory, Lexington, MA, Project Rep. NOAA-22 (22 July 1998).

ABS sampling rate of  $11000 \text{ cm}^{-1}$  indicated above corresponds to the rising edges of a diode lasing at approximately  $0.91 \text{ } \mu\text{m}$ . Given the PV detectors' full-well constraint discussed in Section 4.6, this rate suggests an appropriate decimation factor of  $11000/580 \approx 19$  for channel bandwidths of about  $580 \text{ cm}^{-1}$ . Filtering and then decimating the interferograms by this amount would therefore produce an output data stream of

$$\frac{36}{19} \cdot 2 \cdot \frac{16}{14} \text{ Mbps} \approx 4.3 \text{ Mbps} . \quad (4-25)$$

The factor of 2 stems from using a complex filter (having both real and imaginary signal components), and the factor of  $16/14$  corresponds to the increased number of effective bits in the decimated samples. Further reduction to fit within the downlink communication bandwidth could be accomplished with a lossless compression technique such as bit trimming, where allocated code-word length follows the known *a priori* signal energy concentration (high around ZPD and lower in the wings). Assuming a data compression ratio of 2, the final output IR data rate would therefore be approximately 2.2 Mbps.

Sampling these IR signals would require A/Ds running at about 1.5 MHz. (See Section 4.9.2 for an explanation of the number of A/D bits required.) The sampling rate results from an FTS mirror OPD velocity for 2-sided interferograms of:

$$\frac{2 \cdot (0.8 \text{ cm})}{(3.1 - 0.025) \text{ s}} \approx 0.53 \text{ cm/s} , \quad (4-26)$$

which leads to a pixel readout rate of:

$$11000 \text{ cm}^{-1} \cdot 0.53 \text{ cm/s} \cdot 256 \approx 1.48 \text{ MHz} . \quad (4-27)$$

If desired, one approach to reduce the effective A/D speed would be to use two separate A/Ds for each IR waveband. Each A/D would then only have to run at about 740 kHz.

As an estimate of the digital signal processing required to implement the decimation filter, consider the  $-0.2 \text{ cm}$  to  $+0.2 \text{ cm}$  OPD scan range where maximum sustained throughput would occur. The number of undecimated samples per second would equal the frame rate ( $5730 \text{ samples/s}$ ), ensuring that the maximum detector integration time is less than the limit imposed by pixel well-depth constraints. At a readout rate of 1.5 MHz, the processing load for a 180-point complex FIR filter using a decimation factor of 19 corresponds to:

$$\frac{1480000 \cdot 180 \cdot 2}{19} \approx 28 \text{ M multiply \& accumulate ops/s} . \quad (4-28)$$

Again, the factor of 2 stems from using a complex filter.

Many DSP chips offer single-cycle multiply and accumulate instructions, but these often require data to reside in special on-chip memory for fastest performance. This is a constraint that must be considered in designing any processing circuitry because each detector pixel on an FPA will require about 256 input memory locations for a circular buffer to implement the 180-point FIR filter. A  $16 \times 16$  FPA will therefore require approximately 64 k words of fast input memory that are directly accessible by the core processing unit.



The processing strategy outlined above assumes a limited bandwidth allocation for the sounder communication link. If the GOES communication architecture evolves in such a way that more downlink bandwidth becomes available to the sounder, then several interesting operational modes become possible. For instance, the ABS visible channel could be used to generate high-resolution (0.5 km) imagery for a few different color (visible) bands during each 3.1 second sounding. This could perhaps be implemented with a simple filter-wheel configuration. Each additional color band would add about 400 kbps uncompressed data if quantized to 12 bits.

Table 4-18 shows how integration time would vary for slower or smaller-area sounding coverage. ABS instrument requirements dictate 3000 km x 5000 km sounding in 30 minutes, but a relaxed coverage rate could allow 45 minutes. The sensor could also sound over a 3000 km x 3000 km area in 30 or 45 minutes, but readout rates may vary depending on whether the interferometer has to perform multiple sweeps per dwell time to prevent pixel-well saturation. (See Section 4.9.3 for elaboration.) Moreover, the nominal benefit for slower or smaller sounding coverage is an increase in sensor signal-to-noise, all other parameters being held constant. From the generalized radiometric sensitivity equation:

$$\frac{S}{N} = \int_{\lambda_L}^{\lambda_H} \frac{\text{Radiance}(\lambda) \cdot \text{Transmittance}(\lambda) \cdot \text{IFOV} \cdot \text{Collection Area} \cdot D^*(\lambda)}{\text{Focal Length} \cdot \sqrt{\text{Observation Bandwidth}}} d\lambda. \quad (4-29)$$

Because observation bandwidth  $\propto 1/\text{integration time}$ , the instrument's S/N will thus scale approximately as square-root of the integration period. Despite this apparent reduction in ideal S/N, it is important to note that the ABS point design will meet the noise performance requirements even when operated in the fast 3000 km x 5000 km, 30 minute coverage mode.

**TABLE 4-18**

**Alternative ABS Sounding Modes**

<b>Instrument Parameter</b>	<b>3000 x 5000 km in 30 min</b>	<b>3000 x 5000 km in 45 min</b>	<b>3000 x 3000 km in 30 min</b>	<b>3000 x 3000 km in 45 min</b>
IR Detector Array Size	16x16 pixels	16x16 pixels	16x16 pixels	16x16 pixels
Integration Time	3.1 s	4.6 s	5.1 s	7.7 s
Signal-to-Noise (relative)	1.0	1.2	1.3	1.6

## 4.10 ELECTRONICS TRADE-OFF STUDIES



### 4.10.1 Number of A/D Bits

Interferograms should be sampled with sufficiently high resolution so that quantization noise does not dominate the instrument's overall radiometric resolution. In an effectively designed IR system, radiometric noise from detectors (being the least controllable parameter) will generally exceed other noise sources. Operational parameters are then adjusted so that their contributions to system NEdN fall below the detector noise.

Using Lincoln Lab's interferometer model (described in Appendix C), it is possible to predict noise performance for different sampling quantizations. Figure 4-42 reveals the effects on NEdN of varying the number of A/D bits. Note that a 12 bit A/D would yield higher noise than the IR detectors, while a 14 bit A/D's NEdN would fall slightly below detector noise. This suggests using a 14 bit A/D in the ABS point design.

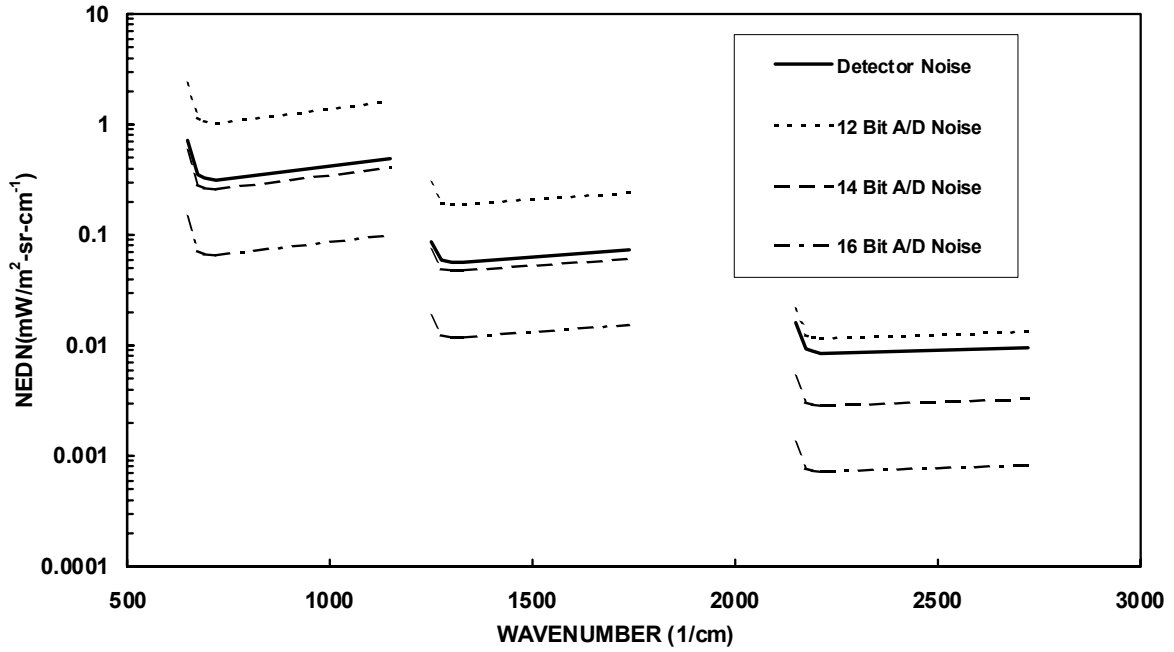


Figure 4-42. Modeled performance for different number of quantization bits.

This conclusion agrees with analytic predictions. Assuming no phase mismatches, it is possible to estimate the number of A/D bits required for some average channel radiance as<sup>29</sup>:

$$b = \log_2 \left( \frac{N_{\text{avg}} \cdot B}{\text{NEdN} \cdot \sqrt{\Delta\nu \cdot s \cdot R}} \right) + 2, \quad (4-30)$$

where  $N_{\text{avg}}$  is the waveband channel's average radiance,  $B$  is the channel's spectral bandwidth,  $\text{NEdN}$  is the noise-equivalent differential radiance,  $\Delta\nu$  is the frequency resolution,  $s$  is the number of interferogram sides used (1-sided or 2-sided), and  $R$  is the sampling rate. For Lincoln Laboratory's point design configuration, these parameters would be about:

$$\begin{aligned} N_{\text{avg}} &= 150 \text{ mW/m}^2/\text{sr}/\text{cm}^{-1} \\ B &= 530 \text{ cm}^{-1} \\ \text{NEdN} &= 0.3 \text{ mW/m}^2/\text{sr}/\text{cm}^{-1} \\ \Delta\nu &= 0.625 \text{ cm}^{-1} \\ s &= 2 \\ R &= 11000 \text{ cm}^{-1} \end{aligned}$$

yielding  $b \approx 13.2$  bits. Accounting for likely phase mismatches and other non-ideal performance effects thus suggests that  $b$  should be 14 bits, in accord with the above spreadsheet model results.

<sup>29</sup> Candell, p. 451

#### 4.10.2 Readout rate vs. Array Size

Using large detector arrays offers some appealing advantages, but they come at a cost. In addition to pushing the design requirements for cooling and optical systems, using a substantially larger array would increase complexity and performance constraints of the electronics system. Figure 4-43 depicts how the integration period grows while the moving mirror velocity diminishes for larger array sizes. Up to a certain size, larger arrays are compensated for by longer dwell times, giving an approximately constant readout rate.

As FPA size increases beyond the nominal 16 x 16 point-design size, however, the frame rate (which scales as  $1/(\text{integration period})$ ) falls below the minimum threshold of approximately 5800 frame/s imposed by PV pixel full-well constraints. It then becomes necessary to shorten the effective dwell time, in effect by speeding up the moving mirror to yield one additional interferogram per integration period. This will therefore increase the array readout rate, assuming the number of output taps and the metrology sampling rate remain fixed. Because the point-design readout rate is already at 1.5 MHz for single output readouts, array sizes larger than 16 x 16 are not recommended.

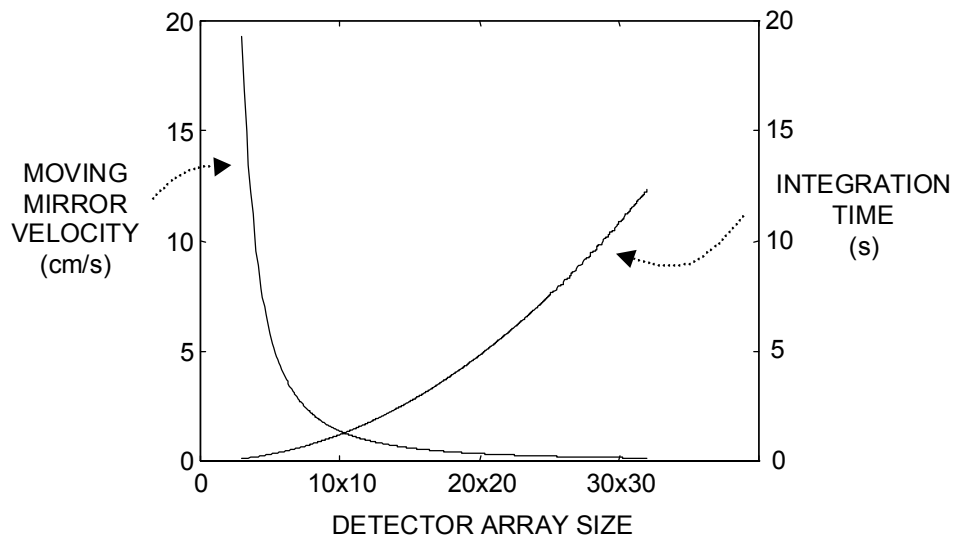


Figure 4-43. Integration period and mirror velocity as functions of FPA size.

#### 4.10.3 Double vs. Single-sided Interferograms

The point design assumes a double-sided interferogram. Using single-sided interferograms could potentially reduce the IR data's output rate by approximately 2, and might also relax some constraints on the moving mirror's porch-swing because it need only travel half the sweep distance. The sampling rate would remain constant, as would the required number of A/D bits.

Nevertheless, it should prove feasible to match most of these benefits by compressing double-sided interferograms. Such compression could encode one side plus any differences from the other side. If the differences were not small (resulting in minimal compression), then using single-sided operation would not be justified either because both sides contain relevant spectral information.

## APPENDIX A

### LIST OF ACRONYMS

A/D	Analog-to-digital converter
ABS	GOES Advanced baseline sounder
ADC	Analog-to-digital converter
AIRS	Atmospheric Infrared Sounder
ASIC	Application-specific integrated circuit
BJT	Bipolar junction transistor
BLIP	Background-limited infrared photo detection
CCD	Charge-coupled (imaging) device
CMOS	Complimentary MOS manufacturing process
CTE	Coefficient of thermal expansion
CTIA	Capacitive transimpedance amplifier
DIP	Dual in-line package
DSP	Digital signal processor
EEPROM	Electrically-erasable PROM
EMI	Electromagnetic interference
EOL	End of life
EOS	NASA Earth observing system
FIR	Finite impulse response
FFT	Fast Fourier transform
FOV	Field of view
FPA	Focal plane array
FTIR	Fourier-transform infrared (spectrometer)
FTS	Fourier-transform (infrared) spectrometer
GEO	Geosynchronous earth orbit
GHIS	GOES High-resolution interferometric sounder
GOES	Geostationary operational environmental satellite
G-R	Generation-recombination
GSD	Ground spot diameter
GSFC	NASA Goddard space flight center
HgCdTe	Mercury-cadmium telluride
IFOV	Instantaneous field of view
InGaAs	Indium-gallium arsenide
ITS	Interferometer thermal sounder
JFET	Junction field-effect transistor
KBr	Potassium bromide
LEO	Low earth orbit
LMIRIS	Lockheed-martin infrared imaging systems division
LW	Longwave sounder band
LWIR	Long-wavelength infrared
MAC	Multiply-accumulate operation
MIT/LL	Lincoln laboratory, massachusetts institute of technology
MOSFET	Metal-oxide-semiconductor field effect transistor
MW	Midwave sounder band
MWIR	Mid-wavelength infrared
NASA	National aeronautics and space administration

NEdN	Noise-equivalent difference in (scene) radiance
NEdT	Noise-equivalent difference in (scene) temperature
NESDIS	National environmental satellite data information service
NOAA	National oceanographic and atmospheric administration
NWS	National weather service
OPD	Optical path-difference
PC	Photoconductive (detector)
PROM	Programmable read-only memory
PTC	Pulse tube cooler
PV	Photovoltaic (detector)
RMS	Root mean-square
ROIC	Read-out integrated circuit
RSS	Root of the sum of the squares
RTIA	Resistive transimpedance amplifier
S/N	Signal-to-noise ratio
SOIC	Small-outline integrated circuit
SRAM	Static random-access memory
SSP	Satellite sub-point (the point on the ground directly below the satellite)
SW	Shortwave sounder band
SWIR	Short-wavelength infrared
TBD	To be determined
TEC	Thermoelectric cooler
TIGR	TOVS Initial guess retrieval
ZnSe	Zinc selenide
ZPD	Zero path-difference

## APPENDIX B

### GRATING AND FTS SPECTROMETERS

In this appendix, the throughput and multiplex advantages of the FTS are examined from the viewpoint of the likely form such instruments would take for the ABS application. It is concluded that these “advantages” themselves are of limited utility in conducting a trade study for ABS, however they lead to comparisons in terms of integration time, instrument noise and cooling requirements which permit a trade to be made.

#### Throughput Advantage Of The FTS, and Implications for Imaging Arrays

***Jacquinot (throughput) advantage.*** The optical throughput attainable through an FTS depends on the beamsplitter area  $A_{bs}$  and spectral resolution  $\lambda/\delta\lambda$ , and can be shown to be

$$(A\Omega)_{FTS} = \frac{\pi A_{bs} \cos \theta}{(\lambda/\delta\lambda)}, \quad (B-1)$$

where  $\theta$  is the angle at which the beamsplitter is set (typically  $30^\circ$ ). In the case of the grating spectrometer, the throughput is limited to

$$(A\Omega)_{grating} = \frac{\beta A_g \sin \phi}{(\lambda/\delta\lambda)}, \quad (B-2)$$

where  $A_g$  is the grating area,  $\phi$  is the angle at which the grating is set, and  $\beta$  is the angle subtended by the slit length. Assuming for the moment that the grating and beamsplitter areas and spectral resolutions are equivalent for the two architectures, the “Jacquinot advantage” of the FTS is given by

$$\frac{(A\Omega)_{FTS}}{(A\Omega)_{grating}} = \frac{\pi \cos \theta}{\beta \sin \phi}. \quad (B-3)$$

Since aberrations and the need for a large focal length make  $\beta$  unlikely to be greater than  $1/30$ , and the angles  $\theta$  and  $\phi$  are likely to be in the vicinity of  $45^\circ$ , the factor given by equation (B-3) is approximately 100 - 150.

***Throughput of a Scene Pixel*** The question then arises: can the ABS instrument make use of this throughput to increase sensitivity? In order to answer this question, the throughput associated with a single scene pixel must be determined. The scene-limited throughput is the product of the solid angle subtended by each ground sample and the aperture area. The solid angle subtended by a ground spot diameter  $D_{spot}$  at a satellite altitude  $h$  is given by

$$\Omega_{spot} = \pi \theta_0^2 = \frac{\pi D_{spot}^2}{4h^2}. \quad (B-4)$$

The detector pixel width is fixed by the choice of available FPA's. The aperture diameter  $D_a$  is then selected to match the Airy spot to the detector pixel width  $W_{pix}$ ,

$$D_a = \frac{2.44 f \lambda}{W_{pix}} = \frac{2.44 h \lambda}{D_{spot}}, \quad (\text{B-5})$$

since the effective focal length is constrained to  $f = h W_{pix} / D_{spot}$ . The throughput available to each pixel is then a function only of wavelength:

$$A_a \Omega_{spot} = \left( \frac{2.44 \pi}{4} \right)^2 \lambda^2 \approx 3.7 \lambda^2, \quad (\text{B-6})$$

and is about  $7 \times 10^{-6}$  at  $14 \mu\text{m}$  (systems are usually designed to match the diffraction spot to the pixel at the longest wavelength). Taking the maximum possible throughput through an FTS from equation (B-1), and using  $R \cong 1000$ , and  $S \cong 10 \text{ cm}^2$ , it is seen that the maximum throughput is  $\sim 10^{-2} \text{ cm}^2\text{-sr}$ , or 3 orders of magnitude larger than the throughput entering a remote-sensing instrument under the above assumptions. In conclusion, because of the modest resolving power ( $\lambda/\delta\lambda \sim 1000$ ) required for ABS the Jacquinot advantage does not appear to be the determinant in the trade study made here because throughput is limited by the scene rather than the instrument.

**Imaging Arrays** Although the scene throughput is orders of magnitude smaller than the limiting throughput of an FTS, the large instrument field of view inferred by the Jacquinot advantage allows the use of imaging arrays in an FTS. When a source pixel is viewed by an FTS at some angle  $\alpha$  to the optical axis, the OPD is decreased by a factor  $\cos \alpha$ . At the focal plane, this phase shift creates a pattern of circular fringes centered on the optical axis similar in appearance to “Newton’s rings”. The derivation of the Jacquinot advantage relies on determining a pixel width which matches the central maximum of this pattern. The modulation at a detector pixel depends on the width of these rings relative to the pixel width<sup>30</sup>, and so for an array of small detectors it is possible to extend the array well into the region beyond the first dark fringe. The implications of this are treated in Section 4.2.

### Multiplex Advantage Of The FTS, and Implications for Detector Noise

**Fellgett (multiplex) advantage.** The FTS simultaneously measures the entire spectrum of the source during each mirror stroke, and so integrates each of  $M$  spectral samples for the full dwell time  $T$ . This usually gives it a second advantage over a grating spectrometer which is scanned to measure the  $M$  samples sequentially with integration time  $T/M$ , giving it a SNR penalty relative to the FTS of  $\sqrt{M}$ . However, by using a focal plane array to simultaneously integrate the signal from each spectral element of the scene pixel this disadvantage may be overcome by a grating instrument with the added benefit of requiring no moving parts. We conclude, then, that the multiplex advantage does not apply for an FTS – grating comparison involving a *single* scene pixel. The FTS does enjoy an advantage in terms of integration time in the ABS trade study, but it arises from the use of imaging arrays to simultaneously image *many* scene pixels, and is a consequence of the throughput advantage as described above. The multiplex advantage of the FTS does manifest itself, however, in the form of much larger photon flux incident on the detector which results in a reduced sensitivity to thermal noise, as summarized in Section 4.2.

---

<sup>30</sup> D. Hearn, “Fourier transform interferometry, Project Memorandum 96PM-GOES-0008, MIT Lincoln Lab., 1995.

## Instrument SNR

We begin this section by following the work of Beer<sup>31</sup>, to derive an expression to compare the relative signal-to-noise ratio which can be obtained from FTS and grating instruments. The reader is directed to the reference for quantitative descriptions of the quantities cited here. The starting point is to formulate the SNR in terms of the signal and noise integrated while viewing the scene, typically by integrating detector signal and noise current onto a capacitor in the readout chip. The SNR in this case is expressed as

$$SNR = \frac{\text{number of signal-generated electrons}}{\sqrt{\text{number of all electrons}}} \quad (\text{B-7})$$

The SNR of FTS and grating instruments can then be shown to be given by

$$SNR^{FTS} = \frac{\delta\nu\eta_m(s_{\text{source emission}} + s_{\text{solar reflection}})\tau_{\text{int}}^{FTS}}{\sqrt{\left[ \left( N_{\text{electronic}} + N_{\text{detector BG}} \right) + \Delta\nu \left( n_{\text{aft optics BG}} + n_{\text{fore optics BG}} + s_{\text{source emission}} + s_{\text{solar reflection}} \right) \right] \tau_{\text{int}}^{FTS}}} \quad (\text{B-8})$$

and

$$SNR^G = \frac{\delta\nu(s_{\text{source emission}} + s_{\text{solar reflection}})(\tau_{\text{int}}^G / M)}{\sqrt{\left[ \left( N_{\text{electronic}} + N_{\text{detector BG}} \right) + \Delta\nu n_{\text{aft optics BG}} + \delta\nu \left( n_{\text{fore optics BG}} + s_{\text{source emission}} + s_{\text{solar reflection}} \right) \right] (\tau_{\text{int}}^G / M)}} \quad (\text{B-9})$$

respectively. The quantities in equations (B-8) and (B-9) are:

$N_{\text{electronic}}$	Detector thermal noise in e <sup>-</sup> /s,
$N_{\text{detector BG}}$	Detector housing background-induced noise in e <sup>-</sup> /s,
$s_{\text{source emission}}$	Signal from source emission in e <sup>-</sup> /(s cm <sup>-1</sup> ),
$s_{\text{solar reflection}}$	Signal from solar reflection in e <sup>-</sup> /(s cm <sup>-1</sup> ),
$n_{\text{aft optics BG}}$	Aft optics background-induced noise in e <sup>-</sup> /(s cm <sup>-1</sup> ),
$n_{\text{fore optics BG}}$	Fore optics background-induced noise in e <sup>-</sup> /(s cm <sup>-1</sup> ),
$\eta_m$	FTS modulation efficiency
$\delta\nu$	Spectral resolution in cm <sup>-1</sup>
$\Delta\nu$	Spectral width of an FTS band in cm <sup>-1</sup>
$\tau_{\text{int}}$	Integration time in s
$M$	Number of spectral samples

The ratio of equations (B-8) and (B-9) then provides a measure of the relative SNR of the two instrument approaches.

<sup>31</sup> R. Beer, "Remote Sensing by Fourier Transform Spectroscopy," *Chemical Analysis* Vol. 120, J. D. Winefordner, Ed., Wiley, 1992.



$$\frac{SNR^{FTS}}{SNR^G} = \frac{\sqrt{\frac{\tau_{int}^{FTS}}{\tau_{int}^G}} \sqrt{M} \sqrt{\left[ \left( N_{electronic} + N_{detector\ BG} \right) + \Delta \nu n_{aft\ optics\ BG} + \delta \nu \left( n_{fore\ optics\ BG} + S_{source\ emission} + S_{solar\ reflection} \right) \right]^G}}{\sqrt{\left[ \left( N_{electronic} + N_{detector\ BG} \right) + \Delta \nu n_{aft\ optics\ BG} + \Delta \nu \left( n_{fore\ optics\ BG} + S_{source\ emission} + S_{solar\ reflection} \right) \right]^{FTS}}} \quad (B-10)$$

We now make the following assumptions as a means of simplifying equation (B-10) while retaining its essential features for the purposes of making the ABS trade:

1.  $M$  is taken to be 1, reflecting our assumption that an array is used by the grating instrument to simultaneously measure each spectral element.
2. The signal from the reflection of solar radiation is ignored, since it is negligible in the spectral region relevant to ABS.
3. The noise arising from the background radiance of the aft optics is ignored, since it does not dominate the ratio (it is multiplied by  $\Delta \nu$  in both the numerator and denominator), and can be minimized by cooling the aft optics.
4. The noise arising from the background radiance of the fore optics is ignored, since an all-reflective telescope and scan mirror are assumed.
5. The detector terms are lumped together, which is reasonable since the background flux of the detector housing and the electronic noise generated in the detector are both primarily a function of temperature.

The resulting ratio is given by

$$\frac{SNR^{FTS}}{SNR^G} \approx \sqrt{\frac{\tau_{int}^{FTS}}{\tau_{int}^G}} \cdot \sqrt{\frac{\eta_m \left( N_{det}^G + \delta \nu \cdot s \right)}{N_{det}^{FTS} + \Delta \nu \cdot s}} \quad (B-11)$$

We complete this section by adding an additional penalty to the FTS which arises because not all of the available power at the instrument aperture can be detected, even in a “perfect” FTS<sup>32</sup>. If some power  $P_0$  enters the aperture at wavenumber  $\nu_0$ , the power falling on the detector as a function of optical path difference  $x$  is given by

$$P(x) = \frac{P_0}{2} \left[ 1 + \cos(2\pi \nu_0 x) \right]. \quad (B-12)$$

Conservation of energy dictates that an equal amount of modulated power must exit the input of the interferometer, given by

$$P'(x) = \frac{P_0}{2} \left[ 1 - \cos(2\pi \nu_0 x) \right]. \quad (B-13)$$

---

<sup>32</sup> D. L. Mooney, et. al., “POES High-resolution sounder study final report,” Project Report NOAA-1, Appendix A. MIT Lincoln Lab., 1993.

In addition, the detection of the interferogram is inherently an AC-coupled process, with a penalty of  $\sqrt{2}$  imposed by the RMS value of the cosine. We now incorporate this  $2\sqrt{2}$  penalty into equation (B-11), while adding a factor of two within the expression for the FTS scene flux to reflect that when the instrument is in the shot-noise-limited regime, reduction of the signal by a factor of two reduces the noise by  $\sqrt{2}$ , making the net penalty a factor of 2 rather than  $2\sqrt{2}$ . The resulting SNR ratio is

$$\frac{SNR^{FTS}}{SNR^G} \approx \frac{1}{2\sqrt{2}} \sqrt{\frac{\tau_{\text{int}}^{FTS}}{\tau_{\text{int}}^G}} \cdot \sqrt{\frac{\eta_m(N_{\text{det}}^G + \delta\nu \cdot s)}{N_{\text{det}}^{FTS} + \frac{\Delta\nu \cdot s}{2}}}. \quad (\text{B-14})$$



## APPENDIX C

### INTERFEROMETER PERFORMANCE MODEL

A Fourier transform interferometer model was used to predict the noise characteristics of the ABS point design. The model has been successfully used on other programs to predict the noise performance of interferometric sounders. Figure C-1 is a flow chart summarizing the instrument parameters incorporated in the model.

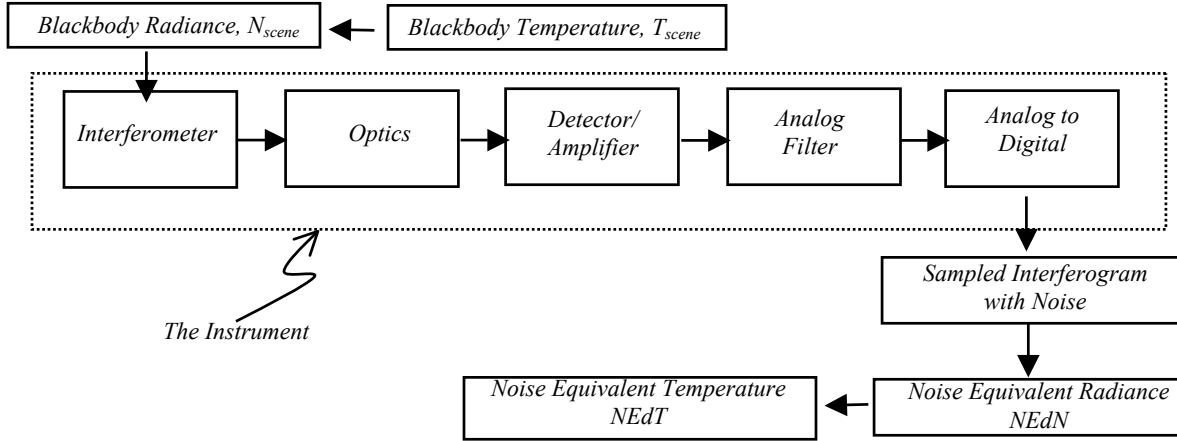


Figure C-1. Flow chart detailing the steps considered in calculating the NEdN of a Fourier transform interferometric sounder.

The earth scene is simulated as an equivalent blackbody radiator. A blackbody temperature is chosen to produce a radiance that is approximately equal to the actual earth radiance in the band of interest. The noise performance is evaluated by considering photon noise, mirror misalignment, mirror velocity fluctuations, amplifier noise, aliasing, and A/D quantization. Each error source is individually modeled to calculate the noise-equivalent difference in scene spectral radiance, NEdN, and signal to noise ratio, S/N. The total NEdN is calculated by combining the various RMS noise terms as the root sum of the squares (RSS). It is defined as the scene spectral-radiance that produces a signal current equal to the total RMS noise current. The NEdN is defined here for each detector in the array at NADIR. The assumption is that each detector is exactly the same. The calculated NEdN can potentially be reduced by the square root of the number of detectors in the array by averaging. It is determined for each wavenumber in the band by transforming the noise current in the interferogram domain to the frequency domain. The noise current spectral density can be represented in wavenumber units to give the effective noise current at each wavenumber in the band. It is calculated using the wavenumber dependent detector responsivity ( $\rho_v$ ) and system transmission ( $\tau_v$ ), along with the instrument field-of-view ( $\Omega$ ) and aperture area (A) by

$$NEdN_v = \frac{4\sigma_v}{A\Omega\tau_v\rho_v} \quad (C-1)$$

where  $\sigma_v$  is the current spectral noise. Additionally, the noise-equivalent difference in scene temperature NEdT can be defined at each wavenumber. It is the equivalent blackbody temperature change, from a reference temperature, required to produce a signal current equal to the RMS noise current at that wavenumber. It is calculated from the derivative with respect to temperature of Planck's spectral irradiance blackbody function  $B(v)$ , for a source at the reference temperature (250 K), multiplied by the NEdN:

$$NEdT_v = NEdN_v \left( \frac{dB(v)}{dT} \right)_{T=250K}^{-1} \quad (C-2)$$

The instrument, satellite, and signal processing parameters, and spectral bands are defined as model inputs. The temperature, transmittance, and emissivity of each component in the signal path are also specified, along with the system  $f$ -number. The total system transmittance for each band is calculated, along with a prediction of the photon flux impinging on the detectors. The model simulates the performance of both photovoltaic (PV) and photoconductive (PC) mercury cadmium telluride (HgCdTe) using a detailed parametric model. The detector detectivity ( $D^*$ ) figure of merit is computed by considering the optical and electrical characteristics of HgCdTe. Post-detection amplifier characteristics are the final user-defined model input. The detector performance sets the lower bound for the instrument NEdN. An interferometric sounder limited by detector noise is ultimately achievable. This appendix outlines the calculation of the detector performance for both PC and PV detectors.

When the detector performance is limited by photon noise, as is true in the MW and SW channels, PV detectors have a  $\sqrt{2}$  advantage in specific detectivity ( $D^*$ ) over PC detectors. The condition for which photon noise dominates is termed background limited infrared photodetection, or BLIP. It is the fundamental limit for photodetection of a scene in the presence of background thermal radiation from the instrument and depends only on the wavelength of the incoming photons ( $\lambda$ ), the photon flux absorbed by the detector ( $\phi_{abs}$ ), and the quantum efficiency of the detector ( $\eta_\lambda$ ). Quantities such as quantum efficiency which depend on wavelength are subscripted to highlight this dependence. For a PC detector, the specific detectivity is given by<sup>33,34</sup>

$$D_{BLIP}^*(\lambda) = \frac{\eta_\lambda}{2E_\lambda \sqrt{\phi_{abs}}} \quad (C-3)$$

The photon energy  $E_\lambda$  is related to the wavelength by  $E_\lambda = hc/\lambda$ . The specific detectivity under BLIP conditions  $D_{BLIP}^*$  for PV detectors is given by

$$D_{BLIP}^*(\lambda) = \frac{\eta_\lambda}{E_\lambda \sqrt{2\phi_{abs}}} \quad (C-4)$$

<sup>33</sup> Kingston, R.H., *Detection of Optical and Infrared Radiation*. Springer-Verlag, New York, 1978.

<sup>34</sup> Dereniak, E.L. and Boreman, G.D., *Infrared Detectors and Systems*, John Wiley & Sons, Inc., New York, 1996.

The PV advantage arises because *only* optically generated minority carriers that diffuse to the photodiode depletion region are detected. Carriers that recombine are not detected, and thus do not contribute to noise. Both processes contribute to signal fluctuations in PC detectors. This is referred to as generation-recombination (G-R) noise.<sup>35</sup> The immunity of PV detectors to optical recombination noise produces a noise spectrum which is  $\sqrt{2}$  times lower than that for PC detectors because the generation noise and recombination noise processes add in quadrature. PV noise current arises from the photo-induced current. Minority carriers that are created in or near the depletion region of the p-n junction are immediately swept across by the strong electric field and detected. Shot noise dominates these detectors.<sup>33</sup>

The above analysis was for BLIP limited detection. At practically achievable detector temperatures in a remote sensing instrument, thermal noise determines the performance of both PC and PV detectors in the LW channel. G-R noise from the random thermal generation of electron-hole pairs and their subsequent recombination affects PC detectors. As the temperature of the device rises, more carriers are excited and thermal G-R noise increases until it becomes the dominant noise mechanism in the detector, a condition which is generally true in the LW band. The noise current density (A/ $\sqrt{\text{Hz}}$ ) due to thermal G-R noise is

$$i_{T(g-r)} = \sqrt{4(eG_{pc})^2 g_{th}} \quad , \quad (\text{C-5})$$

where  $e$  is the electronic charge,  $G_{pc}$  is the photoconductive gain, and  $g_{th}$  is the carrier thermal generation rate. The optical G-R noise current density, which dominates the BLIP limited detector, is

$$i_{O(g-r)} = \sqrt{4(eG_{pc})^2 \phi_{abs} A} \quad , \quad (\text{C-6})$$

where  $A$  is the area of the detector. PC detectors also exhibit Johnson noise, which arises from the random motion of charge carriers in a resistive element. The Johnson noise current density is

$$i_J = \sqrt{\frac{4kT}{R_d}} \quad , \quad (\text{C-7})$$

where  $k$  is Boltzmann's constant, and  $R_d$  is the detector resistance. The total  $D^*$  for PC detectors is<sup>34,35</sup>

$$D_\lambda^* = \frac{\eta_\lambda G_{pc} e}{E_\lambda} \sqrt{\frac{A}{i_J^2 + i_{T(g-r)}^2 + i_{O(g-r)}^2}} \quad . \quad (\text{C-8})$$

Although omitted in the above analysis,  $1/f$  noise can also affect the noise performance of PC detectors.

The noise current in PV detectors arises from the shot noise of charge carriers traversing the depletion region of the p-n junction. There is a constant, temperature-dependent drift of minority carriers across the junction from each side,  $n$  and  $p$ . The two components, the forward and reverse current, are equal in magnitude with zero bias;  $i_f = -i_r = i_o$ .<sup>33</sup> An applied forward bias voltage increases the forward current exponentially. The reverse current saturates to a maximum value,  $i_o$ , when a strong reverse bias is applied. The ideal diode equation describes the current-voltage characteristics of PV detectors

---

<sup>35</sup> Broudy, R.M. and Mazurczyk, V.J., *(HgCd)Te Photoconductive Detectors*, in *Semiconductors and Semimetals*, vol. 18, Willardson, R.K. and Beer, A.C. ED., Academic Press, New York, 1981.

$$i = i_o \left( e^{\frac{\beta e V}{k T}} - 1 \right), \quad (\text{C-9})$$

where  $\beta$  is the ideality factor, and  $i_o$  is the reverse saturation current. The ideality factor ranges between 1 and 2 and is a function of temperature.<sup>34</sup> Figure C-2 shows the current-voltage characteristics of a photodiode (PV detector).

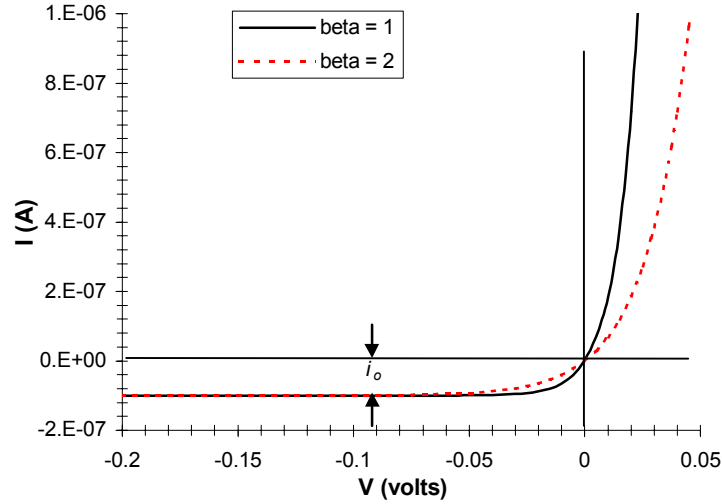


Figure C-2. PV detector current-voltage characteristics

In real devices the reverse saturation current rapidly increases when the reverse bias voltage approaches the breakdown voltage of the device. Often the reverse current in LW PV HgCdTe detectors steadily increases with the bias, before breakdown occurs. This limits the maximum allowable reverse bias one can apply. The non-ideal behavior of the device is primarily due to three effects: quantum mechanical tunneling of carriers across the junction, G-R currents due to defects in the depletion region, and surface leakage. In the absence of an applied bias voltage the net current is zero, however there is shot noise associated with both the forward and reverse currents. The uncorrelated currents add in quadrature (RSS). The thermal noise current density in a PV detector is given by<sup>36</sup>

$$i_T = \sqrt{2e i_o \left( e^{\frac{e V}{k T}} + 1 \right)}. \quad (\text{C-10})$$

The reverse saturation current is

$$i_o = \frac{k T}{e R_o A} \cdot A, \quad (\text{C-11})$$

<sup>36</sup> Reine, M.B., *et.al.*, *Photovoltaic Infrared Detectors*, in *Semiconductors and Semimetals*, vol. 18, Willardson, R.K. and Beer, A.C. ED., Academic Press, New York, 1981.

where  $R_oA$  is the zero bias resistance-area product.  $R_oA$  is constant for a particular photodiode, and is commonly used as a figure of merit for PV devices. Note that with zero bias voltage, the thermal noise term reduces to the Johnson noise,

$$i_T = i_J = \sqrt{\frac{4kT}{R_oA}} \cdot A . \quad (C-12)$$

The photon induced noise current density, which dominates BLIP detectivity, can be calculated from

$$i_{Opt} = \sqrt{2e^2 \phi_{abs} A} . \quad (C-13)$$

The total  $D^*$  for PV detectors is

$$D_\lambda^* = \frac{\eta_\lambda e}{E_\lambda} \sqrt{\frac{A}{i_T^2 + i_{Opt}^2}} . \quad (C-14)$$





## APPENDIX D

### ABS POINT DESIGN OPTICAL PRESCRIPTION

The optical prescriptions for the three infrared channels and the visible channels follow. All linear dimensions are in inches. 'Ade' is a tilt in degrees in the plane of the optics. 'Ben' indicates that the optical axis follows the light path after reflection. 'Yde' is a translation in the plane of the optics perpendicular to the optical axis. If a thickness and decenter or tilt are applied at the same surface, the decenter or tilt is applied first. 'Ady' denotes a translation of the aperture in the plane of the optics perpendicular to the optical axis. 'Dar' indicates that the decenter applies to a single surface. The next surface returns to the previous coordinate definition. Figure D-1 shows a perspective view of the ABS optical system.

#### VISIBLE CHANNEL PRESCRIPTION

Component	Radius	Thickness	Material	Decenter	Aperture (diameter)
		12.811024			
Dummy (optical axis decenter)				yde -5.454545	
Input Telescope M1	-28.20390 k -0.96279	-13.00	REFL		6.4 ady 5.455
Input Telescope M2	-3.24385 k -2.56852	11.50	REFL		0.8 ady 0.428
Input Telescope M3	-16.12670 k -2.28198	-12.00	REFL		2.2 ady -1.000
Dichroic Beamsplitter S1	Infinity	-0.20	Silica	ade -30.0	2.4 ady -1.155
Dichroic Beamsplitter S2	Infinity	0.00			2.4 ady -1.155
Dummy		-1.50		ade 30.0	
Dummy		0.00		yde -1.063242	
Dummy		-6.2281		ade 0.000573	
Element 1 S1	-3.97305	-0.515918	SK6		1.200
Element 1 S2	-2.87718	-0.0600			1.200
Element 2, Doublet S1	-20.34001	-0.251668	LF7		1.200
Element 2, Doublet S2	-4.38494	-0.5500	SK51		1.200
Element 2, Doublet S3	11.63658	-0.6000			1.200
Aperture Stop	Infinity	-3.0000			1.0285
Element 3, Doublet S1	-5.04573	-0.339751	SK51		1.000
Element 3, Doublet S2	1.73349	-0.251668	LF7		1.000
Element 3, Doublet S3	Infinity	-4.724433			1.000
Visible Focal Plane	Infinity				0.214

INFRARED PRESCRIPTION (COMMON COMPONENTS)

Component	Radius	Thickness	Material	Decenter	Aperture (diameter)
		12.811024			
Dummy (optical axis decenter)				yde -5.454545	
Input Telescope M1	-28.20390 k -0.96279	-13.00	REFL		6.4 ady 5.455
Input Telescope M2	-3.24385 k -2.56852	11.50	REFL		0.8 ady 0.428
Input Telescope M3	-16.12670 k -2.28198	-12.00	REFL		2.2 ady -1.000
Dichroic Beamsplitter S1	Infinity	4.50	REFL (ben)	ade -30.0	2.4 ady -1.155
Dummy (optical axis decenter)		0.00		yde -1.00	
Dummy (beamsplitter tilt)				ade 30.0	
Beamsplitter (S1)	Infinity	0.20	ZnSe	yde -0.04233	1.5
Beamsplitter (S2)	Infinity	0.00	REFL (ben)		1.5
Beamsplitter (S1)	Infinity	-0.20	ZnSe		1.5
Dummy				yde -0.04233	
Dummy		-1.30		ade 30.0	
Interferometer Mirror	Infinity	1.30	REFL		1.2
Dummy				ade -30.0	
Beamsplitter (S1)	Infinity	0.20	ZnSe	yde 0.04233	1.5
Beamsplitter (S2)	Infinity	0.05	Air		1.5
Dummy				ade 0.70	
Compensator (S1)	Infinity	0.199484	ZnSe		1.5
Compensator (S2)	Infinity	0.00			1.5
Dummy				yde 0.06984	
Dummy		2.00		ade 29.3	
Aperture Stop		2.91716			1.0844
Dummy (optical axis decenter)				yde -1.400	
Aft Telescope Primary	-6.5 k -1.09221	-2.3	REFL		1.20 ady 1.400
Aft Telescope Secondary	-2.74223 k -4.54585	1.531721	REFL		0.60 ady 0.417

**MIDWAVE CHANNEL PRESCRIPTION (NON-COMMON COMPONENTS)**

Component	Radius	Thickness	Material	Decenter	Aperture (diameter)
LW Dichroic S1	Infinity	-0.8	REFL (ben)	ade 17.0	0.56 ady 0.226
MW Dichroic S1	Infinity	-0.085	ZnSe	ade -17.0	0.66 ady 0.113
MW Dichroic S2	Infinity	0.00			0.66 ady 0.113
Dummy		-0.746467		ade 17.0	
Aft Telescope Image (dar)				ade -1.810744	
Dummy		-0.8780		yde -.012070 ade 7.615280	
Fold Flat	Infinity	1.614158	REFL (ben)	ade -23.8	0.6
Element 1 S1	Infinity	0.166144	ZnSe		0.8
Element 1 S2	-6.29105	0.025561			0.8
Element 2 S1	1.68871	0.127803	Germanium		0.8
Element 2 S2	2.59835	0.678			0.8
Fold Flat	Infinity	-0.430057	REFL (ben)	ade 47.99235	1.0 ady 0.196
Dewar Window S1	Infinity	-0.06	Germanium		0.35
Dewar Window S2	Infinity	-0.3			0.35
Element 3 S1	-0.16931	-0.102242	Germanium		0.15
Element 3 S2	-0.19180	-0.036939			0.15
Midwave Focal Plane					0.0534

**SHORTWAVE CHANNEL PRESCRIPTION (NON-COMMON COMPONENTS)**

Component	Radius	Thickness	Material	Decenter	Aperture (diameter)
LW Dichroic S1	Infinity	-0.8	REFL (ben)	ade 17.0	0.56 ady 0.226
MW Dichroic S1	Infinity	0.75	REFL (ben)	ade -17.0	0.66 ady 0.113
Aft Telescope Focal Plane (dar)				ade 1.531826	
Dummy		1.178125		yde 0.00108 ade -7.61528	
Fold Flat	Infinity	-0.65975	REFL (ben)	ade 48.80765	0.85
Element 1 S1	8.37898	-0.122525	ZnSe		0.7
Element 1 S2	1.89141	-0.01885			0.7
Element 2 S1	-1.27819	-0.09425	Germanium		0.7
Element 2 S2	-1.58887	-0.68732			0.7
Dewar Window S1	Infinity	-0.06	Germanium		0.35
Dewar Window S2	Infinity	-0.347196			0.35
Element 3 S1	-0.13866	-0.0754	Germanium		0.15
Element 3 S2	-0.1488	-0.041192			0.15
Shortwave Focal Plane					0.0534

**LONGWAVE CHANNEL PRESCRIPTION (NON-COMMON COMPONENTS)**

Component	Radius	Thickness	Material	Decenter	Aperture (diameter)
LW Dichroic S1	Infinity	0.085	ZnSe	ade 17.0	0.56 ady 0.226
LW Dichroic S2	Infinity	0.000			0.56 ady 0.226
Dummy		1.519458		ade -17.0	
Dummy				yde -0.00858	
Aft Telescope Focal Plane (dar)				ade 1.531826	
Dummy		0.75		ade -7.615280	
Fold Flat	Infinity	-1.2000	REFL (ben)	ade 48.80765	0.75
Element 1 S1	1.2082	-0.1300	ZnSe		0.75
Element 1 S2	1.39275	-0.0200			0.75
Element 2 S1	-2.62971 k – 5.821651	-0.1000	Germanium		0.75
Element 2 S2	15.41833	-0.65197			0.75
Dewar Window S1	Infinity	-0.06	Germanium		0.35
Dewar Window S2	Infinity	-0.333032			0.35
Element 3 S1	-0.13601	-0.0800	Germanium		0.15
Element 3 S2	-0.16304	-0.024827			0.15
Longwave Focal Plane					0.0534

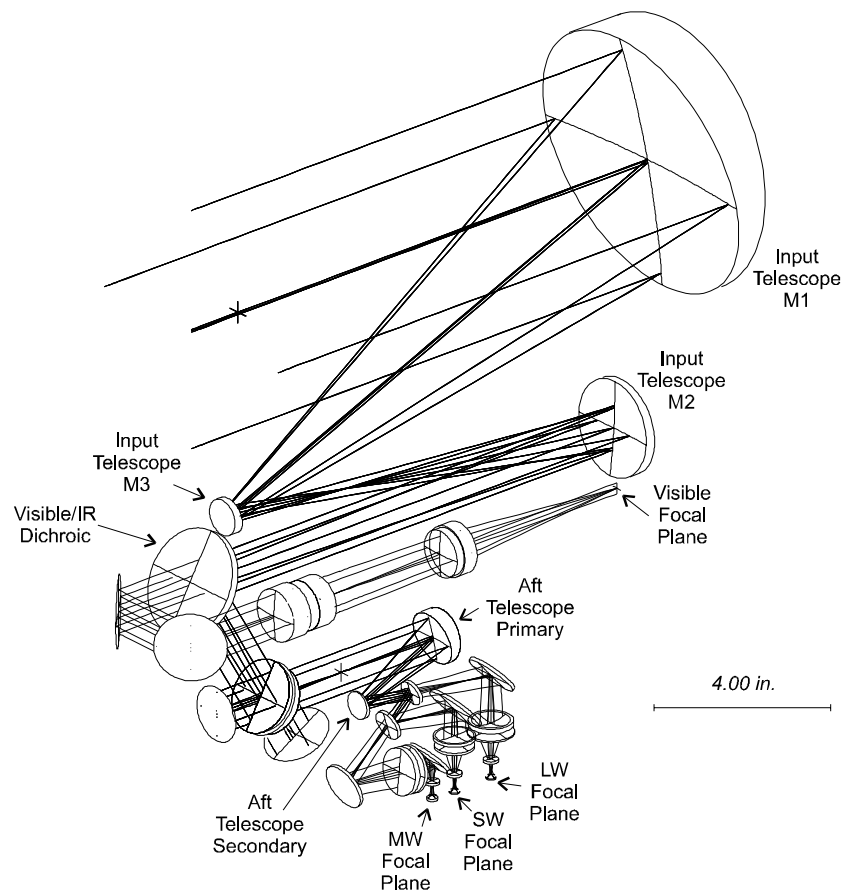


*Figure D-1: Perspective View of the ABS System*